

Air Force Institute of Technology

AFIT Scholar

Theses and Dissertations

Student Graduate Works

3-9-2009

Hyperspectral Imaging of a Turbine Engine Exhaust Plume to Determine Radiance, Temperature, and Concentration Spatial Distributions

Spencer J. Bowen

Follow this and additional works at: <https://scholar.afit.edu/etd>



Part of the [Fluid Dynamics Commons](#), [Other Physics Commons](#), and the [Propulsion and Power Commons](#)

Recommended Citation

Bowen, Spencer J., "Hyperspectral Imaging of a Turbine Engine Exhaust Plume to Determine Radiance, Temperature, and Concentration Spatial Distributions" (2009). *Theses and Dissertations*. 2435.
<https://scholar.afit.edu/etd/2435>

This Thesis is brought to you for free and open access by the Student Graduate Works at AFIT Scholar. It has been accepted for inclusion in Theses and Dissertations by an authorized administrator of AFIT Scholar. For more information, please contact richard.mansfield@afit.edu.



**HYPERSPECTRAL IMAGING OF A TURBINE ENGINE EXHAUST PLUME TO
DETERMINE RADIANCE, TEMPERATURE, AND CONCENTRATION SPATIAL
DISTRIBUTIONS**

THESIS

Spencer J. Bowen, Captain, USAF

AFIT/GAP/ENP/09-M02

**DEPARTMENT OF THE AIR FORCE
AIR UNIVERSITY**

AIR FORCE INSTITUTE OF TECHNOLOGY

Wright-Patterson Air Force Base, Ohio

APPROVED FOR PUBLIC RELEASE; DISTRIBUTION UNLIMITED

The views expressed in this thesis are those of the author and do not reflect the official policy or position of the United States Air Force, Department of Defense, or the United States Government.

AFIT/GAP/ENP/09-M02

HYPERSPECTRAL IMAGING OF A TURBINE ENGINE EXHAUST PLUME TO
DETERMINE RADIANCE, TEMPERATURE, AND CONCENTRATION SPATIAL
DISTRIBUTIONS

THESIS

Presented to the Faculty

Department of Engineering Physics

Graduate School of Engineering and Management

Air Force Institute of Technology

Air University

Air Education and Training Command

In Partial Fulfillment of the Requirements for the

Degree of Master of Science in Applied Physics

Spencer J. Bowen, BS

Captain, USAF

March 2009


APPROVED FOR PUBLIC RELEASE; DISTRIBUTION UNLIMITED

**HYPERSPECTRAL IMAGING OF A TURBINE ENGINE EXHAUST PLUME TO
DETERMINE RADIANCE, TEMPERATURE, AND CONCENTRATION SPATIAL
DISTRIBUTIONS**

Spencer J. Bowen, BS

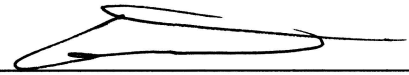
Captain, USAF

Approved:



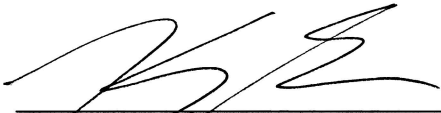
Michael A. Marciniak, PhD (Chairman)

6 Mar 09
Date



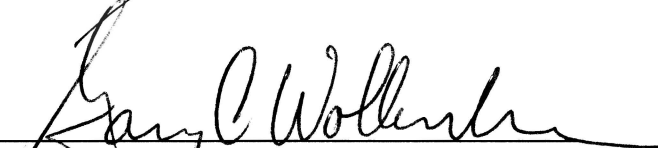
Glen P. Perram, PhD (Member)

6 MAR 09
Date



Kevin C. Gross, PhD (Member)

6-Mar-09
Date



Gary C. Wollenweber (Member)

11-Mar-09
Date

Abstract

The usefulness of imaging Fourier transform spectroscopy (IFTS) when looking at a rapidly varying turbine engine exhaust scene was explored by characterizing the scene change artifacts (SCAs) present in the plume and the effect they have on the calibrated spectra using the Telops, Inc.-manufactured Field-portable Imaging Radiometric Spectrometer Technology, Midwave Extended (FIRST-MWE). It was determined that IFTS technology can be applied to the problem of a rapidly varying turbine engine exhaust plume due to the zero mean, stochastic nature of the SCAs, through the use of temporal averaging. The FIRST-MWE produced radiometrically calibrated hyperspectral datacubes, with calibration uncertainty of 35% in the 1800 – 2500 cm^{-1} (4 – 5.5 μm) spectral region for pixels with signal-to-noise ratio (SNR) greater than 1.5; the large uncertainty was due to the presence of SCAs. Spatial distributions of temperature and chemical species concentration pathlengths for CO_2 , CO, and H_2O were extracted from the radiometrically calibrated hyperspectral datacubes using a simple radiative transfer model for diesel and kerosene fuels, each with fuel flow rates of 300 cm^3/min and 225 cm^3/min . The temperatures were found to be, on average, within 212 K of *in situ* measurements, the difference attributed to the simplicity of the model. Although no *in situ* concentration measurements were made, the concentrations of CO_2 and CO were found to be within expected limits set by the ambient atmospheric parameters and the calculated products of the turbine engine, on the order of 10^{15} and 10^{17} molecules/ cm^3 , respectively.

Acknowledgments

I would like to thank my advisor, Dr. Michael Marciniak, for the support and guidance he provided, and the confidence he had in my ability to accomplish this daunting task.

I would also like to thank my committee members, Drs. Glen Perram and Kevin Gross, and Mr. Gary Wollenweber. Without these three, I would have finished much earlier, but without the level of quality that comes from such a distinguished group. Together they helped push me to a new level of performance. The professional and courteous assistance of Mr. Mike Ranft, Mr. Greg Smith, and Mr. Jeremy Pitz was greatly appreciated.

Without the constant cheer, good humor, and helpful advice of my colleagues in room 210 B, I would probably have lost my mind. Thank you Neil, Mitch, Katie, and Brooke for keeping me sane and full of sugar and caffeine.

My loving wife is a gift from God. I can't count the number of times she was there for me. Listening to my research problems, bringing me lunches and dinners, and having the understanding and compassion to get through the many late nights were just some of the things she did to support me.

Most importantly, I thank God for giving me the gifts and opportunities to accomplish this work. He has carried me, provided me with every necessity, and delivered me.

Spencer J. Bowen

Table of Contents

	Page
Abstract.....	iv
Acknowledgments.....	v
Table of Contents.....	vi
List of Figures.....	viii
List of Tables.....	xvi
I. Introduction.....	1
Motivation.....	1
Problem Statement.....	2
Overview.....	3
II. Background.....	5
Hyperspectral Imaging Technology Overview.....	5
Related Work.....	12
Summary.....	20
III. Experimental Setup.....	21
Physical Layout.....	21
Summary.....	27
IV. Instrument Characterization.....	28
Focal Plane Array Characterization.....	28
Scene Change Artifacts.....	40
Summary.....	51
V. Data Processing.....	52
Error Analysis.....	52
Model Production.....	57
Summary.....	74
VI. Results and Analysis.....	76
Apparent Radiance.....	77
Temperature Spatial Distributions.....	87

	Page
Concentration Spatial Distributions	94
Summary.....	105
VII. Conclusions	107
Future Work.....	109
Final Remarks.....	112
Appendix A. Recovery and Static Temperature	113
Appendix B. Data Averaging Methods.....	114
Appendix C. Atmospheric Constituent Concentrations.....	118
Appendix D. MATLAB Scripts	123
Model Fitting Scripts	123
Two-Temperature Model Scripts	127
Abel Transform Script.....	130
Bibliography	134

List of Figures

Figure	Page
1. Atmospheric transmittance through 11.2 m of standard temperature and pressure atmosphere in the extended midwave band. The absorption features are due to H ₂ O and CO ₂	11
2. Normalized spectral radiance of blackbody functions at temperatures representing the sun, 6000 K, and earth, 300 K. The local minimum occurs at 1736 cm ⁻¹ (5.76 μm), near the edge of the extended midwave band.....	12
3. Diagram of setup for experiments conducted by Schäfer <i>et al.</i> , and Schurmann <i>et al.</i> [13, 14].....	13
4. (a) Exhaust Nozzle Configuration 1: Baseline flow nozzle. (b) Exhaust Nozzle Configuration 17: Core chevron inward angle = 4.5°, core chevron outward angle = 10.25°. (c) Exhaust Nozzle Configuration 7Y: Core chevron inward angle = 9.0°, core chevron outward angle = 15°. (d) Exhaust Nozzle Configuration 7J: Core chevron inward angle = 13.2°, core chevron outward angle = 10.25°. [13].....	15
5. (a) Isotherm plots of data taken from IR camera. (b) Photograph of plume at approximately the same time. Note the similarity of spatial extent between plots and picture. [7]	17
6. The SIGIS HR with components identified. [17]	18
7. (a) Diagram of experimental setup at Building 194, WPAFB, OH (image courtesy of Google Images), (b) a view of the setup from the perspective of the Telops FIRST-MWE (foreground), (c) the Turbine Technologies SR-30 turbojet engine, thermocouple rake, and cold corner, (d) a view of the setup for the 5 November experimental campaign. The Telops FIRST-MWE is the instrument on the right.	22
8. (a) Variable aperture installed on the FIRST-MWE in order to reduce total radiance observed, (b) a close-up false color image clearly shows the setting of the variable aperture used throughout the experimental campaign, (c) a close-up view of variable aperture installed on the FIRST-MWE, (d) a close-up view of the front optic of the FIRST-MWE, without variable aperture installed.	23

Figure	Page
9. (a) A close-up view of the six thermocouples, looking down the axis of the turbine engine. The offset thermocouples, 42 cm from the exit plane, are out of focus, (b) a perspective view of thermocouple rake and turbine engine, (c) an axial view of the turbine engine and thermocouple rake. The offset thermocouples, 42 cm from the engine exhaust exit plane, are out of focus.	25
10. The integrated spectrum of a blackbody radiator set at 80 °C. The spectrum was averaged over twenty blackbody files of the same temperature to reduce noise. The pixel-to-pixel variation seen is attributed only to differing photon responses at each pixel.	30
11. The FPA non-uniform photon response (a) and dark current offset (b). These gain and offset terms were calculated using blackbodies at two temperatures, and are used to perform a NUC on the FPA.	33
12. An example InSb detector spectral response curve, taken from a detector used in an ABB Bomem MR-154 FTS. The spectral response of the FIRST-MWE detector should resemble this lineshape.	34
13. The spectral response of the InSb detector, averaged over all pixels, as well as the average polynomial fit to each pixel spectral response curve.	36
14. The spectral response (a) and spectral offset (b) of each pixel, as well as the average and standard deviation of all pixels. The outlying lines are due to bad pixels in the FPA. A ninth order polynomial was fit to the spectral response.	36
15. A spectrum collected by the FIRST-MWE. One hundred fifty datacubes were averaged, followed by the application of the NUC and spectral gain and offset. These data are at pixel (170, 32) of the diesel fuel type, 225 cm ³ /min fuel flow rate.	37
16. The NESR of the Telops FIRST-MWE.	38
17. The photon response per pixel plotted against the spectral response per pixel in a peak emission region shows strong correlation between the two in the case when the offset is ignored (a), and shows very little correlation between the two in the case when the offset is included (b).	39

Figure	Page
18. Visualization of the impact SCAs have on the variation in a spectrum, compared with the NESR of the instrument. The variation due to SCAs is much greater than the NESR. This data taken from diesel fuel, 225 cm ³ /min flow rate, pixel (170, 32).	41
19. The FPA at a single interferogram OPD mirror position (a), incremented by one OPD mirror position (b), and the difference between the two (c). Scene change between the OPD mirror positions is detectable.	42
20. An interferogram taken from file with a flare-up at OPD mirror position 5882. The interferogram was taken from pixel (170, 32), diesel fuel with a flow rate of 225 cm ³ /min.	43
21. FPA images showing the temporal and spatial propagation of the flare up. The top image (a) is from OPD mirror position 5877, the middle image (b) is from OPD mirror position 5882, and the bottom image (c) is from OPD mirror position 5887. Each image is separated temporally by approximately 1.25 ms.	44
22. Uncalibrated spectrum showing the poor SNR obtained without accounting for SCAs. The spectrum was taken from pixel (170, 32), diesel fuel with a flow rate of 225 cm ³ /min.	45
23. The FPA images show the average over the interferogram dimension of hyperspectral datacube 50616 (a) and hyperspectral datacube 50684 (b), and the difference between the two (c). Both were collected against the turbine engine running diesel fuel at a 225 cm ³ /min fuel flow rate.	46
24. Histograms of an OPD mirror position without flare-ups (a), and an OPD mirror position with two flare-ups (b). Each data point in the histogram is a hyperspectral datacube at the same pixel and OPD mirror position. Both histograms only used datacubes taken while observing the turbine running diesel fuel with a 225 cm ³ /min fuel flow rate.	47

Figure	Page
25. The mean (blue) and median (black) interferogram for pixel (170, 32), taken over 156 hyperspectral datacubes (a). The mean interferogram is biased towards positive values, while the median interferogram is not. The mean (blue) and median (black) spectrum for pixel (170, 32) taken over 156 hyperspectral datacubes, with the Residuals and NESR of the instrument (b). The spectra are very similar. Both (a) and (b) were taken from hyperspectral datacubes observing diesel fuel with a flow rate of 225 cm ³ /min.....	49
26. (a) Unfiltered interferograms of pixel (170, 32), from 156 hyperspectral datacubes, and (b) the same hyperspectral datacubes, filtered to remove all points more than four standard deviations from the mean. These interferograms were taken from hyperspectral datacubes observing diesel fuel with a flow rate of 225 cm ³ /min.....	50
27. Mean spectra from filtered (black) and unfiltered (blue) interferograms. The difference between the two (red) is negligible. These spectra were taken from hyperspectral datacubes observing diesel fuel with a flow rate of 225 cm ³ /min.	50
28. The average, uncalibrated spectrum of pixel (170, 32) from an 80 °C blackbody (blue), with standard deviation (green).	53
29. A calibrated spectrum of pixel (170, 32) from a blackbody (green) with the theoretical planckian (blue). The residuals (blue, subplot) of the calibrated spectrum against the planckian are on the same order as the uncertainty in the calibration (green, subplot), and the NESR of the FIRST-MWE (red, subplot).	57
30. Peak-normalized calibrated spectra at 1 cm ⁻¹ resolution from the 5 November 2008 experimental campaign are shown overlaid (a), and correspond to the white pixels within the plume image (b). These demonstrate the phenomenon of higher temperatures moving the energy into higher ro-vibrational transitions according to the Maxwell-Boltzmann distribution, and the increased ability to discern the temperature differences at higher resolution.	60
31. Peak-normalized calibrated spectra at 8 cm ⁻¹ resolution from the 1 July 2008 experimental campaign are shown overlaid (a), and correspond to the black outlined pixels within the plume image (b) [27]. These demonstrate the phenomenon of higher temperatures moving the energy into higher ro-vibrational transitions according to the Maxwell-Boltzmann distribution, and the increased ability to discern the temperature differences at higher resolution.	61

Figure	Page
32. Diagram illustrating the radiative transfer model of the experimental setup.	63
33. The seventeen pixels selected to represent the scene for determination of the atmospheric constituents. The color scale is in units of $W/cm^2-Sr-cm^{-1}$	69
34. Flow chart illustrating the model fitting algorithm. Two loops, containing three least squares search routines, were used to determine the atmospheric constituents at representative pixels.	69
35. The model (red) fit to the spectrum (black) with residuals (blue) and NESR (green) at pixel (170, 31) (a), pixel (100, 31) (b), pixel (60, 31) (c), and pixel (24, 31) (d). All are with diesel fuel at a $225\text{ cm}^3/\text{min}$ flow rate.	72
36. The model (red) fit to the CO emission spectrum (black) with relative residuals (blue) at pixel (170, 31) (a), pixel (100, 31) (b), pixel (60, 31) (c), and pixel (24, 31) (d). All are with diesel fuel at a $225\text{ cm}^3/\text{min}$ flow rate.	73
37. The model (red) fit to the CO_2 emission spectrum (black) with relative residuals (blue) at pixel (170, 31) (a), pixel (100, 31) (b), pixel (60, 31) (c), and pixel (24, 31) (d). All are with diesel fuel at a $225\text{ cm}^3/\text{min}$ flow rate.	74
38. Visible image of the test setup as taken by the FIRST-MWE bore-sighted camera. The engine is on the right edge of the screen with the exhaust pointing to the left, through the thermocouple rake. The red outline gives the approximate FOV of the MWIR detector on the FIRST-MWE.	76
39. A visible image taken from the bore-sighted camera on the FIRST-MWE, showing the approximate FOV of the MWIR detector.	77
40. Total apparent radiance distribution, diesel Fuel at a $300\text{ cm}^3/\text{min}$ flow rate (a) and $225\text{ cm}^3/\text{min}$ flow rate (b), kerosene Fuel at a $300\text{ cm}^3/\text{min}$ flow rate (c) and $225\text{ cm}^3/\text{min}$ flow rate (d). The color scale is in units of $W/cm^2-Sr-cm^{-1}$	78
41. A calibrated spectrum (blue) with the calibration uncertainty (green) and the FIRST-MWE NESR (red) shown for pixel (170, 31) (a), and pixel (100, 31) (b), with kerosene fuel at a $225\text{ cm}^3/\text{min}$ flow rate.	80

Figure	Page
42. A calibrated spectrum (blue) with the calibration uncertainty (green) and the FIRST-MWE NESR (red) shown for pixel (60, 31) (a), and pixel (24, 31) (b), with kerosene fuel at a 225 cm ³ /min flow rate.	81
43. A total apparent radiance distribution showing the pixels selected for showcasing the uncertainty associated with the calibrated data. The white pixels in the image represent the spectra shown in Figures 41 and 42.	82
44. Spatial distribution of the percent standard deviation in the spectra of each pixel, averaged over the spectral dimension for a blackbody (a) and for the turbine engine exhaust scene (b). As expected, the pixels within the plume exhibit more variation than those outside the plume, and much more than the blackbody. The color scales are in percent.	83
45. The spatial distribution of SNR. This was computed by taking the average NESR compared with the average signal at each pixel.	85
46. Calibrated spectrum of pixel (170, 32), from the kerosene fuel at a 225 cm ³ /min flow rate, and the NESR of the FIRST-MWE.	86
47. Calibrated spectrum of pixel (15, 30), from the kerosene fuel at a 225 cm ³ /min flow rate and the NESR of the FIRST-MWE.	87
48. Spatial distribution of temperatures determined by the model for diesel fuel at a 300 cm ³ /min flow rate (a), diesel fuel at a 225 cm ³ /min flow rate (b), kerosene fuel at a 300 cm ³ /min flow rate (c), and kerosene fuel at a 225 cm ³ /min flow rate (d). The color scale is in Kelvin.	89
49. A distribution showing the ratio of the temperature distributions of the two fuel flow rates, 300 cm ³ /min to 225 cm ³ /min, for diesel (a) and kerosene (b). The ratio highlights the fact that the 300 cm ³ /min flow rate produces higher temperatures for both fuel types.	90
50. A distribution showing the ratio of the temperature distributions of the two fuel types, diesel to kerosene, for 300 cm ³ /min (a), and 225 cm ³ /min (b). The ratio highlights the similarities between the temperature distributions produced by the two fuel types.	90
51. Pixels used to identify the model determined temperature equivalent to the temperatures measured by the thermocouples. The pixels in each region were averaged together to provide a single temperature for comparison.	91

Figure	Page
52. Thermocouple temperature measurements taken over the course of approximately 20 minutes of turbine engine run time at 21 cm (a) and 42 cm (b) from the exhaust plume exit plane, converted to static temperature in K. The on-axis thermocouples exhibited the highest temperatures, as expected. The sharp increase in temperature is due to the initial startup of the turbine engine.	93
53. Spatial distribution of CO ₂ concentration pathlength for diesel fuel at a 300 cm ³ /min flow rate (a), diesel fuel at a 225 cm ³ /min flow rate (b), kerosene fuel at a 300 cm ³ /min flow rate (c), and kerosene fuel at a 225 cm ³ /min flow rate (d). The color scale is in molecules/cm ²	95
54. Spatial distribution of H ₂ O concentration pathlength for diesel fuel at a 300 cm ³ /min flow rate (a), diesel fuel at a 225 cm ³ /min flow rate (b), kerosene fuel at a 300 cm ³ /min flow rate (c), kerosene fuel at a 225 cm ³ /min flow rate (d). The color scale is in molecules/cm ²	96
55. Spatial distribution of CO concentration pathlength for diesel fuel at a 300 cm ³ /min flow rate (a), diesel fuel at a 225 cm ³ /min flow rate (b), kerosene fuel at a 300 cm ³ /min flow rate (c), kerosene fuel at a 225 cm ³ /min flow rate (d). The color scale is in molecules/cm ²	97
56. A distribution showing the ratio of the concentration pathlength distributions of the two fuel flow rates, 300 cm ³ /min to 225 cm ³ /min, for diesel (a) and kerosene (b). The ratio distribution highlights the fact that the flow rates produce similar concentration pathlength distributions for both fuel types.	98
57. A distribution showing the ratio of the concentration pathlength distributions of the two fuel types, diesel to kerosene, for 300 cm ³ /min (a), and 225 cm ³ /min (b). The ratio distribution highlights the differences between the CO ₂ concentration pathlength distributions produced by the two fuel types.	99
58. The model (red) fit to the spectrum (black) of pixel (165, 28), where the SNR was 9.3 and the pathlength approximately 2.4 cm. The residuals (blue) and NESR (green) are also shown. The full spectral region (a), as well as the regions of H ₂ O (b), CO (c), and CO ₂ (d) are shown. The concentrations of CO ₂ , H ₂ O, and CO were determined by the model to be 1.4x10 ¹⁷ , 9.1x10 ¹⁶ , and 1.8x10 ¹⁶ molecules/cm ³ , respectively.	102

59. The model (red) fit to the spectrum (black) of pixel (167, 35), where the SNR was 10.9 and the pathlength approximately 2.4 cm. The residuals (blue) and NESR (green) are also shown. The full spectral region (a), as well as the regions of H₂O (b), CO (c), and CO₂ (d) are shown. The concentrations of CO₂, H₂O, and CO were determined by the model to be 1.3×10^{17} , 8.8×10^{16} , and 1.6×10^{16} molecules/cm³, respectively.103
60. The model (red) fit to the spectrum (black) of pixel (170, 32), where the SNR was 17.3 and the pathlength approximately 2.4 cm. The residuals (blue) and NESR (green) are also shown. The full spectral region (a), as well as the regions of H₂O (b), CO (c), and CO₂ (d) are shown. The concentrations of CO₂, H₂O, and CO were determined by the model to be 1.6×10^{17} , 1.1×10^{17} , and 2.3×10^{16} molecules/cm³, respectively.104
61. A spatial domain average (blue) and a spectral domain average (green) of twenty hyperspectral datacubes observing a blackbody at 80 °C, over the spectral range 1800 – 5000 cm⁻¹ (2 – 5.56 μm) (a), and 2500 – 5000 cm⁻¹ (2 – 4 μm) (b). The spatial average performed only a single Mertz phase correction, while the spectral average performed twenty. The non-zero energy in the spectrum of the spectral domain average at wavenumbers greater than 3000 cm⁻¹ (3.33 μm) is unphysical.115
62. A spectral domain average with only one phase correction (blue) and a spectral domain average with multiple phase corrections (green), observing a blackbody at 80 °C, over the spectral range 1800 – 5000 cm⁻¹ (2 – 5.56 μm) (a), and 2500 – 5000 cm⁻¹ (2 – 4 μm) (b). The singly phase corrected spectrum approaches zero signal at high wavenumbers, and the multiply phase corrected spectrum does not.116

List of Tables

Table	Page
1. Weather conditions reported for the experimental campaign conducted on 5 November 2008, as provided by the Air Force Weather Agency. The format is standard METAR, converted to SI units and test-site elevation.	26
2. Model determined average temperatures associated with two regions of the scene corresponding to the two thermocouple locations, thermocouple static temperatures for the axial position, and the difference between the two. Region one corresponds to the set of thermocouples approximately 21 cm from the exhaust plume exit plane, and region two corresponds to the set of thermocouples approximately 42 cm from the exhaust plume exit plane.	92

HYPERSPECTRAL IMAGING OF A TURBINE ENGINE EXHAUST PLUME TO DETERMINE RADIANCE, TEMPERATURE, AND CONCENTRATION SPATIAL DISTRIBUTIONS

I. Introduction

Motivation

The Field-portable Imaging Radiometric Spectrometer Technology, Midwave Extended (FIRST-MWE) is an imaging Fourier transform spectrometer (IFTS) recently developed by Telops, Inc, designed for the purpose of hyperspectral imaging. Hyperspectral imaging is capable of providing a wealth of information, even when the target and observer are separated by great distances. Specifically, hyperspectral imaging of turbine engine exhaust plumes has the potential to collect unprecedented levels of information about a target, including spatial distributions of spectral radiance, temperature, and chemical species in the plume. This information, obtained passively and without the need for *in situ* measurements, is valuable to many communities, including academia, industry, and the federal government. In order to harness this information, it is necessary to first determine whether IFTS technology is capable of obtaining high quality data from high frequency turbulent events, such as a turbine engine exhaust plume. It is then necessary to develop techniques that enable the observer to quickly distill this information into a useful subset of data. This is an ability highly prized in the field of target detection that has not yet been achieved. This research is the

first of many efforts designed to bring this future operational capability one step closer to reality.

When remotely sensing turbine engine exhaust plumes with a hyperspectral imager, three dimensions of information are obtained, two spatial and one spectral. These three dimensions of information are referred to collectively as a hyperspectral datacube. In the case of this research, the hyperspectral datacube is comprised of apparent spectral radiance. The hyperspectral datacubes contain vast amounts of information on the target of interest, including distributions of total apparent radiance, temperatures, and chemical species concentration pathlengths. The ability to quickly obtain these distributions without the need for *in situ* measurements is valuable to many fields, including turbine engine maintenance, turbine engine design validation, and target identification.

Problem Statement

The goal of this effort is to demonstrate the capability of IFTS technology to obtain high quality hyperspectral datacubes remotely collected against the exhaust plume of a turbine engine, despite the high frequency variations in the plume. This is accomplished by demonstrating the production of spatially and spectrally resolved hyperspectral datacubes of radiometrically calibrated apparent spectral radiance, and presenting the uncertainty in the spectral radiance measurement. This goal is furthered by developing processes that extract spatial distributions of relative temperature and chemical species concentration from the hyperspectral datacube collected using the Telops FIRST-MWE.

Overview

To this end, a review of current efforts in the field of hyperspectral sensing of turbine engines is presented, as well as the characterization of the processes necessary to produce calibrated data using the Telops FIRST-MWE. These background topics can be found in Chapter II. A description of the experimental setup is provided in Chapter III. Characterization of the FIRST-MWE, to include characteristics of the focal plane array (FPA) and scene change artifacts (SCAs) are presented in Chapter IV. Focal plane array characterization includes a determination of the non-uniformity correction (NUC) and spectral gain and offset. The error analysis and radiative transfer equations necessary to produce calibrated spectral distributions, temperature and concentration distributions, and calibration uncertainties are presented in Chapter V. In Chapter VI, results and analysis are presented for spectral radiance, temperature, and concentration pathlength spatial distributions.

Due to the normal distribution of SCAs, it was determined that IFTS technology is capable of collecting high quality hyperspectral datacubes, despite the large amount of variation present in the turbine engine exhaust plume. Due to the large variation caused by SCAs, the calibrated spectra were found to have 35% uncertainty in the 1800 – 2500 cm^{-1} (4 – 5.5 μm) region for pixels with signal-to-noise ratio (SNR) greater than 1.5. Temperature measurements were compared with results from the spatial distributions, with average agreement within 212 K, and concentration pathlengths for CO_2 and CO were within reasonable limits. The lower limit was the atmospheric concentrations, 2.5×10^{17} , 9.4×10^{15} , and 4.3×10^{15} molecules/ cm^3 for H_2O , CO_2 , and CO, respectively, and the upper limit was calculated from the turbojet chemical species emissions for diesel

fuel to be 7.9×10^{17} , 8.3×10^{17} , and 4.2×10^{16} molecules/cm³ for H₂O, CO₂, and CO, respectively, and for kerosene fuel these were determined to be 8.8×10^{17} , 8.1×10^{17} , and 4.1×10^{16} for H₂O, CO₂, and CO, respectively. Discrepancies between *in situ* temperature measurements and temperatures extracted from the spectra are attributable to the many approximations and assumptions made in order to produce a computationally efficient, tractable model. This document demonstrates the capability of the Telops FIRST-MWE to produce spatially and spectrally resolved hyperspectral datacubes of calibrated apparent spectral radiance collected against the exhaust plume of a turbine engine, and the use of that information in the initial steps of building the capability to extract temperature and chemical species concentration pathlength distributions.

II. Background

Much work has been accomplished in the field of characterizing aircraft plume emission. Most of the efforts to date have been spent looking at the spectral content of the plume and the spatial distribution of temperatures separately, but only recently have the two been merged through the development of hyperspectral imaging devices. In order to effectively communicate a method of determining spatially distributed turbine exhaust gas temperatures and species concentrations using a Telops FIRST-MWE, it is first necessary to conduct an overview of the hyperspectral imaging technology incorporated in the Telops FIRST-MWE, as well as a summary of the unclassified related efforts in the fields of spectroscopic and imaging characterization of turbine engine exhaust plumes. This preparation will provide better understanding of the subsequent sections.

Hyperspectral Imaging Technology Overview

Hyperspectral imaging devices are relatively new data collection tools, the first of which was the airborne visible infrared imaging spectrometer (AVIRIS) developed by the National Air and Space Administration (NASA) and the Jet Propulsion Laboratory (JPL), first operational in 1989 [1]. The application of hyperspectral imaging to characterizing turbine exhaust plumes is even more recent. Due to potential unfamiliarity in this technology area, a description of the characteristics of hyperspectral imaging devices will be covered. Additionally, the use of a hyperspectral imager to determine the spatial distribution of temperatures and chemical species concentrations requires an intimate familiarity with the imaging device to ensure a complete dataset is collected.

With these considerations, it is prudent to provide an overview of hyperspectral imagers in general, with more specific information focused on the temporal interferometer type hyperspectral imagers.

Advantages of Imaging Fourier Transform Spectrometers.

Hyperspectral imaging devices are spatial and spectral data collection tools, where two dimensions of spatial and one dimension of spectral information are recorded. The spectral information recorded by a hyperspectral imager is collected simultaneously in narrow, adjacent spectral bands, generating a spectrum for each pixel of the scene [2]. Hyperspectral sensors include two classes, dispersive spectrometers and interferometers. Additionally, within each class of sensor there are two sub-classes. Within the dispersive spectrometer class, there are spectrometers that use gratings and those that use prisms. Within the interferometer class, there are spatial interferometers, in which one of the spatial dimensions is collected in time, which are typically based on Sagnac's interferometer [3], and temporal interferometers, in which the spectral dimension is collected in time, which are based on Michelson's interferometer [4]. As stated previously, this paper focuses on the characteristics of the temporal interferometer, and will hence forth be referred to generally as an interferometer. A basic understanding of the non-imaging interferometer is assumed, as well as the basics of the gaseous effluent model, both of which have been described in numerous places [4, 5, 6, 7].

The interferometer class of hyperspectral imagers has both advantages and disadvantages compared to dispersive imaging spectrometers. The Fellgett multiplexing advantage and the Jacquinot advantage are two classic advantages; however, additional advantages of interferometers will also be discussed.

The Fellgett advantage refers to the increase in SNR an interferometer-based imaging spectrometer has compared to a dispersive imaging spectrometer due to the number of frames collected in the creation of one interferogram. The following equation shows the SNR varies with the square root of the number of frames collected [5]

$$SNR = N^{\frac{1}{2}}F \frac{(N_s)_{frame}}{\left[(N_b)_{frame} + \frac{J_d A_d \tau_d}{q} + \sigma_{read}^2 + \frac{2^{-2m} N_{FW}^2}{12} + \sigma_{spatial}^2 \right]^{\frac{1}{2}}} \quad (1)$$

where N is the number of frames collected in a single scan of the interferometer, F is a factor due to the method of apodization, and N_s is the number of photoelectrons detected due to the signal. Noise terms are in the denominator: N_b is the number of photoelectrons detected due to the background, which manifests itself as shot noise; the second term is dark current noise; the third is electronics noise; the fourth is quantization noise; and the fifth is spatial noise. Because of the ease at which one can increase the number of frames collected, within the limitations of the Nyquist frequency, it is possible to increase the SNR of an interferogram-based spectrometer over that of a dispersive spectrometer.

A second advantage is the natural spectral calibration an interferometer-type imaging spectrometer employs compared to the complex process of spectrally calibrating a dispersive spectrometer, called the Connes advantage. Typically, a metrology Helium Neon (HeNe) laser is used to trigger frame collections for the interferogram. With the ability to obtain precise knowledge of the wavelength of the laser, and the optical axis location on the FPA, the error in the triggering is very small and only due to the uncertainty in mirror position and optical axis location. Because the HeNe laser travels different distances to reach each pixel on the FPA away from the optical axis, an

additional multiplicative factor is introduced in the spectral axis. It is possible to account for the different pathlengths the HeNe travels to all pixels across the FPA. This precision spacing of the interferogram translates to a precision calibration of the spectral axes when the Fourier transform is computed [5, 8].

One additional advantage an interferometer holds over a dispersive spectrometer is the straightforward control over spectral resolution. The equation for spectral resolution is

$$SR = \frac{1.207}{2 \text{OPD}_{max}} [cm^{-1}] \quad (2)$$

where OPD_{max} is the maximum optical path difference, the greatest distance the interferometer's movable mirror travels from the point of zero path difference (ZPD). The spectral resolution is determined by the distance the movable mirror travels, *i.e.* the maximum OPD, in the collection of the interferogram. The ability to increase mirror travel distance is completely determined by the design of the system. This allows for very high resolution spectra to be collected, with one hundredth of a wavenumber resolution possible [2, 9]. In a dispersive system, the spectral resolution is fixed, and limited by the size of the FPA.

Although interferometers have advantages over dispersive spectrometers, there are also disadvantages which should be covered for completeness. One of the primary disadvantages that plague interferometers but not dispersive spectrometers is the decrease in SNR due to an increase in the number of spectral bands. To gain spectral resolution means to increase the number of spectral bands. As the number of bands increases, the SNR decreases due to the increased background noise contribution from each band. Equation (3), the noise equivalent spectral radiance (NESR) of the system, is a measure

of the noise. The integral of all non-scene wavelengths increases the noise compared to that of a dispersive spectrometer [10].

$$NESR = \frac{L_s(\lambda)}{SNR} = \frac{1}{N^{1/2}F} \sqrt{\frac{\sigma_n^2 + A\Omega \frac{\tau_d}{hc} \int \frac{\tau_b(\lambda)}{2} L_s(\lambda) \lambda \delta\lambda}{A\Omega \frac{\tau_d m \tau_s(\lambda_0)}{hc} \lambda_0 \delta\lambda}} \quad (3)$$

where σ_n^2 is the combined noise of the system, $A\Omega$ is the optical throughput, τ_d is the integration time, h is Planck's constant, c is the speed of light, τ_b is the spectral background factor, which when combined with $L_s(\lambda)$, the signal spectral radiance, creates the background spectral radiance. τ_s is the spectral transmission factor of the signal, and λ_0 is the wavelength of the signal.

All wavelengths of the incident background sum together to increase NESR, while only the wavelength of the signal acts to decrease it. This leads to an overall increase in NESR on the order of the square root of the number of spectral bands [10]. This number of spectral bands can be quite large due to the large spectral range and small spectral resolution obtainable by imaging interferometers. As mentioned previously, a resolution of one hundredth of a wavenumber is achievable. With detectors responsive over thousands of wavenumbers, the decrease in SNR can be a factor of more than 100. This introduces an issue requiring significant consideration when sensing low signal targets; either longer integration times or less spectral resolution may be necessary to achieve a suitable SNR.

Increased resolution causes not only increased noise, but also an increase in the amount of time required to collect an interferogram. Because higher resolutions require the arm of the interferometer to sweep a greater maximum optical path difference, greater resolution requires more time [11]. If the time needed to collect an interferogram is

longer than the time constant of the scene, there will be scene change artifacts in the spectrum. SCAs are spectral manifestations of a changing scene, and they result in increased variation in the spectra. Due to an inability to separate the cause of variations in the spectra, i.e. variations due to SCAs as opposed to variations due to noise, SCAs act to decrease SNR [11]. It is necessary either to ensure collections are fast enough to minimize scene change artifacts, or attempt to account for the decrease in SNR through additional data averaging.

Advantages of the Midwave Infrared Band.

The midwave infrared (MWIR) band is typically defined as $2000 - 3333 \text{ cm}^{-1}$ ($3 - 5 \text{ }\mu\text{m}$), however because the FIRST-MWE is responsive in the region $1818 - 6666 \text{ cm}^{-1}$ ($1.5 - 5.5 \text{ }\mu\text{m}$), this region will be referred to as the extended midwave band. There are many advantages to using the extended midwave band compared to other regions of the electromagnetic spectrum. Three advantages relevant to this work are that the atmospheric transmittance is very high, with the exception of a carbon dioxide (CO_2) absorption band centered at 2325 cm^{-1} ($4.3 \text{ }\mu\text{m}$) and a few water vapor (H_2O) absorption bands centered at 1800 cm^{-1} ($5.5 \text{ }\mu\text{m}$), 3700 cm^{-1} ($2.7 \text{ }\mu\text{m}$), and 5500 cm^{-1} ($1.8 \text{ }\mu\text{m}$), the background radiation from the sun and earth are at a local minimum, and for the specific case of turbine engine exhaust plumes, most of the spectral emission falls within this band.

Although the atmosphere is comprised mostly of nitrogen (N_2), at 78.08%, oxygen (O_2), at 20.95%, argon (Ar), at 0.93%, and CO_2 , at 0.038%, H_2O can also exist in amounts varying from 0 – 4% by volume, with an average around 1% [12]. H_2O and CO_2 account for most of the atmospheric absorption that takes place in the extended

midwave band. The absorption lines of H₂O and CO₂ can be seen in Figure 1, which shows the atmospheric transmittance in the extended midwave band over an 11.2 m path in a standard temperature and pressure atmosphere. This figure was generated using the line-by-line radiative transfer model (LBLRTM) with data from the high-resolution transmission molecular absorption (HITRAN) database.

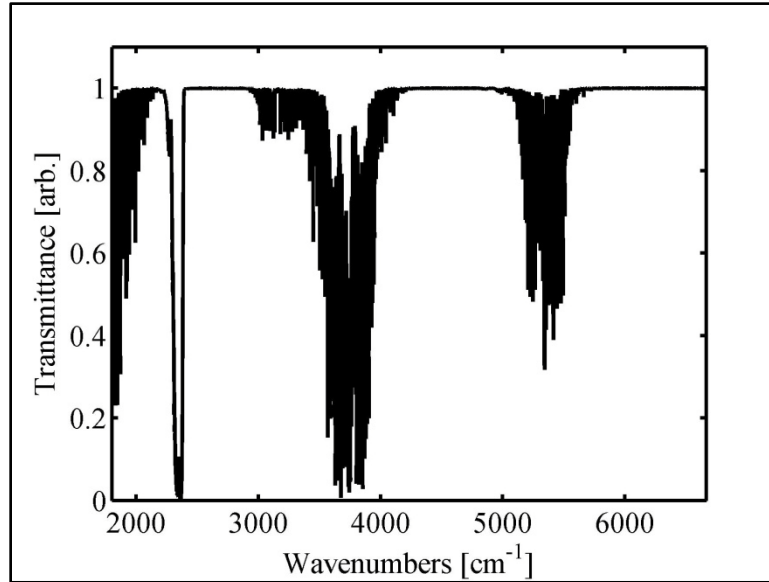


Figure 1. Atmospheric transmittance through 11.2 m of standard temperature and pressure atmosphere in the extended midwave band. The absorption features are due to H₂O and CO₂.

The extended midwave band also has the distinct advantage of being located near a local minimum of spectral radiance from both the sun and earth, which occurs at 1736 cm⁻¹ (5.76 μm). Both the earth and sun emit radiation with emissivity near unity, the earth at approximately 300 K and the sun at approximately 6000 K. Figure 2 shows the local minimum of two peak-normalized blackbody functions representing solar and terrestrial emission. The point where the two curves intersect is just below the extended midwave band. By operating in a band that minimizes the solar and terrestrial spectral radiance, the impact of any background in the scene is reduced, improving the SNR.

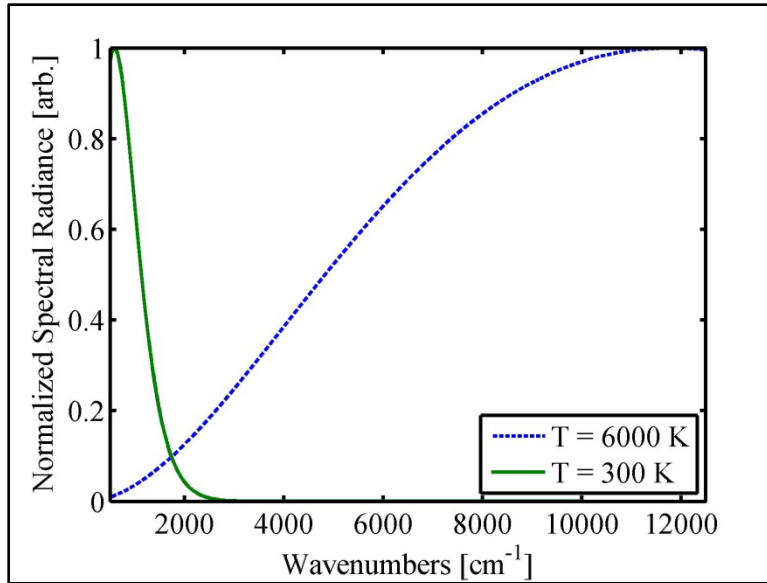


Figure 2. Normalized spectral radiance of blackbody functions at temperatures representing the sun, 6000 K, and earth, 300 K. The local minimum occurs at 1736 cm^{-1} ($5.76\text{ }\mu\text{m}$), near the edge of the extended midwave band.

Related Work

A turbine engine releases many chemical species, and the determination of these species concentrations is useful for multiple reasons previously mentioned. The advantages of using a non-invasive method such as a non-imaging Fourier transform spectrometer (FTS) or IFTS versus using an invasive method are well documented [12, 18]. Some advantages are put forth by Schäfer *et al.* [12] and include:

...lower operational costs, easier handling, and the versatility to provide characterization of engine–turbine emissions early in the development cycle to allow for design alterations; avoidance of costly design and manufacture of extractive sampling rakes; avoidance of the need to demonstrate the representativeness of rake samples; avoidance of chemical changes that could occur within the probe extraction system before it reaches the analytical equipment; elimination of the risk of engine damage during measurement; an improved and expanded database of engine–turbine emissions. [12]

Papers concerning both the spectral content of a plume [6, 12, 14, 15] as well as thermal images of a turbojet exhaust plume [7, 16] are widely available. However, there is only a few published works combining the two via IFTS [17, 18].

Single-pixel FTS of Plumes.

Single-pixel FTS methods of determining chemical species concentrations have been employed in the study of aircraft exhaust with results within 20% to 30% of the standard invasive measurement technique [6, 12, 14]. Schäfer *et al.* [6] and Schurmann *et al.* [14] utilized a Kayser-Threde FTS mounted in a measurement vehicle to view aircraft at various airports throughout Europe. The FTS was set up at multiple locations within the airport to collect spectra of aircraft engine emissions in different stages of operation (*e.g.* idle and taxi), as can be seen in Figure 3.

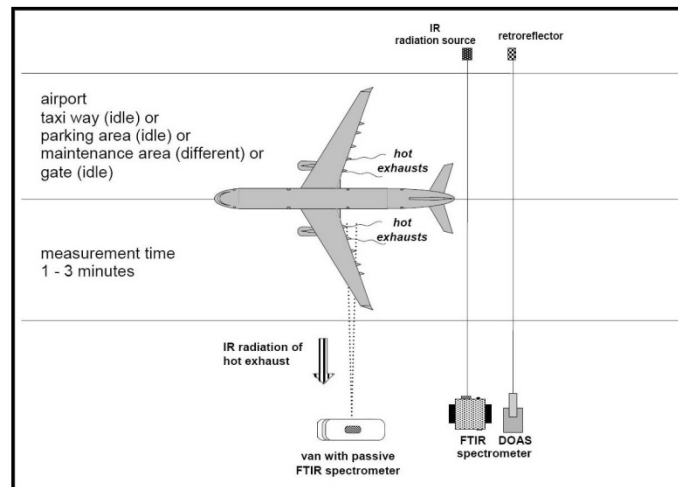


Figure 3. Diagram of setup for experiments conducted by Schäfer *et al.*, and Schurmann *et al.* [13, 14]

The concentrations of carbon dioxide (CO₂), carbon monoxide (CO), nitric oxide (NO) and nitrogen dioxide (NO₂) were determined using a least squares fit of the data to the high-resolution transmission molecular absorption (HITRAN) database using multi-

component air pollution software (MAPS), a proprietary software suite. The spectrum is interpreted by MAPS using line-by-line calculations of the thermal emission and molecular absorptions of the air components. The average emission index (EI) for each chemical species was calculated using [6, 14]

$$EI(X) = EI(CO_2) * \frac{M(X)}{M(CO_2)} * \frac{Q(X)}{Q(CO_2)} \quad (4)$$

Equation (4) assumes complete combustion of the kerosene fuel. The EI is given in grams of the species per kilogram of fuel burned; M denotes the molecular weights and Q the column densities of the species. A theoretical value of the emission index for CO₂ was assumed to be 3159 g/kg, based on the calculation of the stoichiometric combustion of kerosene [6, 12]. These emission indices were then compared with those computed by the International Civil Aviation Organization (ICAO) via intrusive methods measured during engine certification. The non-intrusive measurements were within 30% of the ICAO's intrusive measurements.

IR imagery of plumes.

Much work on IR images of aircraft plumes has been accomplished, especially within the Department of Defense (DoD) [19-24]. However, many of these articles are classified and will not be discussed here. Agboola *et al.* [16] has completed unclassified work containing IR imagery of aircraft engine plumes, and Brustet *et al.* [7] has completed detailed work on the spatial and temporal evolution of temperature within a hot plume.

Agboola *et al.* [16] used an IR camera to collect data for the comparison of different flow nozzle designs for a turbofan engine. The field of view of the camera

covered from the nozzle exit to six fan diameters downstream. The IR imager was used to quantize the relative decrease in thermal emissions each of the different flow nozzle designs achieved compared with a baseline nozzle. Examples of the IR images collected are shown in Figure 4.

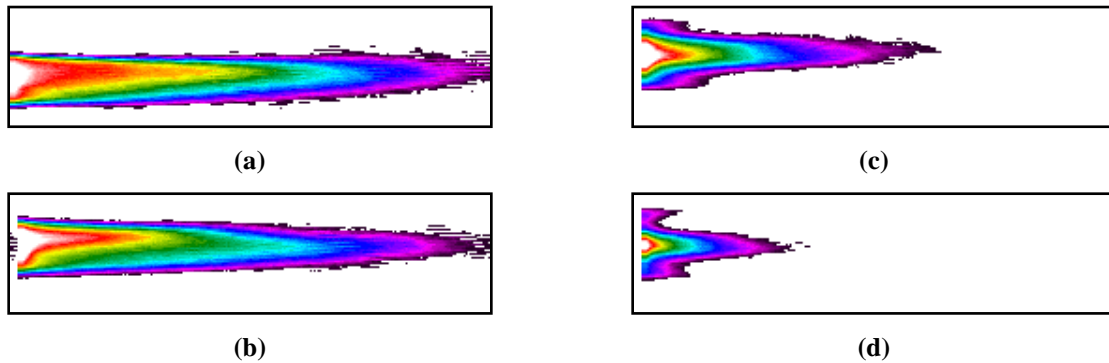


Figure 4. (a) Exhaust Nozzle Configuration 1: Baseline flow nozzle. (b) Exhaust Nozzle Configuration 17: Core chevron inward angle = 4.5° , core chevron outward angle = 10.25° . (c) Exhaust Nozzle Configuration 7Y: Core chevron inward angle = 9.0° , core chevron outward angle = 15° . (d) Exhaust Nozzle Configuration 7J: Core chevron inward angle = 13.2° , core chevron outward angle = 10.25° . [13]

Note the lack of temperature or spatial scale; the IR imager collected only relative distributions of apparent band-integrated flux. The plots shown in Figure 4 are baseline-normalized to show the effect the different flow nozzles had on temperature. However, if the IR imager had a linear response, with *a priori* knowledge of the baseline temperature and gain characteristics of the imager, it would be possible to make estimates of the temperatures for the plume of each model type. Because only relative change in thermal emission was studied, the path length difference within the cylindrical plume was not accounted for, as would be necessary when taking absolute temperature measurements [7].

Brustet *et al.* [7], using an AGA IR movie camera equipped with an indium antimonide (InSb) detector sensitive in the spectral region $2 - 5.8 \mu\text{m}$, collected IR

imagery of an upward rising plume of unburnt hydrocarbons to characterize the spatial and temporal evolution of temperatures within the plume. Although this plume is not due to turbine engine exhaust, many independent measurements were made in an effort to fully characterize this phenomenology. To that end, temperature, pressure, relative humidity and wind speed measurements of the ambient atmosphere were made using multiple radiosonde launchings as well as instrumented aircraft fly-bys. Additionally, source temperature measurements were taken, as well as plume geometry measurements, throughout the test.

To get absolute radiometric data, special attention was paid to the optical depth of the plume. Estimates of the emissivity of the plume were necessary to determine plume radiance and temperature. It was shown via modeling work accomplished by Wyatt *et al.* [25], and Selby *et al.* [26] that for most of the plume height, the approximate optical path length was less than the plume radius. Thus, an approximation of emissivity equal to unity was good for those sections of the plume. This semi-opaque approximation simplified the model to allow the calculation of radiant energy of each pixel to be a function of the estimated plume penetration. Isotherm plots were generated, an example of which can be seen in Figure 5. The temperatures calculated using the IR camera were in agreement with the independent temperature measurements, and the structure was in agreement with the visible photographs showing plume contours. [7]

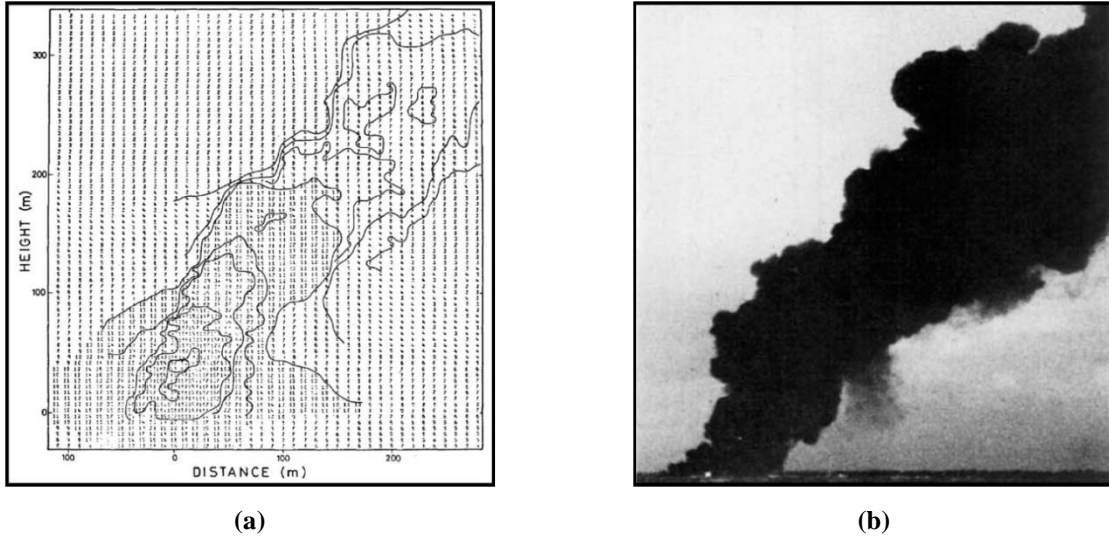


Figure 5. (a) Isotherm plots of data taken from IR camera. (b) Photograph of plume at approximately the same time. Note the similarity of spatial extent between plots and picture. [7]

Imaging FTS of plumes.

Rusch *et al.* [17] and Flores-Jardines *et al.* [18] used a Scanning Infrared Gas Imaging System of High Resolution (SIGIS HR) to collect hyperspectral images of commercial aircraft exhaust plumes. The SIGIS HR, which can be seen in Figure 6, was comprised of a non-imaging FTS, an IR camera, a scanning mirror system equipped with stepper motors, two digital signal processing (DSP) boards, a computer and monitor. The FTS, a Bruker OPAG 22, was equipped with a mercury cadmium telluride (MCT) single-pixel detector responsive in the spectral region $680 - 3500 \text{ cm}^{-1}$ ($2.86 - 14.7 \text{ }\mu\text{m}$). The IR camera had a Jenoptik Variocam Head. The first DSP was dedicated to the FTS; it controlled the mirror movement, data acquisition, preprocessing of the spectral data, and communication with the PC. The second DSP controlled the IR camera and collected images from the camera for viewing on the computer monitor. The instantaneous field of view (IFOV) of the FTS was 15 mrad, 4 mrad when equipped with a telescope. The

minimum step size of the scanning mirror was less than 0.1° , with a total field of regard of 285° by 80° . [17]

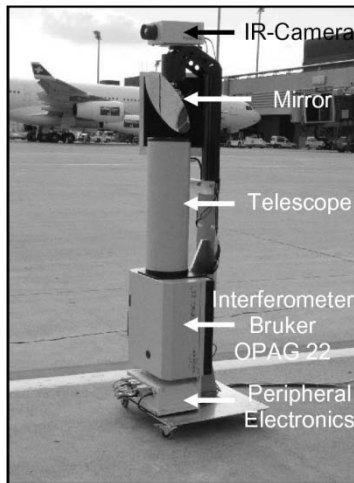


Figure 6. The SIGIS HR with components identified. [17]

Due to the experimental setup within an airport, it was necessary to minimize interference with airport operations and maximize collection time. A fast (17 spectra per second), low resolution (56 cm^{-1}) scan of the area of interest was performed by rastering the field of view using the scanning mirror. A temperature distribution was generated as well as a spectral map, which was used to locate the optimal mirror orientation for obtaining high concentrations of chemical species. To find regions with strong emission, calculations of peak CO_2 intensity versus baseline intensity and band-integrated CO_2 intensity versus band-integrated baseline intensity were computed. Once the scanning mirror was positioned on the pixel with the strongest CO_2 emission, a high resolution scan (0.2 cm^{-1}) was completed for the determination of chemical species concentrations. The system was automated to perform the alignment in as little time as possible, so as to allow for the maximum collection time possible. As discussed previously, the high resolution collection had an SNR lower than a low resolution collection of the same

integration time, due to the increased number of spectral bins, so to achieve a suitable SNR coaddition of multiple datacubes was necessary. [17]

Although this system was capable of hyperspectral operation, a raster scan of the field of view was necessary to acquire a hyperspectral datacube. In some scenarios, this can be an advantage due to the relatively short collection time necessary to achieve the same SNR compared to an IFTS utilizing an array of pixels at the same spectral resolution; the ability to capture a scene with spatial extent on the order of the IFOV and with a small time constant (*i.e.* rapidly varying) is improved. However, this can also be a disadvantage when collecting datacubes of scenes with a spatial extent larger than the IFOV and with a large time constant (*i.e.* slowly varying).

Flores-Jardines *et al.* [18] used the SIGIS HR using the techniques described by Rusch *et al.* [17] to measure high resolution (0.2 cm^{-1}) spectral emissions of the exhaust plume of the CFM56-7B24 engine on a Boeing B737-7Q8. Measurements were also taken against a diesel powered burner. Temperature and chemical species concentration distributions were produced by comparing the collected spectrum to a theoretical spectrum via the least squares fitting algorithm. The theoretical spectra and subsequent fitting were performed using MAPS, the same software suite as was used by Schäfer *et al.* [6, 12] and Schurmann *et al.* [14]. The MAPS software was able to estimate the concentrations of CO_2 , H_2O , CO , and NO in the exhaust plume of both the CFM56-7B24 engine and diesel powered burner. The concentrations were then used to determine emission indices using Equation (4) in the same manner as Schäfer *et al.* and Schurmann *et al.* The average of three measurements produced an emission index for CO of 29 g/kg ,

compared to the ICAO result of 22 g/kg, and an emission index for NO of 4.21 g/kg compared to the ICAO result of 4.4 g/kg. [15]

In a laboratory, Flores-Jardines *et al.* took measurements of a diesel powered burner exhaust plume using the same techniques as for the CFM56-7B24 engine. The laboratory environment allowed time for a full raster scan of the burner plume at high temporal resolution (0.2 cm^{-1}). Using the same post-processing techniques as Rusch *et al.*, a hyperspectral datacube of CO, NO, and temperature was produced from the data.

Summary

A brief description was presented on a few of the advantages and disadvantages of IFTS over other forms of imaging spectroscopy, and a few of the advantages to the MWIR band were discussed. The IFTS method provides flexibility in the selection of many collection parameters, and the MWIR band is ideal for remote detection of turbine engine exhaust plume emissions. Related work was also discussed. The SIGIS HR was optimized to find the region of greatest CO₂ emission and determine the emission indices quickly and efficiently; the FIRST-MWE used in this research was not optimized in this way. Due to the emergent nature and unique properties of the FIRST-MWE, it required much more post-processing to produce relevant data. Although not yet optimized for speed, the FIRST-MWE has already demonstrated the benefit of collecting vast amounts of data when observing turbine engine exhaust emissions through the production of spatial distributions of temperature and chemical species concentration pathlength. The following description of the experimental setup provides necessary background information for the post processing that follows.

III. Experimental Setup

The Telops FIRST-MWE was used to collect hyperspectral imagery of a Turbine Technologies SR-30 turbojet in two experimental campaigns. The first campaign, conducted on 01 July 2008, was reported on previously [27]. The second campaign was conducted on 05 November 2008 at building 194, Wright-Patterson Air Force Base (WPAFB), OH. The second experimental campaign will be focused on due to the extended analysis performed on this data set.

Physical Layout

In the experimental campaign of 05 November, hyperspectral imagery of turbine engine exhaust was collected from a side-plume vantage point with the FIRST-MWE positioned 11.2 meters from the engine, as shown in Figure 7, (a) – (d).

One issue uncovered during the July campaign was the need to use an extremely low integration time, 5 μ sec, when collecting against the turbine engine, which was the lower limit the FPA could achieve. This had the potential to produce corrupted data. The short integration time was necessary in order to avoid saturation at ZPD. In order to increase the integration time without saturation, the FIRST-MWE was fit with a variable diameter aperture at the aperture stop. Figure 8, (a) – (d), show the Telops FIRST-MWE with and without the variable diameter aperture.

This variable diameter aperture was set at 14% of the original aperture stop diameter for the duration of the campaign, which allowed the integration time to be set at a more reasonable 50 μ sec for all collections. Because the data used to calibrate the hyperspectral images were collected with the same aperture stop configuration, use of the

aperture made no impact on the calibration process. If, however, the data were to be calibrated with blackbody data taken without the same diameter aperture, it would be necessary to include a factor relating the two aperture sizes in order to account for the decreased number of photons reaching the FPA. Additionally, if the integration times were varied between the collections, a factor relating the integration times would be necessary as well.

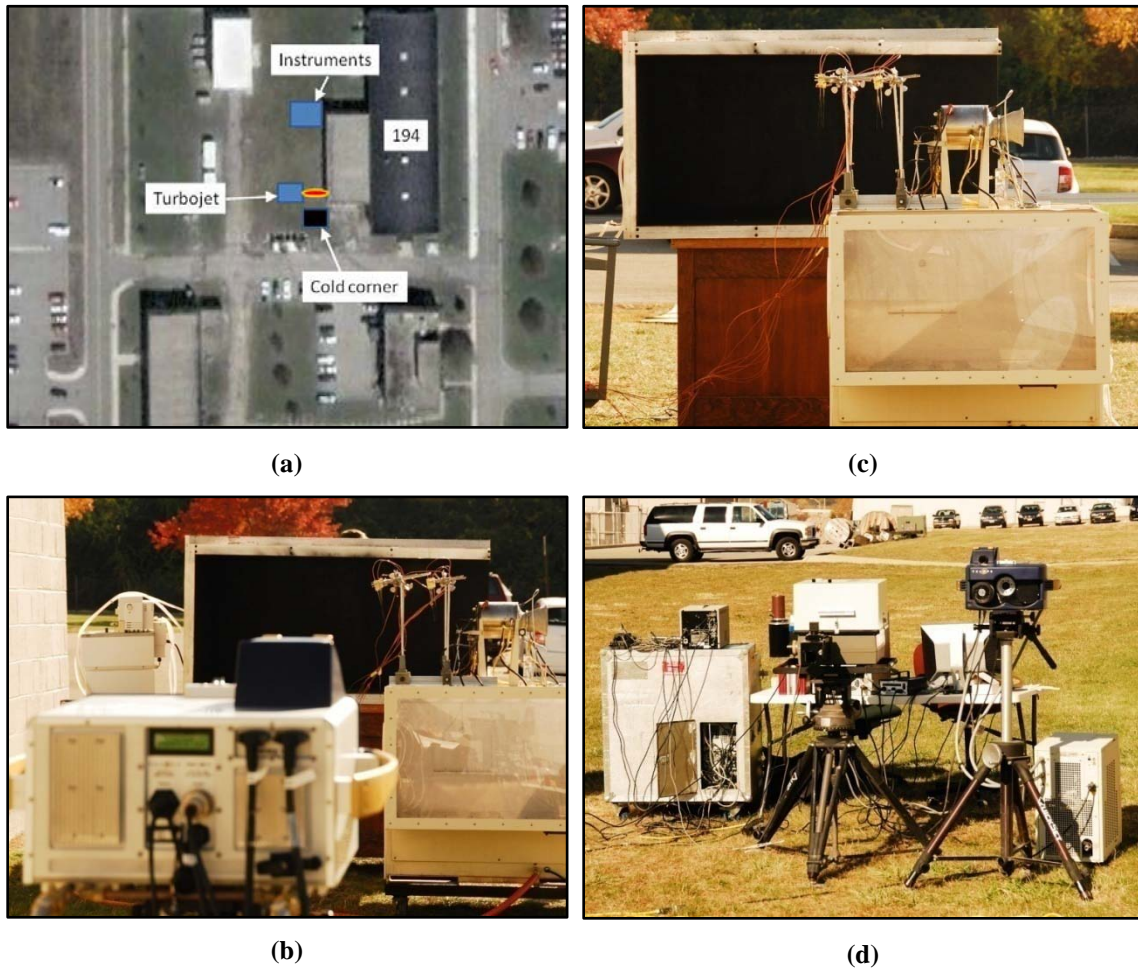


Figure 7. (a) Diagram of experimental setup at Building 194, WPAFB, OH (image courtesy of Google Images), (b) a view of the setup from the perspective of the Telops FIRST-MWE (foreground), (c) the Turbine Technologies SR-30 turbojet engine, thermocouple rake, and cold corner, (d) a view of the setup for the 5 November experimental campaign. The Telops FIRST-MWE is the instrument on the right.

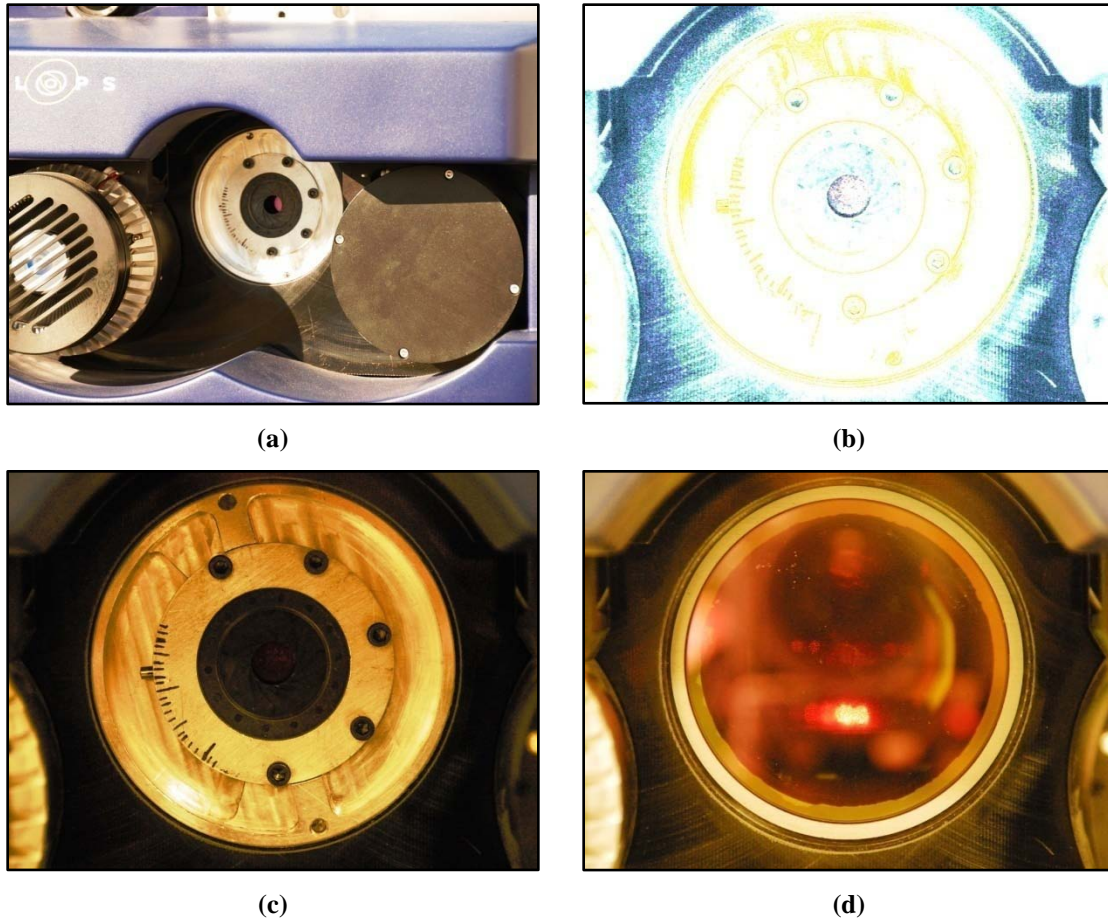


Figure 8. (a) Variable aperture installed on the FIRST-MWE in order to reduce total radiance observed, (b) a close-up false color image clearly shows the setting of the variable aperture used throughout the experimental campaign, (c) a close-up view of variable aperture installed on the FIRST-MWE, (d) a close-up view of the front optic of the FIRST-MWE, without variable aperture installed.

The FPA of the FIRST-MWE was spatially windowed from 320x 256 pixels to 200x64 pixels in order to decrease collection time. With a 0.35 mrad IFOV, the spatial resolution was 3.9x3.9 mm² per pixel, with a total field of regard of 0.77x0.25 m² at the object plane. At a spectral resolution of 1 cm⁻¹ and an integration time of 50 μsec, approximately one hyperspectral datacube was collected every five seconds. Between one hundred fifty and two hundred hyperspectral datacubes were collected for each fuel type and engine setting combination, requiring up to 17 minutes of collection time per

setting. The number of collections was chosen for future co-addition of data to increase the SNR.

In addition to the measurements taken by the FIRST-MWE, six k-type thermocouples were positioned in the plume, and two k-type thermocouples were positioned outside and away from the plume. The thermocouples measured a recovery temperature at a rate of 1.1 Hz. The thermocouples did not capture static temperature because they do not account for the turbulence in the flow; however, static temperature can be obtained from recovery temperature, the details of which are discussed in Appendix A. The six in-plume thermocouples were used for comparison with temperatures obtained via modeling. Three thermocouples were positioned approximately 21 cm from the exit plane, one on the axis of the turbojet, the others offset by approximately 2 cm to the left and right. Three thermocouples were positioned approximately 42 cm from the exit plane. The positioning of the second row was offset from the first, with the right-most thermocouple placed along the axis of the turbine engine, the middle thermocouple approximately 2 cm to the left, and the left-most thermocouple placed approximately 2 cm more to the left. The setup can be seen in Figure 9, (a) – (c).

The SR-30 turbojet was operated with two types of fuel, low sulfur diesel and K-1 kerosene [28, 29]. With each fuel type, the engine was run for an extended period before data collection to allow the system to achieve a stable operating condition. The engine was operated at two fuel flow rate settings for each fuel type, 300 and 225 cm³/min.

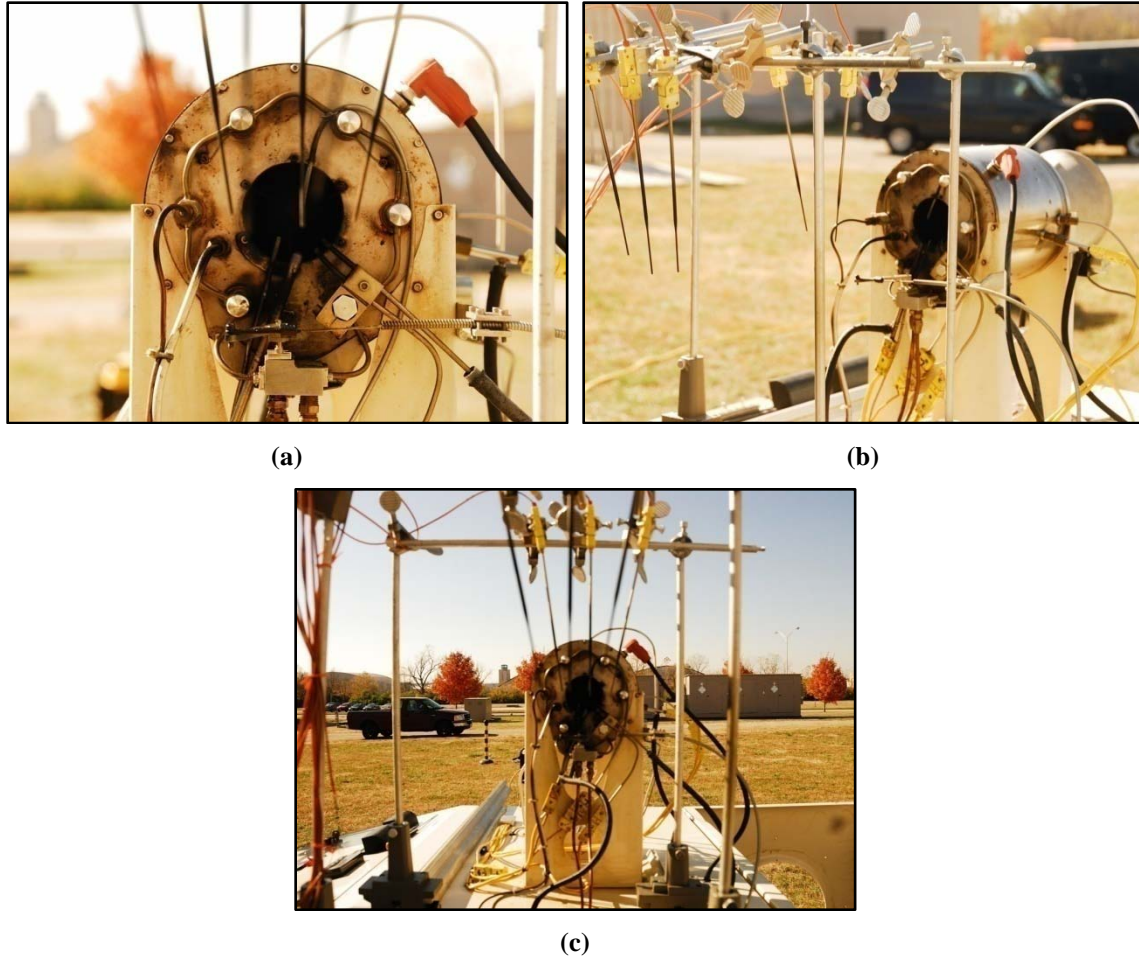


Figure 9. (a) A close-up view of the six thermocouples, looking down the axis of the turbine engine. The offset thermocouples, 42 cm from the exit plane, are out of focus, (b) a perspective view of thermocouple rake and turbine engine, (c) an axial view of the turbine engine and thermocouple rake. The offset thermocouples, 42 cm from the engine exhaust exit plane, are out of focus.

In order to further reduce the amount of background radiation, a custom built $66 \times 66 \times 122 \text{ cm}^3$ blackbody was placed in the background of the scene. Figure 7, (b) and (c), shows the blackbody, which had a shape similar to a corner cube, exposed on only two sides to aid in preventing direct solar illumination. A pump circulated water across the surface, keeping the blackbody near ambient temperature. Due to issues related to chiller performance, it was not possible to achieve temperatures below ambient.

Weather data was collected by the Air Force Weather Agency (AFWA), Detachment 3, on Wright-Patterson AFB Area C. The weather station provided the Meteorological Terminal Aviation Routine Weather Report (METAR), which was converted to International System (SI) units, as shown in Table 1.

Table 1. Weather conditions reported for the experimental campaign conducted on 5 November 2008, as provided by the Air Force Weather Agency. The format is standard METAR, converted to SI units and test-site elevation.

EST Time (24-hour)	Wind Speed (km/hr)	Wind Direction (degrees from North)	Visibility (km)	Temperature (K)	Dew Point (K)	Relative Humidity (%)	Static Pressure (kPa)
0858	00	000	16	280	278	87	99.06
0955	00	000	16	285	280	71	99.06
1055	00	000	16	290	280	52	99.03
1155	00	000	16	293	280	43	98.99
1255	00	000	16	295	280	38	98.86
1316	6	Variable	16	295	280	38	98.83
1325	00	000	16	295	280	38	98.83
1355	6	Variable	11	296	280	36	98.80
1455	9	250	16	296	280	36	98.80
1555	11	130	16	296	278	36	98.70
1655	7	190	16	294	278	40	98.67

The original pressure measurements provided by the METAR were collected at 251 m elevation and reported in units of inches of mercury at sea level. These measurements were converted to kPa at the test location elevation of 256 m using a correction based on the US Standard Atmosphere, 1974 [30, 31].

Although there are many steps necessary in order to calibrate the Telops FIRST-MWE, no calibration process can be performed before data is collected; therefore, before data could be interpreted, it was necessary to utilize data collected against blackbodies during the experimental campaign in order to characterize the instrument. Before, during, and after the data collection against the turbine engine, hyperspectral datacubes

were collected against blackbodies at two temperatures. A total of five sets of blackbody files were collected, with twenty hyperspectral datacubes at two temperatures collected per set. These would later be used in post-processing to characterize the FIRST-MWE and calibrate the data collected against the turbine engine exhaust plume.

Summary

The experimental setup was outlined, showing the major details of the 5 November 2008 experimental campaign at WPAFB. The FIRST-MWE was utilized to collect hyperspectral datacubes at 1-cm^{-1} spectral resolution and 4-mm^2 spatial resolution per pixel against the academic class SR-30 turbojet engine, which was run with two fuel types, diesel and kerosene, and two fuel flow rates per fuel type, $300\text{ cm}^3/\text{min}$ and $225\text{ cm}^3/\text{min}$. A cooled blackbody was used to create a uniform background. Six thermocouples were placed in the plume for later comparison with temperatures extracted from the spectral information. Weather data was recorded and reported by AFWA, Detachment 3, which is used later for determining lower limits on the concentrations within the plume extracted from the spectral information.

No calibration was performed on the FIRST-MWE prior to testing. In order to extract information from the spectrum for comparison with these measurements, it is necessary to perform a calibration of the data collected by the FIRST-MWE during post-processing. Characterization of the FPA, to include non-uniformity of the FPA, the detector spectral response, and the correlation between the two, as well as the impact SCAs have on the data, must be addressed in order to properly calibrate the spectra. These processes enable accurate interpretation of the data.

IV. Instrument Characterization

As stated previously, the FIRST-MWE has many calibration details which must be completed before data can be calibrated and analysis can be accomplished.

Additionally, there have been few publications characterizing the Telops FIRST family of instruments [32], none of which cover the details specific to the FIRST-MWE.

In order to produce calibrated spectra, it is necessary to characterize the focal plane array (FPA) and understand the effect a rapidly varying scene will have on the ability to collect high SNR data. FPA characterization includes identifying the non-uniformity due to variations in the photon response and dark current at the individual pixel level, as well as the spectral response of the InSb detector and the spectral offset due to instrument self-emission. Methods were developed to account for the effect scene change artifacts (SCAs) had on the SNR. All instrument characterization work has been completed to a level sufficient to enable progression of the work. In most cases, this means achieving bounds on the accuracy of a given method, and not optimization.

Focal Plane Array Characterization

FPA characterization is necessary for IFTS systems in order to calibrate the raw data output. The FIRST-MWE does not have on-board software to correct variations across the array, and the spectral response of the detector was also unknown. In order to account for the pixel-to-pixel variations, a NUC was accomplished. To calibrate the raw data, it was necessary to determine the spectral response of the InSb detector.

Non-Uniformity Correction.

The Telops FIRST-MWE was equipped with an Indigo Systems manufactured indium antimonide (InSb) FPA, which exhibited a variation in the pixel-to-pixel output for a similar photonic input. This is known as non-uniformity of the FPA, which is usually caused by imperfections in the readout integrated circuit (ROIC) manufacturing process [33]. This non-uniformity has at least two sources, the pixel-to-pixel variation in photon response and the pixel-to-pixel variation in dark current. Photon response can be described as the number of electrons generated for a number of photons incident on the InSb detector. Dark current is the amount of current received from a pixel when no photons are incident on the InSb detector, a result of the reverse-biased ROIC [34]. Both causes of non-uniformity can be corrected in post-processing; by collecting hyperspectral datacubes of an object with known emissivity, the pixel-to-pixel variation in photon-response and, if necessary, the pixel-to-pixel variation in dark current can be compensated for.

This NUC was accomplished using two methods to better understand the impact variations in photon response versus dark current had on the uniformity of the FPA. The first method could be completed either before or after Fourier transform because both the NUC and the Fourier transform are linear processes. The second method relied on a theoretical blackbody emission spectrum, as given by Planck's equation, and must be completed after the Fourier transform.

The first method used only a gain term to account for the pixel-to-pixel variation in photon response, making the assumption that the dark current offset was minimal and

could be ignored. The second method used an offset term in addition to the gain to account for the dark current present in the FPA.

The first method used to correct the FPA relied on data collected from a single wide-area blackbody set at 80 °C. If the instrument was ideal, the integrated spectrum of all pixels would be the same for each pixel. It was observed, however, that the values at each pixel were not uniform across all pixels, attributable to both a non-uniformity of the pixels and a noise component. With the assumption that the non-uniformity did not vary in time, performing an average over all the files of the same blackbody temperature reduced the noise component of the non-uniformity without affecting the pixel non-uniformity. Twenty hyperspectral datacubes were collected and averaged together to produce a single low-noise hyperspectral datacube. The raw data was averaged over all spectral bins to produce a single value for each pixel. This can be seen in Figure 10.

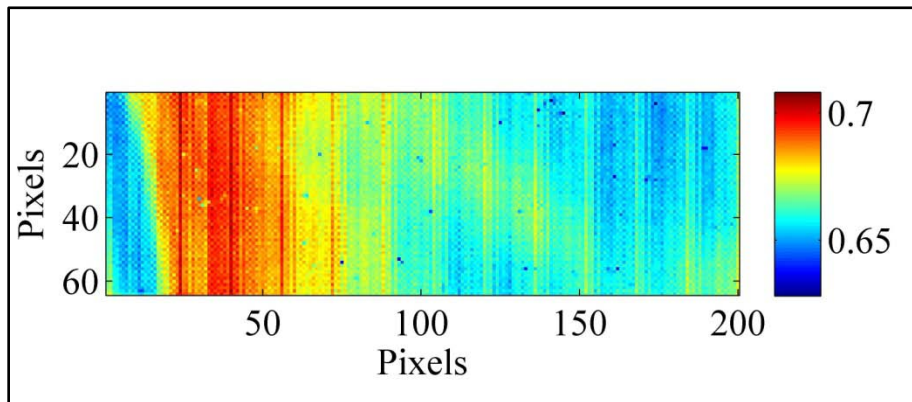


Figure 10. The integrated spectrum of a blackbody radiator set at 80 °C. The spectrum was averaged over twenty blackbody files of the same temperature to reduce noise. The pixel-to-pixel variation seen is attributed only to differing photon responses at each pixel.

The spectrally integrated pixel value was then used to correct the blackbody and turbine engine data by dividing by the median pixel value; this process was completed for all pixels. The equation is given by

$$\overline{C_{obs}}(i, j, T) = g(i, j) \overline{\overline{C_{obs}}}(T) \quad (5)$$

where $\overline{C_{obs}}(i, j, T)$ is the temperature-dependant integrated signal at each pixel, $g(i, j)$, is the photon response of each pixel, and $\overline{\overline{C_{obs}}}(T)$ is the median value of $\overline{C_{obs}}(i, j, T)$, taken over all pixels after integrating the signal.

The photon response was applied to the raw data in the following manner.

$$C_{nuc}(i, j, \bar{\nu}) = \frac{C_{obs}(i, j, \bar{\nu})}{g(i, j)} \quad (6)$$

or equivalently,

$$C_{nuc}(i, j, x) = \frac{C_{obs}(i, j, x)}{g(i, j)} \quad (7)$$

where $C_{nuc}(i, j, \bar{\nu})$ is the photon response corrected spectrum at each pixel location, and $C_{nuc}(i, j, x)$ is the photon response corrected interferogram at each pixel location.

When the single blackbody NUC was accomplished in the spatial domain, it insufficiently accounted for the non-uniformity of the FPA because it did not sufficiently correct different temperature blackbody inputs. This prompted the incorporation of a two-point NUC to attempt to account for the non-trivial amount of DC bias.

The two on-board blackbodies, set at 20 °C and 80 °C, respectively, were used. Twenty hyperspectral datacubes were collected at each temperature and averaged together to produce one low-noise hyperspectral datacube per temperature. The photon response and dark current offset were found using the following set of equations.

$$\overline{C_{obs,1}}(i, j, T_1) = g(i, j) \overline{L_{BB}}(T_1) + o(i, j) \quad (8)$$

$$\overline{C_{obs,2}}(i, j, T_2) = g(i, j) \overline{L_{BB}}(T_2) + o(i, j) \quad (9)$$

where $\overline{C_{obs,1}}(i, j, T_1)$ and $\overline{C_{obs,2}}(i, j, T_2)$ are the temperature-dependant signals observed by the FIRST, averaged over all spectral bins at each pixel and temperature, with i and j

pixel indices and temperatures $T_1 = 80 \text{ }^\circ\text{C}$ and $T_2 = 20 \text{ }^\circ\text{C}$; the photon response of each pixel is represented by $g(i, j)$; $\overline{L_{BB}}(T)$ is Planck's blackbody equation, averaged over all spectral bins, which represents the uniform signal; $o(i, j)$ is the dark current of each pixel. These two equations and two unknowns were solved to find the gain and offset at each pixel. Figure 11 shows, respectively, a representative FPA gain and offset produced via this method.

The photon response and dark current offset were applied to the data in the following manner.

$$C_{nuc}(i, j, \bar{\nu}) = \frac{C_{obs}(i, j, \bar{\nu}) - o(i, j)}{g(i, j)} \quad (10)$$

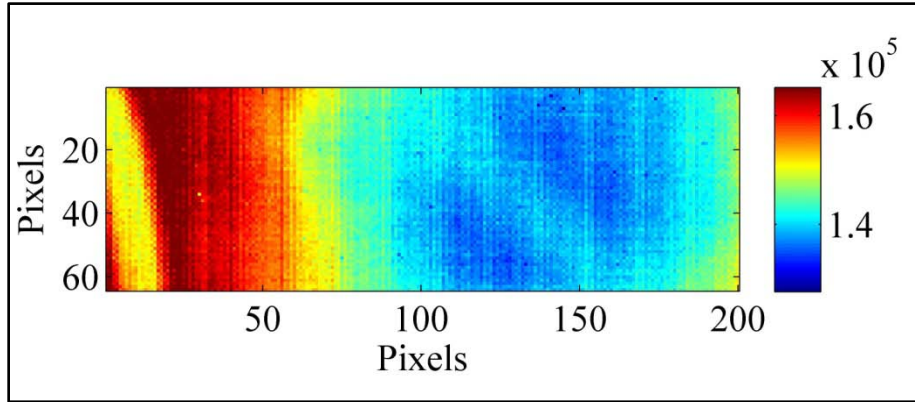
By accounting for both the photon response and dark current offset, the two-point NUC captures much of the pixel-to-pixel variation of the FPA. Although slight variations exist, later sections discuss the impact this has on the calibration process.

Detector Spectral Response.

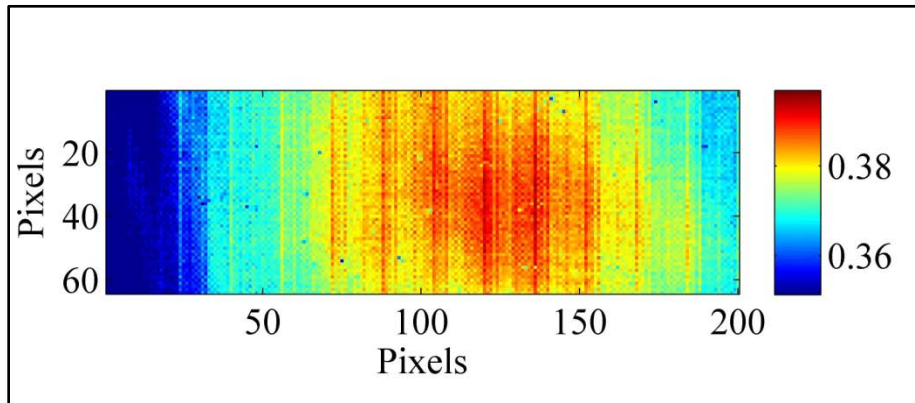
In addition to non-uniformity in the photon response between pixels, the InSb material, which comprises the detector layer of the FPA, has a different response to each wavelength of light to which it is sensitive. This is known as the spectral response of the detector. According to Telops, the FIRST-MWE manufacturer, this InSb material has a non-uniform spectral response to light of $1818 - 6666 \text{ cm}^{-1}$ ($1.5 - 5.5 \text{ } \mu\text{m}$) [35].

In order to convert the spectral data collected by the FIRST-MWE into radiometric quantities and determine spatial distribution maps of temperature and chemical species concentrations, it was necessary to characterize the spectral response of the InSb detector of the FIRST-MWE. The spectral response, in an ideal case, looks like

a sharp increase at the cutoff wavenumber, followed by a linear decrease toward zero with increasing wavenumber [34]. Figure 12 shows an example of what a spectral response curve looks like. This spectral response curve was computed for an InSb detector of an ABB Bomem MR-154 FTS. The spectral response of the FIRST-MWE InSb detector should resemble this lineshape.



(a)



(b)

Figure 11. The FPA non-uniform photon response (a) and dark current offset (b). These gain and offset terms were calculated using blackbodies at two temperatures, and are used to perform a NUC on the FPA.

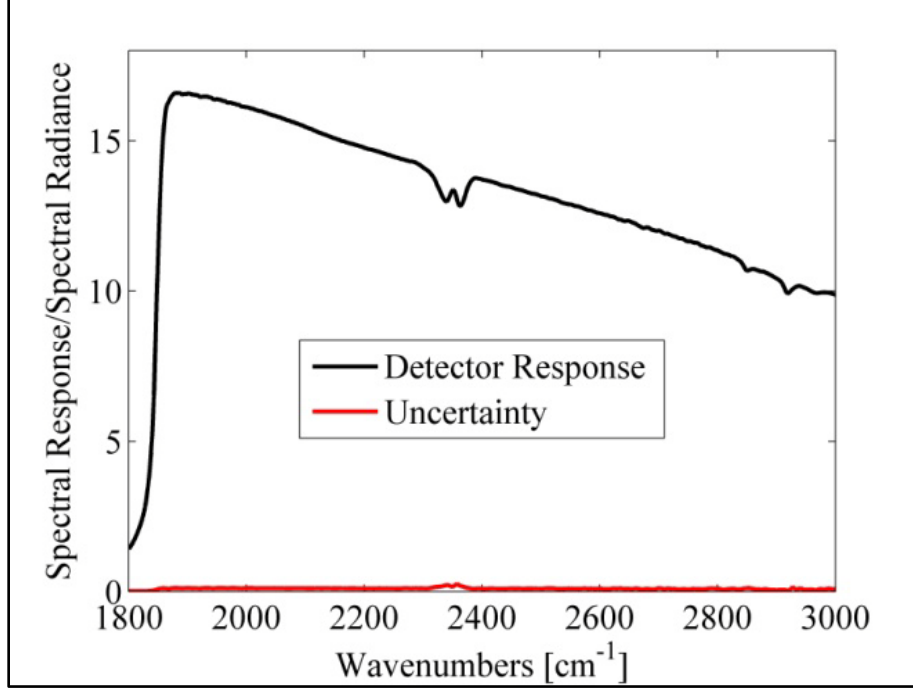


Figure 12. An example InSb detector spectral response curve, taken from a detector used in an ABB Bomem MR-154 FTS. The spectral response of the FIRST-MWE detector should resemble this lineshape.

The spectral response relates the observed signal to a radiometrically calibrated signal and instrument self-emission radiance,

$$C_{nuc}(i, j, \bar{\nu}) = R(\bar{\nu}) [L_{scene}(i, j, \bar{\nu}) + L_{inst}(\bar{\nu})] \quad (11)$$

where $C_{nuc}(i, j, \bar{\nu})$ is the uncalibrated, non-uniformity corrected signal the instrument receives, $R(\bar{\nu})$ is the spectral response of the InSb photodetector, $L_{scene}(i, j, \bar{\nu})$ is the calibrated spectral radiance of the scene and $L_{inst}(\bar{\nu})$ is the calibrated spectral radiance of the instrument self-emission. This can be rewritten as a first order linear equation,

$$C_{nuc}(i, j, \bar{\nu}) = G(\bar{\nu})L_{scene}(i, j, \bar{\nu}) + O(\bar{\nu}) \quad (12)$$

where $G(\bar{\nu}) = R(\bar{\nu})$ is the spectral gain, and $O(\bar{\nu}) = G(\bar{\nu}) L_{inst}(\bar{\nu})$ is the spectral offset, a product of the spectral gain and the instrument self-emission. The assumption was made that the instrument self-emission is without a pixel-to-pixel variation.

By utilizing the known uniform spectrum of the on-board wide-area blackbody, the pixel-to-pixel variation is removed, $L_{scene}(i, j, \bar{\nu}) = L_{BB}(\bar{\nu}, T)$. Using a blackbody at two temperatures, Equation (12) reduces to two first-order linear equations with two unknowns, $G(\bar{\nu})$ and $O(\bar{\nu})$.

$$C_{nuc,1}(\bar{\nu}) = G(\bar{\nu})L_{BB}(\bar{\nu}, T_1) + O(\bar{\nu}) \quad (13)$$

$$C_{nuc,2}(\bar{\nu}) = G(\bar{\nu})L_{BB}(\bar{\nu}, T_2) + O(\bar{\nu}) \quad (14)$$

where $L_{BB}(\bar{\nu}, T)$ is Planck's blackbody radiation function at temperature T. Even though the spectral response is theoretically the same for each pixel, in order to account for any residual non-uniformity in the FPA, the spectral response was calculated for each pixel.

The spectral gain for each pixel was very noisy towards the upper end of the detector's spectral range, owing to the fact that the blackbody signal was very low in that region, creating a low SNR. Due to this large amount of noise, the spectral gain curves for each pixel were smoothed using a ninth order polynomial. The ninth order polynomial was selected for ease of use; a three-piece cubic spline was able to fit the data with similar accuracy, but is not shown here.

As can be seen in Figure 13, the spectral gain curves contained atmospheric absorption features due to the path between the blackbody, abutting the front optic, and the detector. These absorption features are due to H₂O in the 1800 – 2000 cm⁻¹ (5 – 5.5 μm) region, and CO₂ in the 2250 – 2400 cm⁻¹ (4.2 – 4.4 μm) region. The H₂O absorption features were small enough to disregard the impact they had on the polynomial fit, however, the CO₂ absorption feature required masking of that spectral region. Figure 13 shows the average spectral response as well as the average of the

polynomial fit to each pixel. Figure 14 shows the spectral gain and offset for each pixel, as well as the average of each.

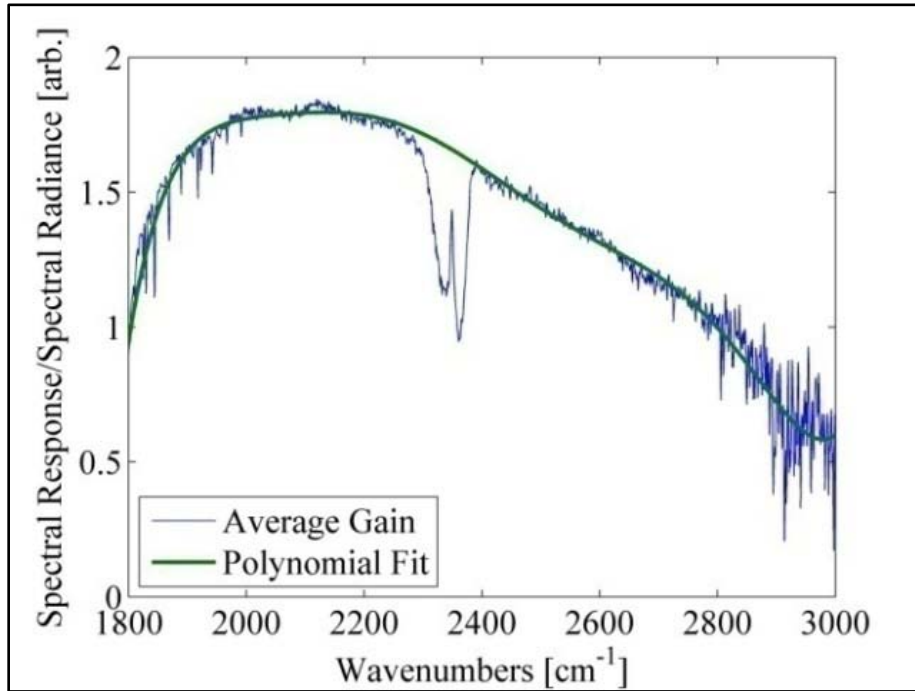


Figure 13. The spectral response of the InSb detector, averaged over all pixels, as well as the average polynomial fit to each pixel spectral response curve.

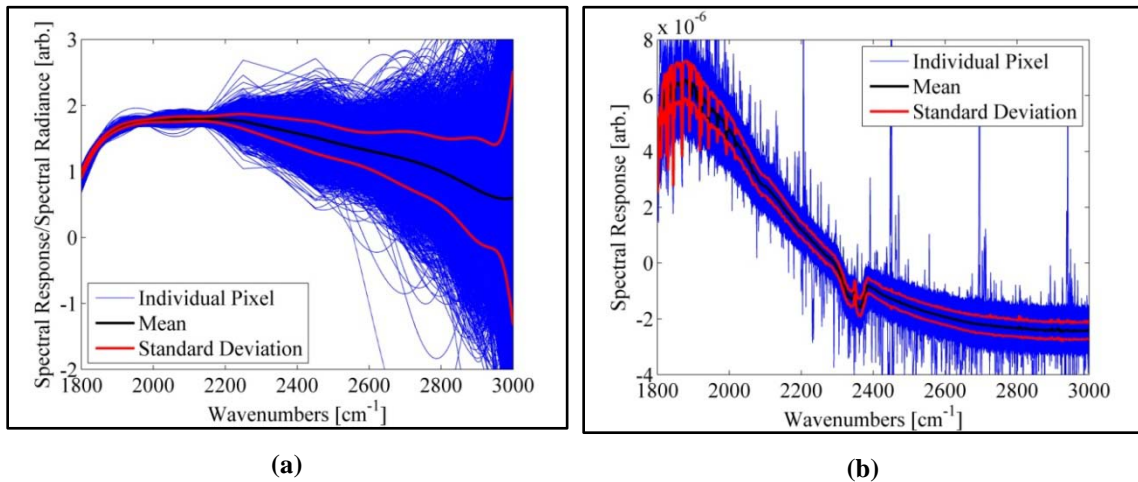


Figure 14. The spectral response (a) and spectral offset (b) of each pixel, as well as the average and standard deviation of all pixels. The outlying lines are due to bad pixels in the FPA. A ninth order polynomial was fit to the spectral response.

Application of these values allows for the radiometric calibration of the turbine engine exhaust data. Equation (15) shows the application of the spectral gain and offset to obtain calibrated spectra

$$C_{cal}(i, j, \bar{\nu}) = \frac{C_{nuc}(i, j, \bar{\nu}) - O(\bar{\nu})}{G(\bar{\nu})} \quad (15)$$

where $C_{cal}(i, j, \bar{\nu})$ is the calibrated spectrum at each pixel, and $C_{nuc}(i, j, \bar{\nu})$ is the non-uniformity corrected turbine engine exhaust spectra at each pixel. Figure 15 shows an example calibrated spectrum.

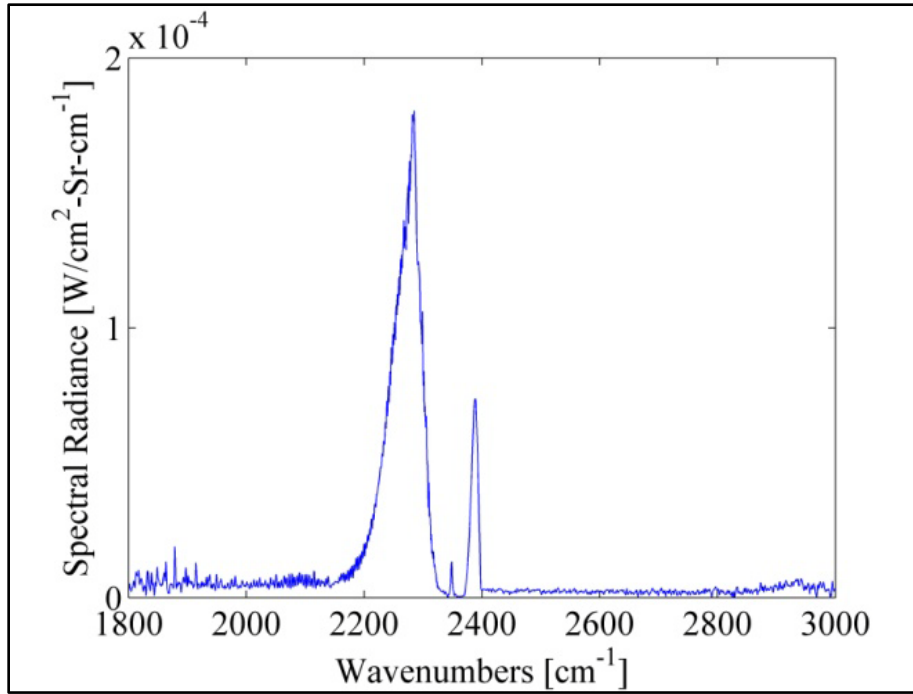


Figure 15. A spectrum collected by the FIRST-MWE. One hundred fifty datacubes were averaged, followed by the application of the NUC and spectral gain and offset. These data are at pixel (170, 32) of the diesel fuel type, 225 cm³/min fuel flow rate.

The calibration process was applied to both the average turbine engine exhaust plume hyperspectral datacube and the individual blackbody hyperspectral datacubes. The individual blackbody hyperspectral datacubes, once calibrated, were used to determine the NESR of the instrument. Telops has published a method of calculating the NESR of

their FIRST family of instruments [32], which was used here to produce an NESR for the FIRST-MWE. The standard deviation in the spectrum of a representative pixel, taken over all off the calibrated blackbody hyperspectral datacubes, represents the NESR.

Figure 16 shows the NESR computed by this method.

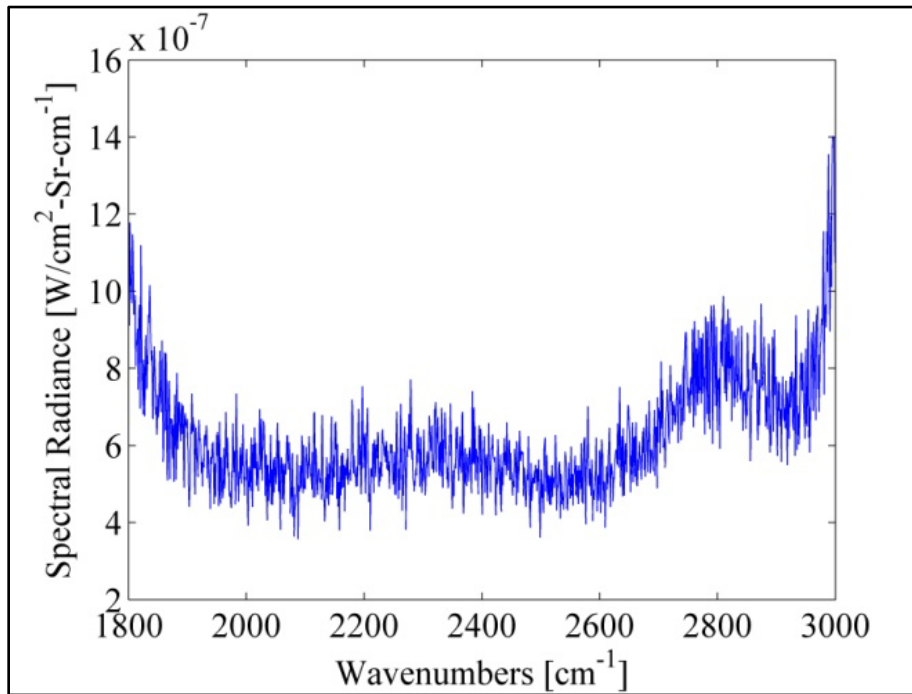


Figure 16. The NESR of the Telops FIRST-MWE.

Once the spectra have been calibrated, it is possible to begin analysis of the data. One final point on FPA characterization will be made prior to looking at the effects of a changing scene on the data. This topic addresses the unresolved causes of FPA non-uniformity.

Spectral Response and Photon Response Correlation.

It is interesting to note that the pixel-to-pixel photon response distributions, both single and two-point, were correlated to the spectral response of each pixel. It was originally thought that a proper NUC should remove this correlation entirely. Due to the

correlation between spectral gain and photon gain, it became evident that the NUC did not account for all pixel non-uniformity. A suggestion that the FPA exhibited higher order non-uniformity was made, along with a suggestion that differences in optical coating thickness could lead to the correlation. Although neither potential cause was fully explored, it was determined that by performing the two temperature non-uniformity correction, the correlation was greatly reduced. Figure 17 (a), shows an example of the correlation observed when performing a NUC without an offset. For the spectral gain, the spectral bin of peak response was selected, approximately 1970 cm^{-1} ($5.1 \mu\text{m}$).

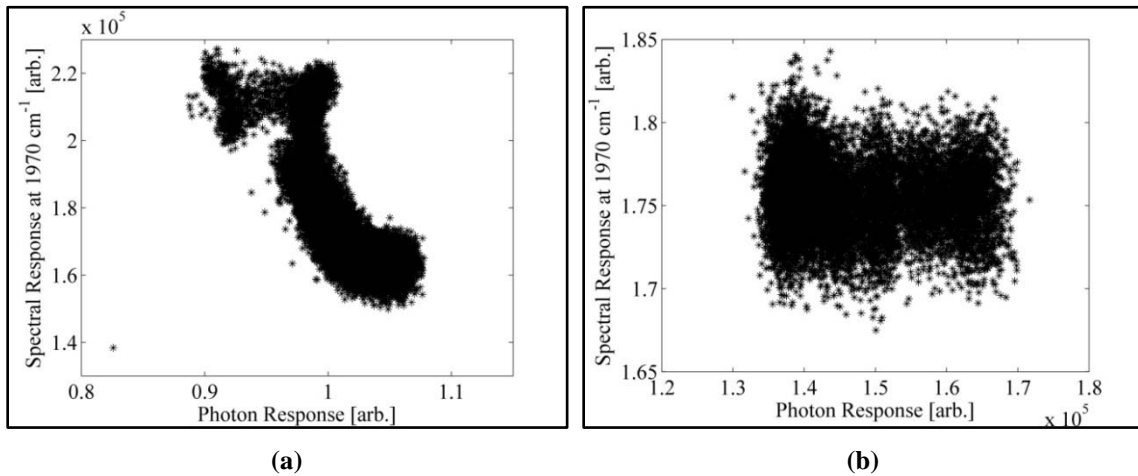


Figure 17. The photon response per pixel plotted against the spectral response per pixel in a peak emission region shows strong correlation between the two in the case when the offset is ignored (a), and shows very little correlation between the two in the case when the offset is included (b).

When the NUC was performed in the spectral domain and included an offset, the correlation between photon response and spectral response dramatically reduced. The correlation coefficient was originally greater than 0.8, and reduced to less than 0.08. Figure 17 (b) shows the photon response versus spectral response for the case of a two temperature NUC. The decrease in correlation is due to the better non-uniformity correction of the two temperature method. When performing the one temperature NUC,

not all causes of non-uniformity in the FPA were accounted for. When calculating the spectral gain and offset, the spectral gain incorporated residual non-uniformity, which caused the correlation. By including the offset term in the two temperature non-uniformity correction, a dramatic reduction in correlation between the photon response and spectral response was observed.

Scene Change Artifacts

In addition to factors that impact the data within the instrument, there are factors outside the instrument which will impact the quality of the data collected. Due to the nature of the object under observation, it was necessary to address the impact of a changing scene on the data.

Scene change artifacts (SCAs) are variations in the interferogram due to variations in the scene under observation which occur when the time required to collect a hyperspectral datacube is longer than the time constant of the scene. SCAs are not noise; they are a manifestation of the scene undergoing rapid changes in radiance, and thus are real phenomena. In this study, SCAs were a direct result of the highly turbulent nature of the turbine engine exhaust, in which non-uniform hot gas emissions from the turbine produced temporary localized pockets differing in total apparent radiance. Because it is not possible to separate SCAs from noise in a spectrum with SCAs, the result is an increase in spectral variation from that which would be obtained when observing a scene without SCAs. The impact of SCAs on the variation of a spectrum can be seen in Figure 18, which compares the NESR of the FIRST-MWE with a spectrum impacted by SCAs. The SCAs significantly increase the variation over the NESR of the instrument.

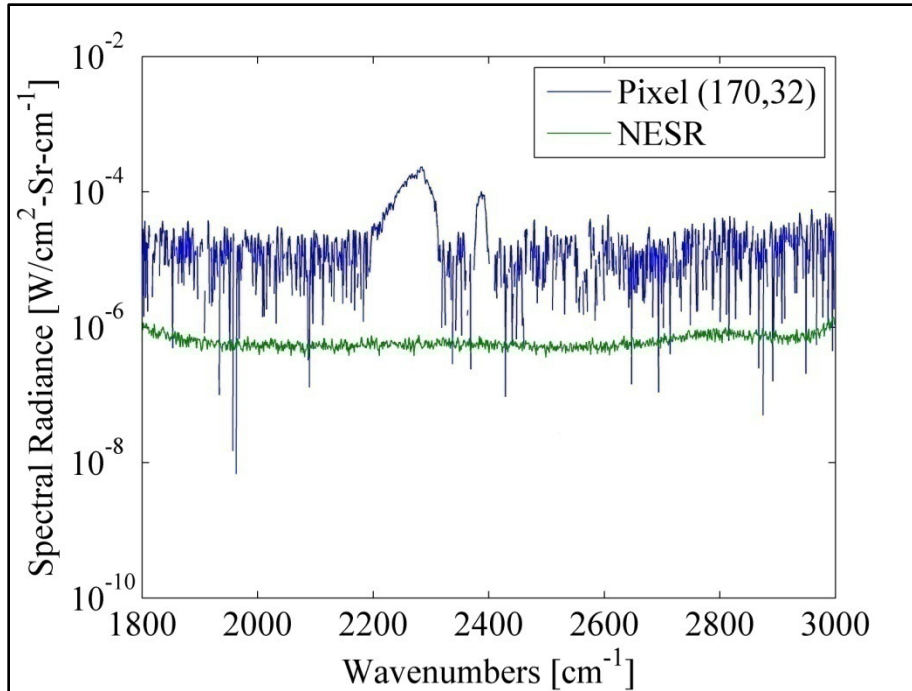
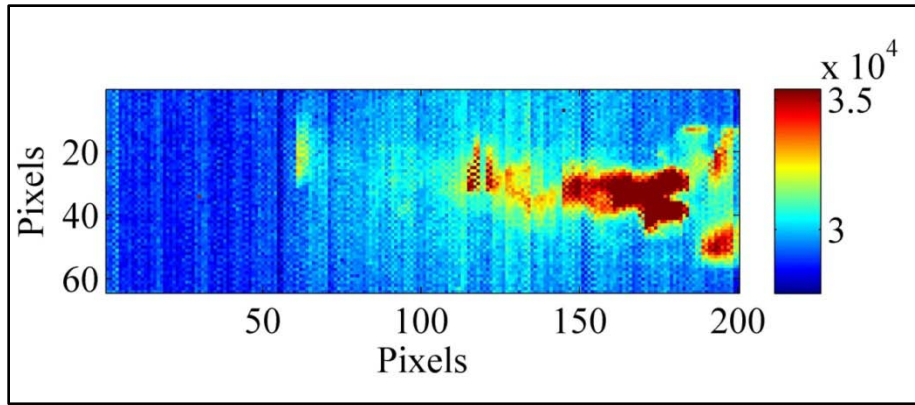


Figure 18. Visualization of the impact SCAs have on the variation in a spectrum, compared with the NESR of the instrument. The variation due to SCAs is much greater than the NESR. This data taken from diesel fuel, 225 cm³/min flow rate, pixel (170, 32).

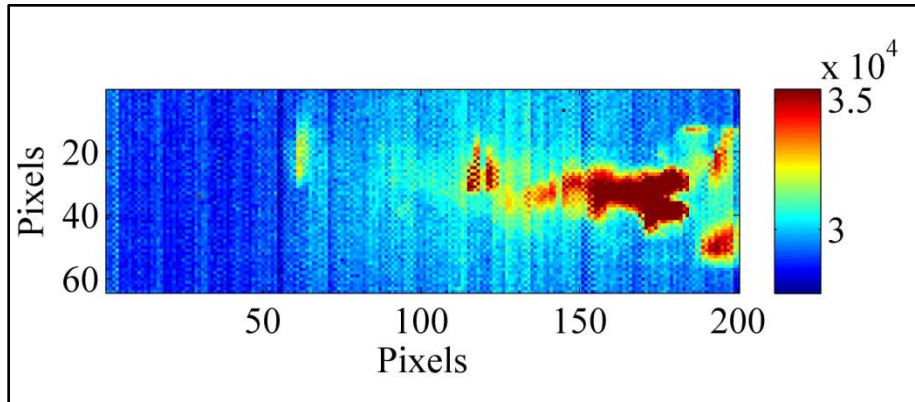
In order to produce high signal-to-noise ratio data for analysis, it was necessary to minimize the impact SCAs had on the data. Three methods were investigated for the purpose of increasing SNR in the spectra.

In this study, the time constant of the scene is too small for the Telops FIRST-MWE to collect a hyperspectral datacube free of SCAs. In the collection of a single hyperspectral datacube, the Telops FIRST-MWE captures a two-dimensional image at each OPD mirror position the same way a single-pixel FTS sweeps through each OPD mirror position. To achieve the 1-cm⁻¹ spectral resolution desired, the mirror necessarily swept through 18,956 mirror positions at a rate of approximately 250 μsec per OPD mirror position. Figure 19 demonstrates that the time constant of the turbine exhaust was

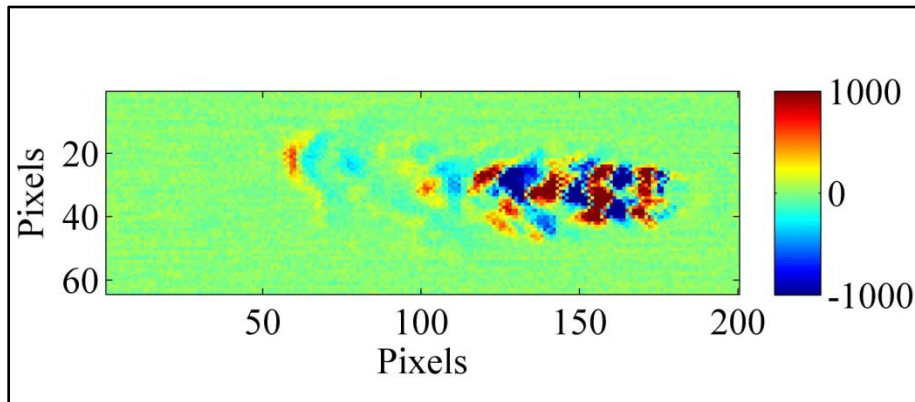
not only less than the time required to collect a hyperspectral datacube, it was less than the 250 μ sec required to collect data at each OPD mirror position.



(a)



(b)



(c)

Figure 19. The FPA at a single interferogram OPD mirror position (a), incremented by one OPD mirror position (b), and the difference between the two (c). Scene change between the OPD mirror positions is detectable.

In addition to this constant scene change created by localized pockets of total apparent radiance, occasional flare-ups from the turbine engine were observed, which can be characterized as intense, localized bursts of total apparent radiance. These flare-ups were of a short duration but very large in magnitude, producing peak values on the FIRST-MWE at OPD mirror positions other than the center-burst at ZPD. Figure 20 displays an interferogram from the diesel fuel, 225 cm³/min flow rate set, file 50684, pixel (170, 32) containing a flare-up around an OPD of 0.38 cm.

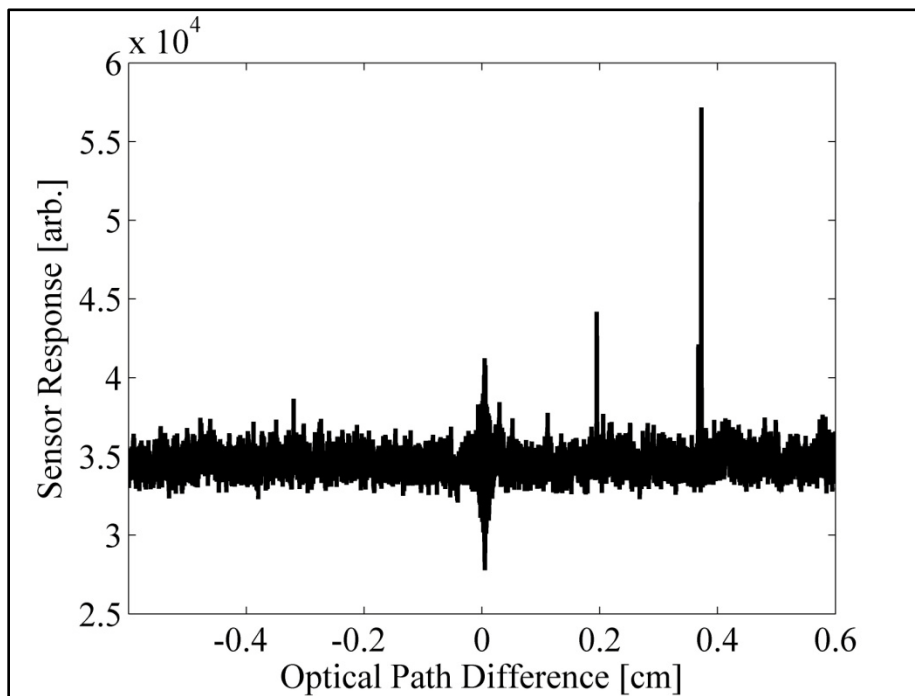
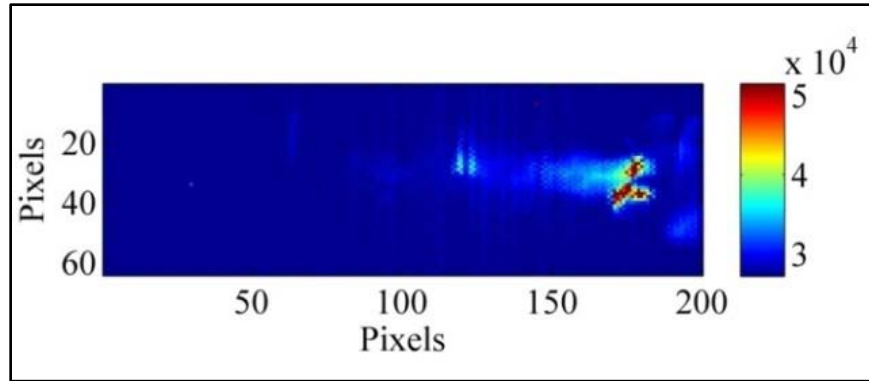
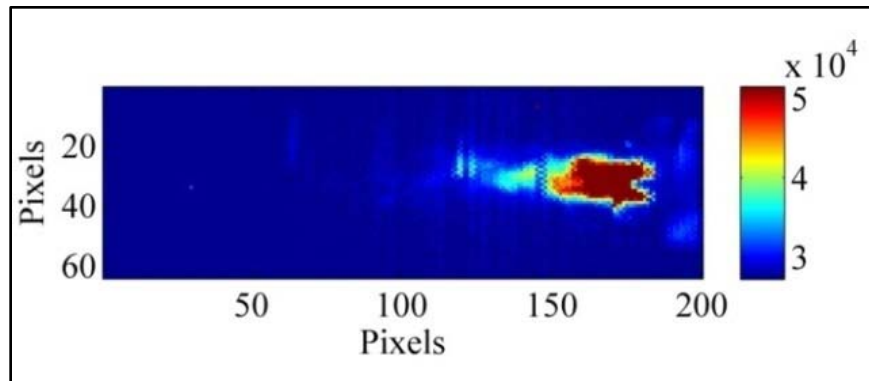


Figure 20. An interferogram taken from file with a flare-up at OPD mirror position 5882. The interferogram was taken from pixel (170, 32), diesel fuel with a flow rate of 225 cm³/min.

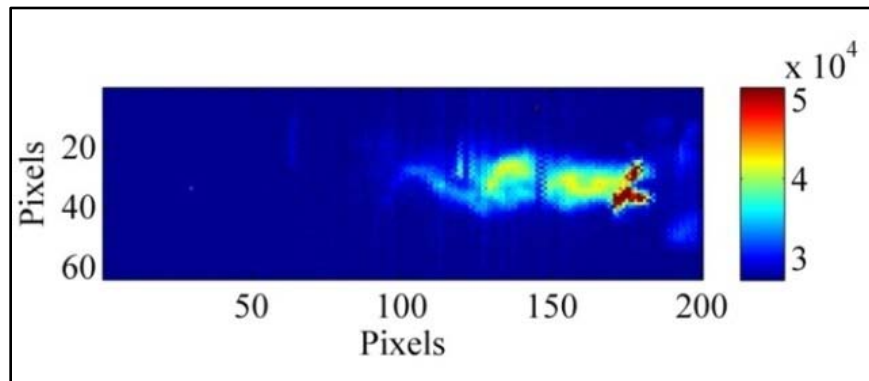
Figure 21 displays the FPA at OPD mirror position 5877, 5882, and 5887, showing the temporal and spatial propagation of the flare-up. The three images displayed are separated temporally by approximately 1.25 ms.



(a)



(b)



(c)

Figure 21. FPA images showing the temporal and spatial propagation of the flare up. The top image (a) is from OPD mirror position 5877, the middle image (b) is from OPD mirror position 5882, and the bottom image (c) is from OPD mirror position 5887. Each image is separated temporally by approximately 1.25 ms.

Due to the extremely short time constant of the turbine engine exhaust, it is not possible to avoid the presence of SCAs in the data. Without considering and accounting

for these SCAs, it would not be possible to perform further analysis of the data. Figure 22 displays the uncalibrated spectrum from pixel (170, 32), produced from the raw data without averaging to account for SCAs.

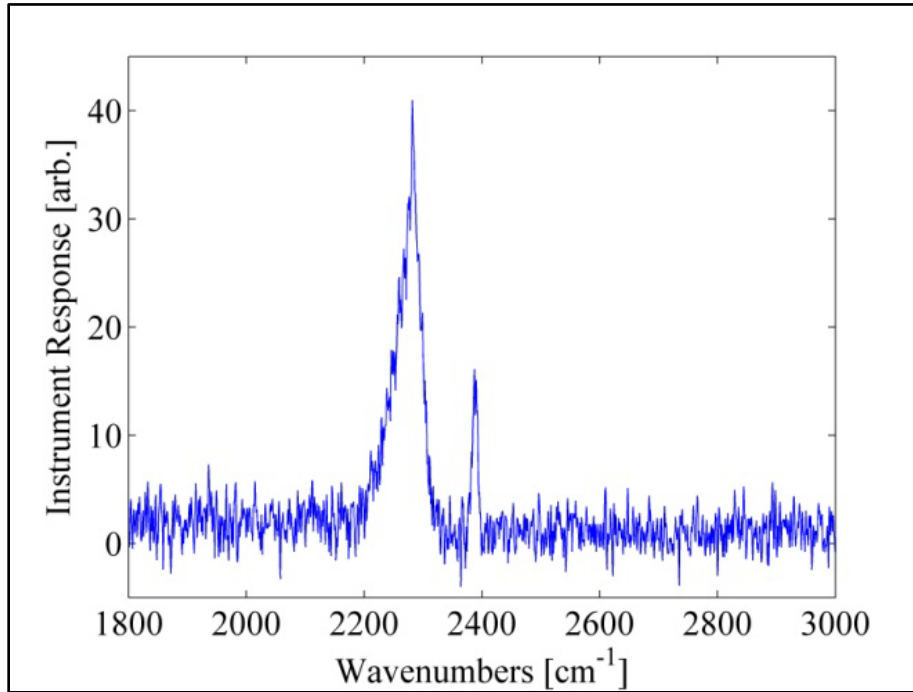
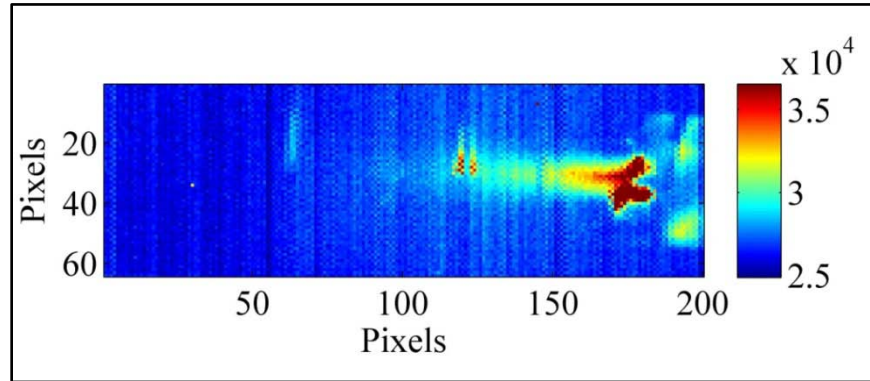


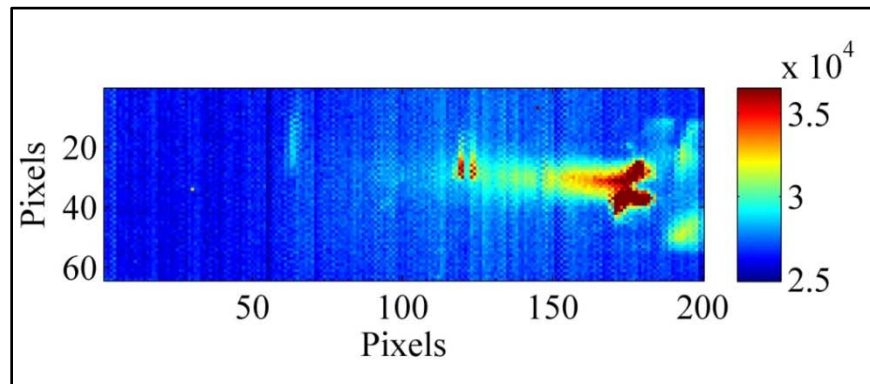
Figure 22. Uncalibrated spectrum showing the poor SNR obtained without accounting for SCAs. The spectrum was taken from pixel (170, 32), diesel fuel with a flow rate of 225 cm³/min.

Methods of accounting for SCAs have been discussed elsewhere [11, 27], however, these center on the prevention or reduction of SCAs without further analysis. Prevention is not a viable method in this scenario; however, it has been shown that by averaging across the interferogram position values for each pixel, a picture which appears to represent a constant view of the plume emerges [27]. This as can be seen in Figure 23, which shows the average over all OPD positions for two hyperspectral datacubes, and the difference between them. Both of these hyperspectral datacubes were taken from the diesel fuel, 225 cm³/min data set, in which there were 311 hyperspectral datacubes

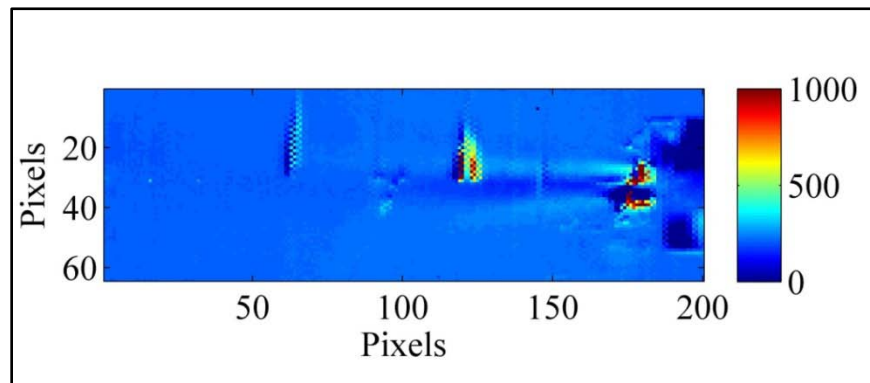
collected, numbered 50212 – 50428 and 50612 – 50705. The two shown in Figure 23 are hyperspectral datacubes 50616 and 50684. The scene observed for these two turbine engine exhaust plume has a very similar distribution for all datacubes in this data set.



(a)



(b)



(c)

Figure 23. The FPA images show the average over the interferogram dimension of hyperspectral datacube 50616 (a) and hyperspectral datacube 50684 (b), and the difference between the two (c). Both were collected against the turbine engine running diesel fuel at a $225 \text{ cm}^3/\text{min}$ fuel flow rate.

Because it removes all spectral information, an average along the interferogram dimension is not useful except to show the average total apparent radiance of the turbine engine exhaust plume. In order to improve the SNR to a level sufficient to produce clean spectra, it is necessary to reclaim the SNR lost due to scene change. It has been shown that averaging over multiple datacubes increases the SNR of the data, which carries the implication that the SCAs are stochastic phenomena [27]. However, it has been shown that flare-ups occur in addition to the normal SCAs that plague interferograms. Unlike normal SCAs, which were both positive- and negative-valued relative to the mean signal, flare-ups are only positive-valued. Figure 24 shows the distribution of values for one pixel and one interferogram position each, across all datacubes. Figure 24 (a) is at an interferogram point with no flare-ups, while Figure 24 (b) is at a point with two flare-ups. Figure 24 (a) resembles a zero-mean, normally distributed distribution, while Figure 24 (b) does not.

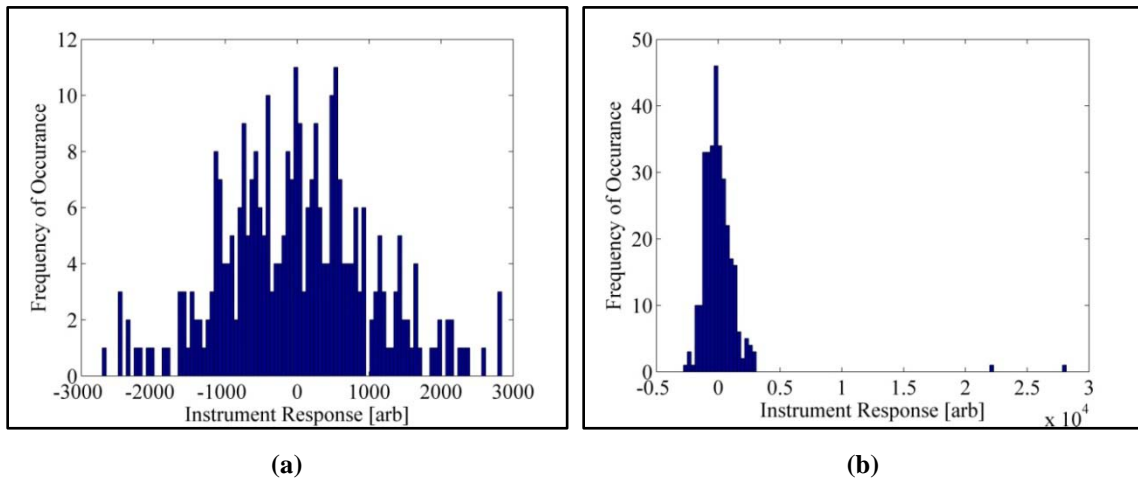
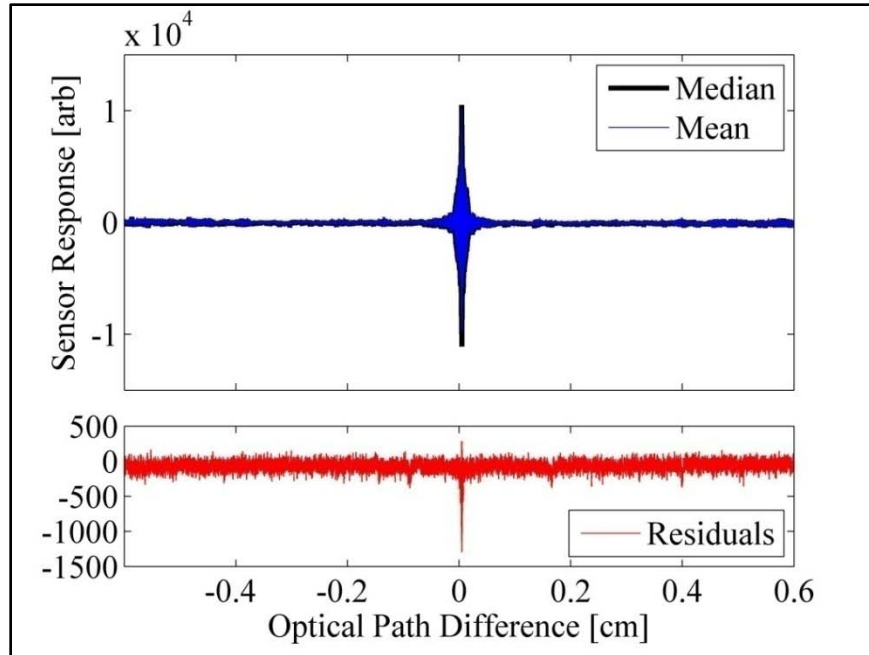


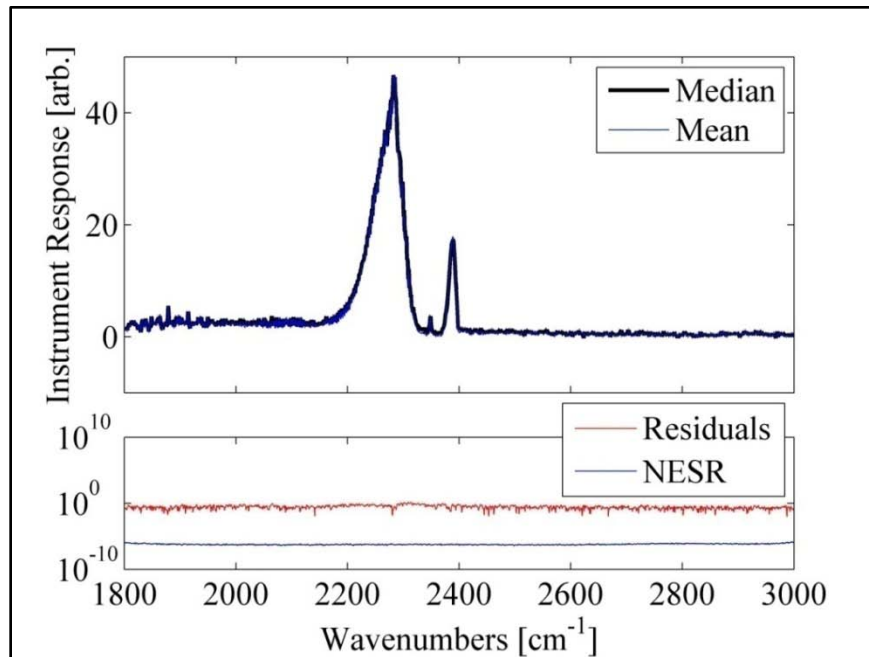
Figure 24. Histograms of an OPD mirror position without flare-ups (a), and an OPD mirror position with two flare-ups (b). Each data point in the histogram is a hyperspectral datacube at the same pixel and OPD mirror position. Both histograms only used datacubes taken while observing the turbine running diesel fuel with a 225 cm³/min fuel flow rate.

A chi-square goodness-of-fit test shows that the distribution of Figure 24 (a) is reasonably Gaussian, with a p-value of 0.40, while that of Figure 24 (b) fails the null hypothesis, with a p-value less than 0.05; the flare-ups bias the data away from zero-mean. In order to avoid this bias and obtain a less noisy spectrum, it would appear to be necessary to perform either data filtering to remove flare-ups from the dataset before computing a mean over the datacubes. This was determined not to be the case. Figure 25 (a) is a plot of both the mean and median interferogram, taken over 156 datacubes, while Figure 25 (b) is a plot of the corresponding mean and median spectra. The differences between the two spectra are on the order of the NESR of the instrument.

While it is apparent that the mean interferogram contains biased data corresponding to locations of flare-ups, and that the median interferogram is much cleaner in that respect, this does not substantially impact the corresponding spectra. Similarly, when a filter is applied to remove flare-ups and all other SCAs more than four standard deviations from the mean, much cleaner mean interferograms are produced. However, any differences become insignificant when converted to spectra. Additionally, data filtering has no appreciable difference when taking the median value. Due to the infrequent occurrence of flare-ups, data filtering does not significantly impact the corresponding spectra. Figure 26 is a plot of both the filtered and unfiltered mean interferogram, while Figure 27 is a plot of the corresponding filtered and unfiltered mean spectra, with residuals.



(a)



(b)

Figure 25. The mean (blue) and median (black) interferogram for pixel (170, 32), taken over 156 hyperspectral datacubes (a). The mean interferogram is biased towards positive values, while the median interferogram is not. The mean (blue) and median (black) spectrum for pixel (170, 32) taken over 156 hyperspectral datacubes, with the Residuals and NESR of the instrument (b). The spectra are very similar. Both (a) and (b) were taken from hyperspectral datacubes observing diesel fuel with a flow rate of 225 cm³/min.

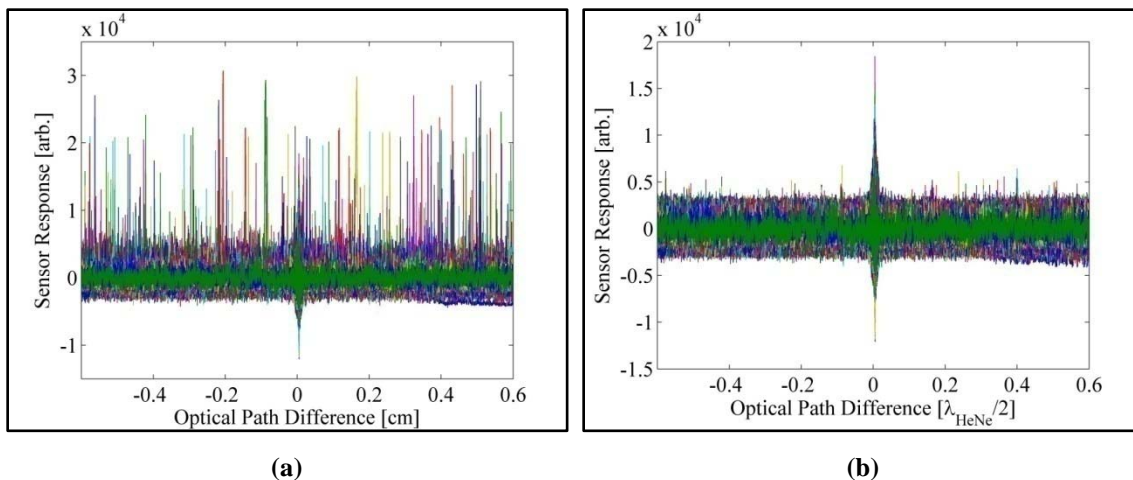


Figure 26. (a) Unfiltered interferograms of pixel (170, 32), from 156 hyperspectral datacubes, and (b) the same hyperspectral datacubes, filtered to remove all points more than four standard deviations from the mean. These interferograms were taken from hyperspectral datacubes observing diesel fuel with a flow rate of 225 cm³/min.

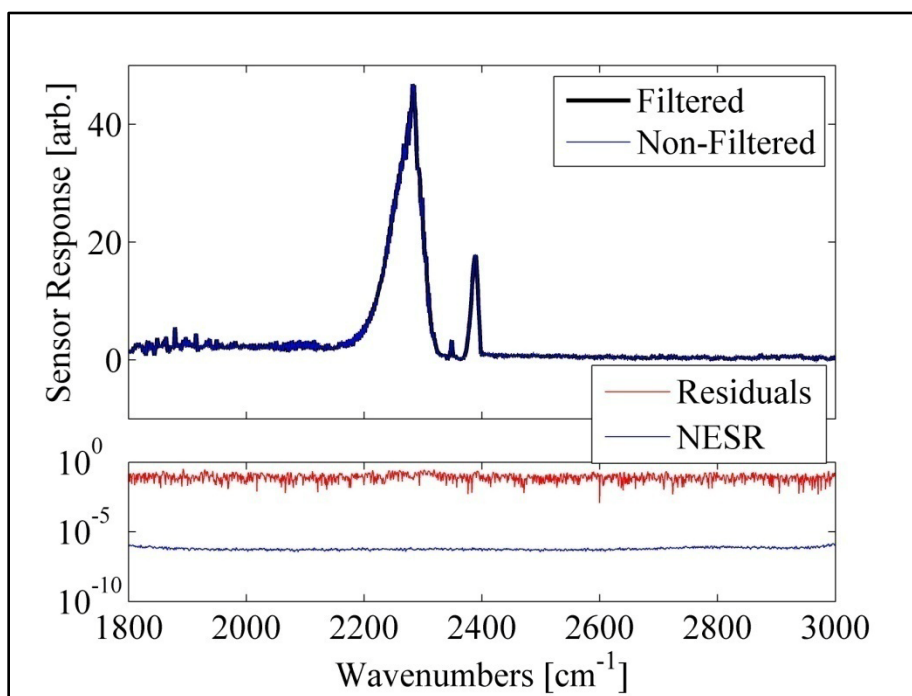


Figure 27. Mean spectra from filtered (black) and unfiltered (blue) interferograms. The difference between the two (red) is negligible. These spectra were taken from hyperspectral datacubes observing diesel fuel with a flow rate of 225 cm³/min.

Summary

The important factors related to characterization of the Telops FIRST-MWE were presented. The FPA characterization tools necessary to produce calibrated spectra, such as the NUC and the spectral gain and offset of the detector, were developed, and a brief analysis of the impact SCAs have on data was presented. These tools enable the calibrated spectra to be analyzed for the uncertainty in the calibration, and fit a model to the data to extract temperature and chemical species concentration pathlength distributions. The tools necessary for these steps, namely error analysis and the radiative transfer model, are developed next.

V. Data Processing

With the incorporation of results obtained from the non-uniformity correction, spectral gain and offset correction, and scene change artifact reduction, calibrated data can be used to extract information from the hyperspectral datacubes. In order to determine the uncertainty associated with the calibrated spectra, which represents one measure of the quality of the calibration, an error analysis was performed. The error analysis also enabled the determination of the main sources of uncertainty, to target areas for future refinement of the implemented calibration techniques. In order to extract spatial distributions of temperature and chemical species concentration pathlength, a simple radiative transfer model was constructed to fit to the calibrated data. This simple radiative transfer model is developed here.

Error Analysis

Due to the inherent nature of remote sensing, there is uncertainty in the measurement of a source. Instrument noise, SCAs, and other temporally varying parameters of the scene, such as atmospheric constituents, pressures and temperatures, contribute to variations in the data. Averaging of the raw hyperspectral datacubes, which averages the variations as well, requires some consideration, and is discussed in Appendix B. One advantage to averaging in the spectral domain is that it removes the need to propagate error through the Fourier transform equation. For that reason, despite the requisite increase in computation time, this analysis was completed using the spectral domain averaging technique.

When calculating the mean spectra, a standard deviation of the spectral information of each pixel is also calculated, and can be used to represent the uncertainty in the measurement. This is done for both the blackbodies and the turbine engine exhaust data. Figure 28 shows standard deviation from the mean for a representative pixel, representing the average of two hundred spectra. The spectral features of H₂O and CO₂, observed at 1800 – 2000 cm⁻¹ (5 – 5.5 μm) and 2300 – 2400 cm⁻¹ (4.2 – 4.3 μm), respectively, are due to atmospheric absorbance along the path inside the instrument, between the front optic and the detector.

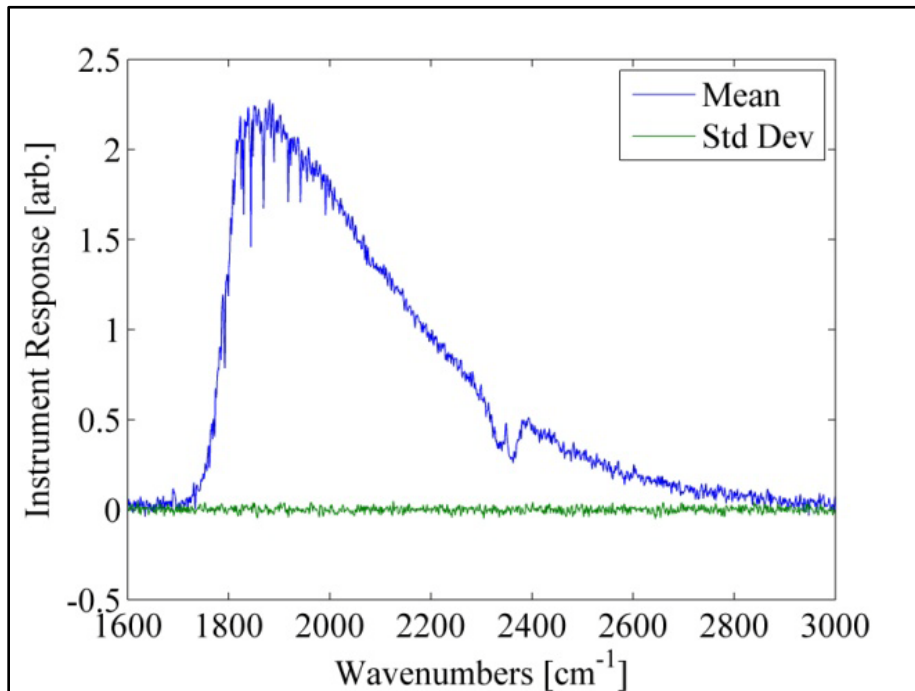


Figure 28. The average, uncalibrated spectrum of pixel (170, 32) from an 80 °C blackbody (blue), with standard deviation (green).

The standard deviation of the blackbody shown in Figure 28 was used to determine the uncertainty in the non-uniformity correction photon gain term. The equation for calculating the photon gain is given by

$$g(i, j) = \frac{\overline{C_{obs,1}}(i, j, T_1) - \overline{C_{obs,2}}(i, j, T_2)}{\overline{L_{BB}}(T_1) - \overline{L_{BB}}(T_2)} \quad (16)$$

where $g(i, j)$ is the non-uniformity correction photon gain; $\overline{C_{obs,1}}(i, j, T_1)$ and $\overline{C_{obs,2}}(i, j, T_2)$ are the hyperspectral datacubes integrated over the spectrum at blackbody temperatures $T_1 = 80$ °C and $T_2 = 20$ °C; $\overline{L_{BB}}(T)$ is Planck's temperature-dependant blackbody radiation equation. The terms in Equation (16) have an uncertainty associated with them, resulting from the variation across the blackbody files. The equations determining the uncertainty are given by

$$\overline{C_{obs}}(i, j, T) = \sum_{\bar{v}=1}^N C_{obs}(i, j, T, \bar{v}) \quad (17)$$

$$\sigma_{\overline{C_{obs}}}(i, j, T)^2 = \sum_{\bar{v}=1}^N \sigma_{C_{obs}}(i, j, T, \bar{v})^2 \quad (18)$$

where $C_{obs}(i, j, T, \bar{v})$ is the individual pixel and spectral position of the observed signal for a given temperature, and N is the number of spectral bins in the spectrum. The variance of each pixel in the hyperspectral datacube integrated over the spectrum is given by $\sigma_{\overline{C_{obs}}}(i, j, T)^2$, where $\sigma_{C_{obs}}(i, j, T, \bar{v})^2$ is the variance about each spectral bin. There is no uncertainty associated with Planck's equation.

The equation for the variance in the photon response is given by

$$\sigma_g(i, j)^2 = \sigma_{\overline{C_{obs}}}(i, j, T_1)^2 \left[\frac{1}{\overline{L_{BB}}(T_1) - \overline{L_{BB}}(T_2)} \right]^2 + \sigma_{\overline{C_{obs}}}(i, j, T_2)^2 \left[\frac{-1}{\overline{L_{BB}}(T_1) - \overline{L_{BB}}(T_2)} \right]^2 \quad (19)$$

where $\sigma_g(i, j)^2$ is the variance in the photon response for each pixel.

The equation for calculating the dark current offset is given by

$$o(i, j) = \overline{C_{obs,1}}(i, j, T_1) - g(i, j) \overline{L_{BB}}(T_1) \quad (20)$$

and the equation for the variance in the dark current offset is given by

$$\sigma_o(i, j)^2 = \sigma_{\overline{C_{obs}}}(i, j, T_1)^2 + \sigma_g(i, j)^2 [\overline{C_{obs,1}}(i, j, T_1)]^2 \quad (21)$$

Equation (10) has been rewritten here as a reminder of the application of the non-uniformity correction, which can be utilized for both blackbodies and turbine engine exhaust data,

$$C_{nuc}(i, j, \bar{\nu}) = \frac{C_{obs}(i, j, \bar{\nu}) - o(i, j)}{g(i, j)} \quad (10)$$

$$\sigma_{C_{nuc}}(i, j, \bar{\nu})^2 = \sigma_{C_{obs}}(i, j, \bar{\nu})^2 \left[\frac{1}{g(i, j)} \right]^2 + \sigma_o(i, j)^2 \left[\frac{-1}{g(i, j)} \right]^2 + \sigma_g(i, j)^2 \left[\frac{-C_{obs}(i, j, \bar{\nu})}{g(i, j)^2} \right]^2 \quad (20)$$

where $C_{nuc}(i, j, \bar{\nu})$ is the non-uniformity corrected spectrum at each pixel, $C_{obs}(i, j, \bar{\nu})$ is the raw hyperspectral datacube, averaged over all files of the same fuel type and flow rate. The variance about each spectral position at each pixel is given by $\sigma_{C_{nuc}}(i, j, \bar{\nu})^2$.

Calculation of the variance of the spectral gain and offset is similar. Recall Equation (12), the spectrum observed by the sensor, after non-uniformity correction, from a blackbody of temperature T, is given by

$$C_{nuc}(\bar{\nu}, T) = G(\bar{\nu})L_{BB}(\bar{\nu}, T) + O(\bar{\nu}) \quad (12)$$

where $C_{nuc}(\bar{\nu})$ is the observed spectrum, uniform across all pixels due to the non-uniformity correction, $G(\bar{\nu})$ is the spectral gain term, $L_{BB}(\bar{\nu}, T)$ is Plank's spectral radiance from a blackbody at temperature T, and $O(\bar{\nu}) = G(\bar{\nu}) L_{inst}(\bar{\nu})$ is the spectral offset term, a combination of the spectral gain and the instrument self-emission apparent spectral radiance. By using a blackbody at two temperatures, the spectral gain and offset were obtained,

$$G(\bar{\nu}) = \frac{C_{nuc}(\bar{\nu}, T_1) - C_{nuc}(\bar{\nu}, T_2)}{L_{BB}(\bar{\nu}, T_1) - L_{BB}(\bar{\nu}, T_2)} \quad (21)$$

$$O(\bar{\nu}) = C_{nuc,1}(\bar{\nu}, T_1) - G(\bar{\nu})L_{BB}(\bar{\nu}, T_1) \quad (22)$$

The equations for calculating the variance in each is similar to that computed previously for the NUC gain,

$$\sigma_G(\bar{\nu})^2 = \sigma_{Cnuc}(\bar{\nu}, T_1)^2 \left[\frac{1}{L_{BB}(\bar{\nu}, T_1) - L_{BB}(\bar{\nu}, T_2)} \right]^2 + \sigma_{Cnuc}(\bar{\nu}, T_2)^2 \left[\frac{-1}{L_{BB}(\bar{\nu}, T_1) - L_{BB}(\bar{\nu}, T_2)} \right]^2 \quad (23)$$

$$\sigma_O(\bar{\nu})^2 = \sigma_{Cnuc}(\bar{\nu}, T_1)^2 + \sigma_G(\bar{\nu})^2 [-L_{BB}(\bar{\nu}, T_1)]^2 + \sigma_{Lbb}(\bar{\nu}, T_1)^2 [-G(\bar{\nu})]^2 \quad (24)$$

where $\sigma_G(\bar{\nu})^2$ is the variance in the spectral response, and $\sigma_O(\bar{\nu})^2$ is the variance in the spectral offset.

Because the spectral gain curve is known to be a smooth function, the spectral gain of each pixel was fit to a ninth order polynomial in order to smooth out the noise.

Thus, the equation for the gain becomes

$$G(\bar{\nu}) = C_8\bar{\nu}^8 + C_7\bar{\nu}^7 + C_6\bar{\nu}^6 + C_5\bar{\nu}^5 + C_4\bar{\nu}^4 + C_3\bar{\nu}^3 + C_2\bar{\nu}^2 + C_1\bar{\nu}^1 + C_0\bar{\nu}^0 \quad (25)$$

where $C_0 - C_8$ are the polynomial coefficients. To remove computational complexity, the previous calculation for the spectral gain variance is used, *i.e.* Equation (23). The uncertainty associated with applying the spectral gain and offset to the blackbody and turbine engine exhaust data is straightforward. The variance in the calibrated spectrum at each pixel in the hyperspectral datacube is

$$\sigma_{Ccal}(i, j, \bar{\nu})^2 = \sigma_{Cnuc}(i, j, \bar{\nu})^2 \left[\frac{1}{G(\bar{\nu})} \right]^2 + \sigma_O(\bar{\nu})^2 \left[\frac{-1}{G(\bar{\nu})} \right]^2 + \sigma_G(\bar{\nu})^2 \left[\frac{-Cnuc(i, j, \bar{\nu}) + O(\bar{\nu})}{G(\bar{\nu})^2} \right]^2 \quad (26)$$

Figure 29 shows an example calibrated spectrum compared against the theoretical planckian at the same temperature, as well as the residuals, the standard deviation of the calibrated data, and the NESR of the FIRST-MWE. The CO₂ absorption feature in Figure 29, observed at 2300 – 2400 cm⁻¹ (4.2 – 4.3 μm), is due to atmospheric absorbance along the path inside the instrument, between the front optic and the detector. The increased variation in the spectrum is due to SCAs because this is a pixel from a single hyperspectral datacube, not an average.

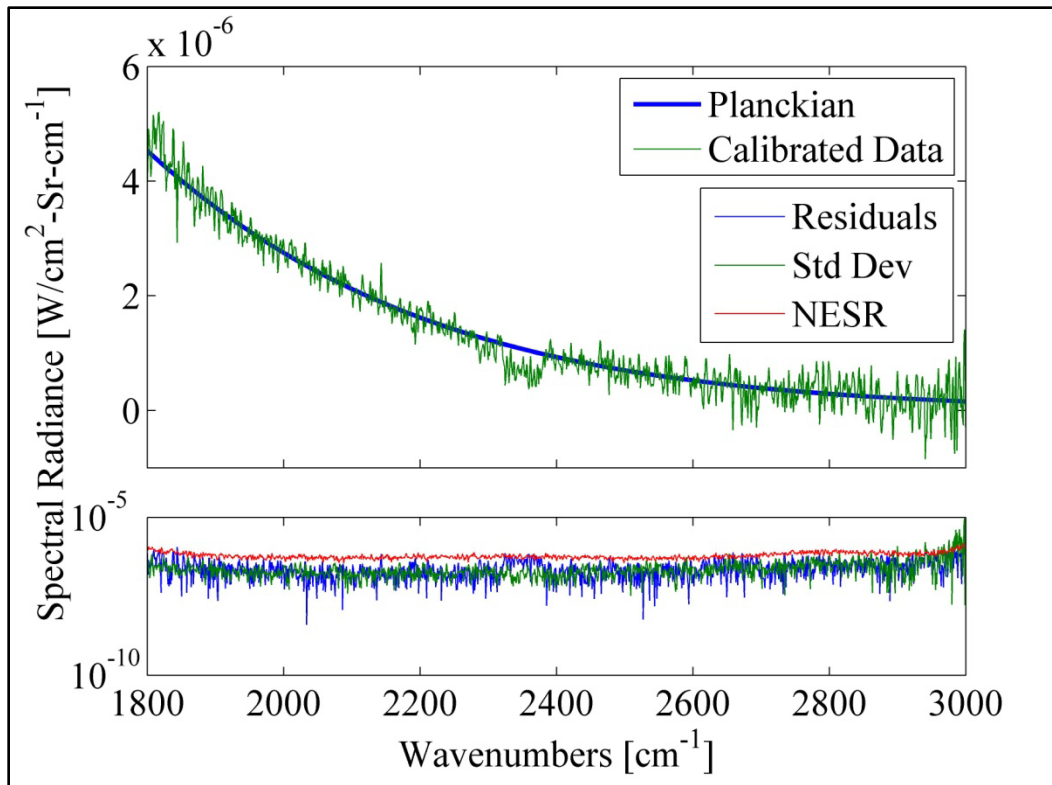


Figure 29. A calibrated spectrum of pixel (170, 32) from a blackbody (green) with the theoretical planckian (blue). The residuals (blue, subplot) of the calibrated spectrum against the planckian are on the same order as the uncertainty in the calibration (green, subplot), and the NESR of the FIRST-MWE (red, subplot).

In this way, the calibrated hyperspectral datacubes can be bounded by the uncertainty due to the variations in measurement. These calibrated datacubes can now be used in a model fitting algorithm in order to obtain distributions of temperature and chemical species concentration pathlength.

Model Production

In order to show the capability of the Telops FIRST-MWE to extract spatial distributions of temperature and chemical species concentration pathlength, it is necessary to develop a model that can be fit to the data. In order to use the model to extract physical properties from the plume, it is not sufficient to simply fit a curve to the

data; instead, it is necessary to build a model using the radiative transfer equations of the experimental setup in order to extract accurate physical information from the spectrum, such as plume temperature and chemical species concentration pathlengths. The quality and fidelity of the model will determine the quality of the temperature and chemical species concentration predictions at each pixel.

Development of the Spectral Model.

The spectrum of each pixel in the calibrated hyperspectral datacube depends on many parameters which vary along the path between the FIRST-MWE detector and the cooled blackbody background. The temperature of the cooled blackbody, the temperatures of the turbine engine exhaust plume, the absorption and emission coefficients of each chemical species, as well as their concentration, and the properties of the atmosphere between the two, such as temperature, pressure, and chemical species concentration, all impact the shape of the spectrum. Additionally, the temporal evolution of the plume causes variations in spectral radiance per pixel, adding complexity to the interpretation of a temporally averaged spectrum.

As a first step in the modeling process, two assumptions were made: the plume may be adequately modeled using a single temperature, and the average spectrum will be approximately represented by spectral emissions at an average temperature and concentration. The average radiance of a temporally evolving emission spectrum is

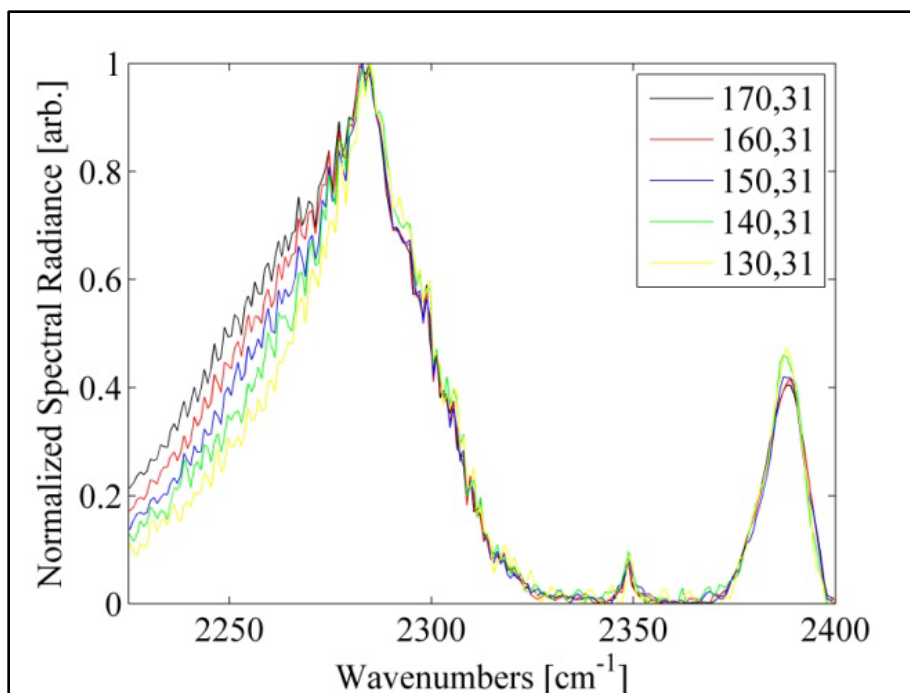
$$\langle \varepsilon(\bar{\nu}, T) L_{BB}(\bar{\nu}, T) \rangle = \varepsilon(\bar{\nu}, \bar{T}) L_{BB}(\bar{\nu}, \bar{T}) \quad (27)$$

where $\varepsilon(\bar{\nu}, T)$ is the spectral emissivity of the plume, which depends on temperature, and, although not shown, chemical species concentration; $L_{BB}(\bar{\nu}, T)$ is the planckian function;

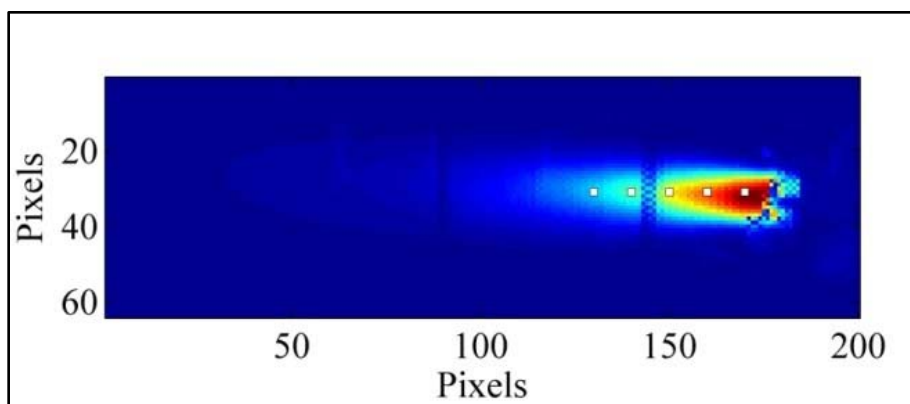
$\varepsilon(\bar{\nu}, \bar{T})L_{BB}(\bar{\nu}, \bar{T})$ is a radiance spectrum produced from the average temperature and chemical species concentrations.

The two assumptions stated above are required at this early stage of model maturity in order to obtain reasonable results within a practical timeframe. A detailed analysis is required to determine the accuracy and validity of these assumptions, which has not been accomplished at this time. Therefore, the uncharacterized assumptions that a temporally evolving spectrum can be represented by a single average temperature and chemical species concentration will have an uncharacterized impact on the values extracted by the model.

Figures 30 and 31 illustrate an example of one way in which the scene parameters impact the spectrum, the phenomenon of broader CO₂ emission spectra for pixels closer to the engine exhaust exit plane. This widening of the CO₂ emission line is due to higher rotational temperatures closer to the exit plane, moving energy into higher rovibrational transitions, which is consistent with the Maxwell-Boltzmann distribution. This phenomenon can be observed at both high and low resolution, however, by comparing the spectra collected at 1 cm⁻¹ with the spectra collected at 8 cm⁻¹, it is possible to gain a sense of the advantage of increased spectral resolution; through visual inspection, it is apparent that the high resolution data is better able to show the spectral widening with temperature. The high and low resolution normalized spectra can be seen in Figure 30 (a) and Figure 31 (a), respectively, which show the widening of the CO₂ emission profile for higher temperatures. The high and low resolution spectra correspond to pixels identified in Figure 30 (b) and Figure 31 (b), respectively.

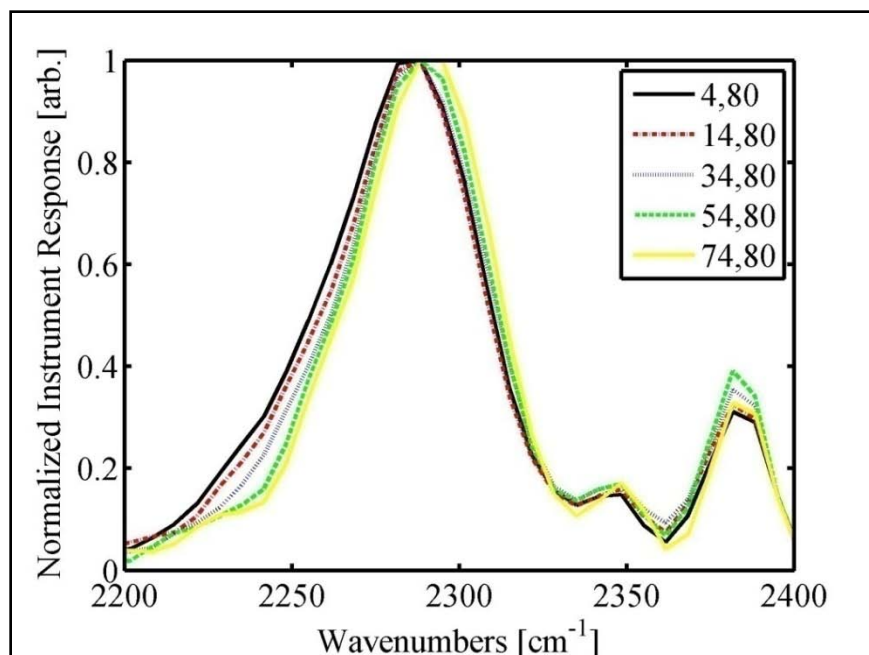


(a)

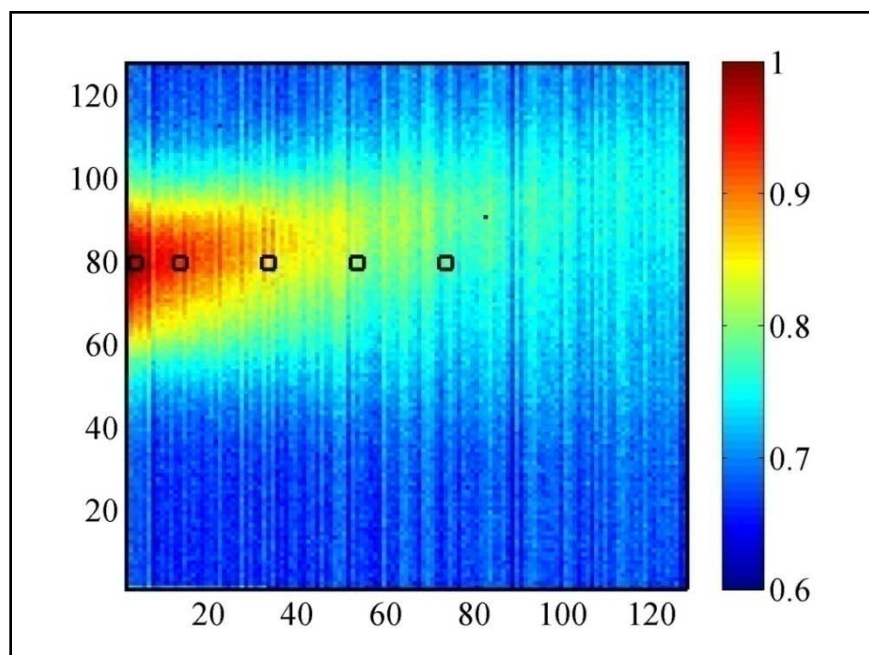


(b)

Figure 30. Peak-normalized calibrated spectra at 1 cm^{-1} resolution from the 5 November 2008 experimental campaign are shown overlaid (a), and correspond to the white pixels within the plume image (b). These demonstrate the phenomenon of higher temperatures moving the energy into higher ro-vibrational transitions according to the Maxwell-Boltzmann distribution, and the increased ability to discern the temperature differences at higher resolution.



(a)



(b)

Figure 31. Peak-normalized calibrated spectra at 8 cm^{-1} resolution from the 1 July 2008 experimental campaign are shown overlaid (a), and correspond to the black outlined pixels within the plume image (b) [27]. These demonstrate the phenomenon of higher temperatures moving the energy into higher ro-vibrational transitions according to the Maxwell-Boltzmann distribution, and the increased ability to discern the temperature differences at higher resolution.

If all parameters were known, it would be possible, by incorporating all of the elements impacting the shape of the spectrum into a model, to replicate the calibrated spectrum observed at each pixel. As in most remote sensing applications, it was not feasible to obtain *in situ* measurements of all necessary parameters at each pixel along the entire path between the background and detector. Without the knowledge of exact temperatures, pressures, and chemical species concentrations in the plume or along the path between the plume and sensor, it becomes necessary to search for the best fit of the model to the data, fitting certain key parameters such as chemical species concentrations and temperatures of the plume at each pixel, and fitting chemical species concentrations in the atmosphere for the entire scene. Without considering re-emission, the general form of this radiative transfer model is

$$\begin{aligned}
L_{obs}(i, j, \bar{\nu}, T_{atm,1}, T_{atm,2}, T_{back}, T_{plm}) = & \\
& \varepsilon_{back} L_{BB}(\bar{\nu}, T_{back}) \tau_{atm,1}(\bar{\nu}, T_{atm,1}) \prod_n \left(\tau_{plm,n}(i, j, \bar{\nu}, T_{plm,n}) \right) \tau_{atm,2}(\bar{\nu}, T_{atm,2}) \\
& + \varepsilon_{atm,2}(\bar{\nu}, T_{atm,2}) L_{BB}(\bar{\nu}, T_{atm,2}) \prod_n \left(\tau_{plm,n}(i, j, \bar{\nu}, T_{plm,n}) \right) \tau_{atm,2}(\bar{\nu}, T_{atm,2}) \\
+ \sum_n \left[\varepsilon_{plm,n}(i, j, \bar{\nu}, T_{plm,n}) L_{BB}(\bar{\nu}, T_{plm,n}) \prod_{m>n} \left(\tau_{plm,m}(i, j, \bar{\nu}, T_{plm,m}) \right) \tau_{atm,2}(\bar{\nu}, T_{atm,2}) \right] & \\
& + \varepsilon_{atm,1}(\bar{\nu}, T_{atm,1}) L_{BB}(\bar{\nu}, T_{atm,1}) \tag{28}
\end{aligned}$$

where $L_{obs}(i, j, \bar{\nu}, T_{atm,1}, T_{atm,2}, T_{back}, T_{plm})$ is the observed spectrum at the pixel indexed by i and j ; ε_{back} is the emissivity of the background; $L_{BB}(\bar{\nu}, T)$ is the planckian blackbody spectral radiance function at temperature, T ; $\tau_{atm,1}(\bar{\nu}, T_{atm,1})$ and $\varepsilon_{atm,1}(\bar{\nu}, T_{atm,1})$ are the atmospheric spectral transmittance and emissivity, respectively, along the path between the background and the plume; $\tau_{atm,2}(\bar{\nu}, T_{atm,2})$ and

$\varepsilon_{atm,2}(\bar{\nu}, T_{atm,2})$ are the atmospheric spectral transmittance and emissivity, respectively, along the path between the plume and the FIRST-MWE; $\tau_{plm,n}(i, j, \bar{\nu}, T_{plm,n})$ and $\varepsilon_{plm,n}(i, j, \bar{\nu}, T_{plm,n})$ are the spectral transmittance and emissivity, respectively, of the n^{th} layer of the plume at each pixel; T_{back} , T_{plm} , and T_{atm} are the temperatures of the background, plume, and atmosphere, respectively. The diagram in Figure 32 gives a visual depiction of the radiative transfer model necessary to replicate the spectrum at each pixel.

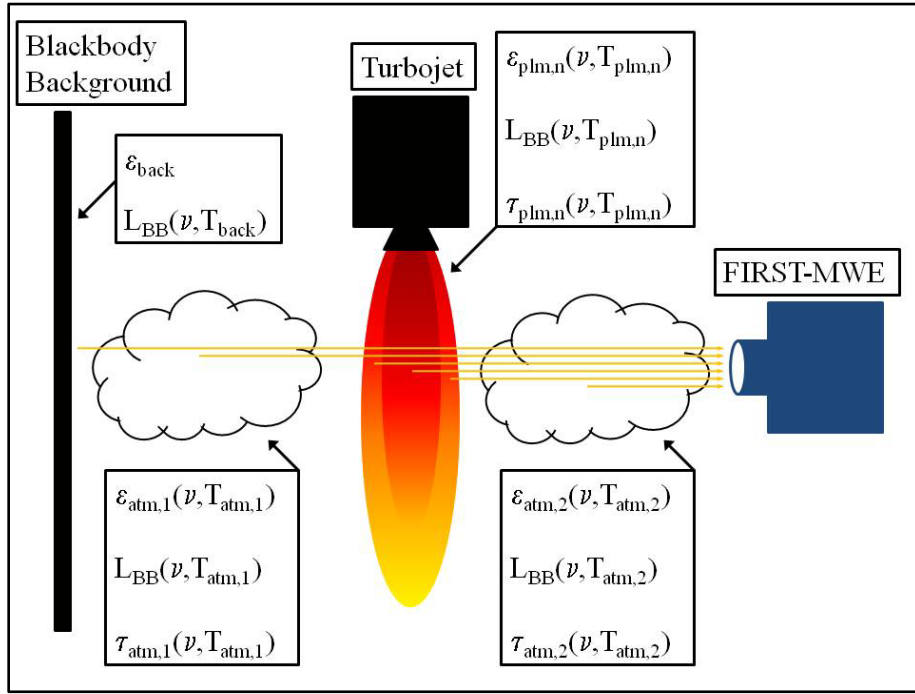


Figure 32. Diagram illustrating the radiative transfer model of the experimental setup.

The model described in Equation (28) was attempted for a single pixel and two plume temperatures, however, it required several minutes of computation time to produce a single iteration. The MATLAB scripts for this process are included in Appendix D.

This model is unsuitable for least squares fitting due to the number of variables required to be fit non-linearly; it is necessary to make simplifying assumptions. As stated previously, in order to build a computationally efficient model, it was necessary to assume that the plume temperature and chemical species concentrations at each pixel could each be represented by a single average value, with the assumption that this represents the average spectrum. This approximation considerably decreased the computation time of the model fit.

Two assumptions regarding the radiance from the background were made. One was to remove the plume transmittance, which would have required nonlinear fitting of the plume chemical species concentrations and temperatures, and the other was to approximate the emissivity as from a blackbody, $\varepsilon_{\text{back}} = 1$. The decision to remove plume transmittance was based on the notion that the plume absorption of the background radiance had a minimal impact on the emission spectrum. Because plume emission is what is being fit, this could be ignored.

Two approximations regarding the atmosphere were made. It was determined that the path between the background and plume, approximately 1.2 m, was sufficiently small compared with the path between the plume and the FIRST-MWE, approximately 11.2 m, to ignore the transmission through and emission from that first path. The emission from the second path was ignored as well, assumed to be of insufficient magnitude to warrant inclusion.

Incorporating all these approximations, the radiometric model, which was used to replicate the spectrum for each pixel, conformed to the radiative transfer equation

$$L_{\text{obs}}(i, j, \bar{\nu}, T_{\text{atm}}, T_{\text{back}}, T_{\text{plm}}) = L_{\text{BB}}(\bar{\nu}, T_{\text{back}})\tau_{\text{atm},2}(\bar{\nu}, T_{\text{atm},2})$$

$$+ \varepsilon_{plm}(i, j, \bar{\nu}, \overline{T_{plm}}) L_{BB}(\bar{\nu}, \overline{T_{plm}}) \tau_{atm,2}(\bar{\nu}, \overline{T_{atm,2}}) \quad (29)$$

where $\overline{T_{plm}}$ and $\overline{T_{atm,2}}$ are the average temperatures of the plume and atmosphere between the plume and FIRST-MWE, respectively.

It is possible to simplify Equation (29) by making further approximations. By assuming the plume and atmosphere are optically thin for the spectral region of interest, 1800 – 3000 cm^{-1} (3.3 – 5.5 μm), the spectral transmittance and emissivity of the plume and atmosphere are given by

$$\tau(i, j, \bar{\nu}, T) = e^{-\sum_{k=1}^K Q_k(i, j) \sigma_k(i, j, \bar{\nu}, T)} \cong 1 - \sum_{k=1}^K Q_k(i, j) \sigma_k(i, j, \bar{\nu}, T) \quad (30)$$

$$\varepsilon(i, j, \bar{\nu}) = 1 - e^{-\sum_{k=1}^K Q_k(i, j) \sigma_k(i, j, \bar{\nu}, T)} \cong \sum_{k=1}^K Q_k(i, j) \sigma_k(i, j, \bar{\nu}, T) \quad (31)$$

where $Q_k(i, j) = N_k(i, j)l(i, j)$ is the k^{th} chemical species concentration multiplied by the pathlength at a pixel indexed by i and j , and $\sigma_k(i, j, \bar{\nu}, T)$ is the effective spectral molecular absorption cross section of the k^{th} chemical species at that pixel. The effective molecular absorption cross section is defined as a combination of the quantum-mechanical dipole overlap matrix and the statistical temperature-dependent distribution of states [36]. The effective spectral molecular cross section for each molecule is retrieved from the HITRAN database, and incorporates the Maxwell-Boltzmann distribution with the dipole overlap matrix, making it temperature dependent. The approximation in transmittance and emissivity is based on a series expansion of the exponential, which is valid for optically thin media. The regime of optically thin media is subjective; however, a good rule of thumb is $\sum_{k=1}^K Q_k(i, j) \sigma_k(i, j, \bar{\nu}) < 0.1$ for all spectral locations. This relation was determined to hold for the turbine engine exhaust plume and atmosphere in question. Equation (29) reduces to

$$\begin{aligned}
L_{obs}(i, j, \bar{\nu}, T_{atm}, T_{back}, T_p) = & \\
\varepsilon_{BB} L_{BB}(\bar{\nu}, T_{back}) \tau_{atm}(\bar{\nu}, T_{atm}) & \\
+ [\sum_{k=1}^K Q_k(i, j) \sigma_k(i, j, \bar{\nu}, T_p)] L_{BB}(\bar{\nu}, T_p) \tau_{atm}(\bar{\nu}, T_{atm}) & \quad (32)
\end{aligned}$$

In the spectral region of interest, the only molecules in the plume that emit enough to show in the spectra are H₂O, CO₂, and CO. Thus, the relation reduces further;

$$\begin{aligned}
L_{obs}(i, j, \bar{\nu}, T_{atm}, T_{back}, T_{plm}) = & L_{BB}(\bar{\nu}, T_{back}) \tau_{atm,2}(\bar{\nu}, T_{atm,2}) \\
+ L_{BB}(\bar{\nu}, T_{plm}) \tau_{atm,2}(\bar{\nu}, T_{atm,2}) Q_{H_2O}(i, j) \sigma_{H_2O}(i, j, \bar{\nu}, T_{plm}) & \\
+ L_{BB}(\bar{\nu}, T_{plm}) \tau_{atm,2}(\bar{\nu}, T_{atm,2}) Q_{CO_2}(i, j) \sigma_{CO_2}(i, j, \bar{\nu}, T_{plm}) & \\
+ L_{BB}(\bar{\nu}, T_{plm}) \tau_{atm,2}(\bar{\nu}, T_{atm,2}) Q_{CO}(i, j, \bar{\nu}) \sigma_{CO}(i, j, \bar{\nu}, T_{plm}) & \quad (33)
\end{aligned}$$

where the only known parameter is $L_{obs}(i, j, \bar{\nu}, T_{atm}, T_{back}, T_{plm})$, the spectral radiance observed by the sensor. However, the temperature-dependent shape of $\sigma_{H_2O}(i, j, \bar{\nu}, T_{plm})$, $\sigma_{CO_2}(i, j, \bar{\nu}, T_{plm})$, $\sigma_{CO}(i, j, \bar{\nu}, T_{plm})$, $L_{BB}(\bar{\nu}, T_{plm})$, and $L_{BB}(\bar{\nu}, T_{back})$ are known; the unknown parameter in each is the temperature, which is the same for the four plume effective cross sections, and the background temperature is the same for all pixels. The concentration pathlengths of H₂O, CO₂, and CO, the atmospheric chemical species concentrations, and the distribution of temperatures within the plume are unknown parameters.

Additionally, a spectral axis multiplier was included to account for the different pathlengths the HeNe laser travels to each pixel. Recall that the HeNe laser is used as the trigger for the collection of an interferogram point. The path the HeNe laser travels is further for points on the FPA away from the optical axis than for the pixel on the optical axis. The path difference results in a multiplicative factor for the spectral axis for the

pixels away from the optical axis, the magnitude depending on the distance from the optical axis. Only a small correction is necessary to account for this difference, with values ranging from 0.9995 to 1.0005 across the entire FPA.

One final approximation was incorporated. The planckian blackbody functions of the background and any additional instrument self-emission were each replaced with a third order polynomial. The planckian is smoothly varying, and is represented well by a third order polynomial. The polynomial representing the background was multiplied by the atmospheric transmittance, while the polynomial representing the instrument self-emission was not. This was done in order to enable linear fitting of the coefficients instead of nonlinear fitting of the temperatures. The final form of the radiative transfer equation used for spectral fitting is given by

$$L_{obs}(i, j, \xi, T_{atm}, T_{plm}) = \tau_{atm,2}(\xi, T_{atm,2}) \left[L_{BB}(\xi, T_{plm}) \left(Q_{H_2O}(i, j) \sigma_{H_2O}(i, j, \xi, T_{plm}) + Q_{CO_2}(i, j) \sigma_{CO_2}(i, j, \xi, T_{plm}) + Q_{CO}(i, j, \bar{\nu}) \sigma_{CO}(i, j, \xi, T_{plm}) \right) + A_0(i, j) + A_1(i, j) \xi + A_2(i, j) \xi^2 \right] + B_0(i, j) + B_1(i, j) \xi + B_2(i, j) \xi^2 \quad (34)$$

where A_0 through A_2 and B_0 through B_2 , the polynomial coefficients, and Q_{H_2O} , Q_{CO_2} , and Q_{CO} , the molecular concentration pathlengths, are the linear fit parameters; $\xi = C\bar{\nu}$, the spectral axis multiplicative factor, the atmospheric concentrations of H_2O , CO_2 , and CO , which impact the atmospheric transmittance, and T_{plm} are nonlinear fit parameters.

Spectral Model Fitting.

To determine the unknown values of the fit parameters, both linear and non-linear fitting algorithms were employed in order to fit the model to the observed spectra.

Because of the many assumptions made in the production of the radiometric model used

for fitting, the potential that the model does not exactly replicate the data is high; in the case that the model does not exactly replicate the data, the model will not exactly match the spectrum, and the model must properly balance where to make the model fit the data. Because the goodness-of-fit measure was the minimization of squared error, it was necessary to weight the error in the spectra to account for a bias that occurred due to the large CO₂ emission compared to the relatively small CO and H₂O emission features. Without proper weighting, reduction of the CO₂ error would take precedence; large errors in the fit of spectral emission features of CO and H₂O would be permitted in order to reduce the error in the CO₂ emission region. To create a proper weighting, the spectrum of each pixel was integrated by region, 1800 – 2150 cm⁻¹ (4.65 – 5.56 μm) for H₂O, 2150 – 2250 cm⁻¹ (4.44 – 4.65 μm) for CO, and 2250 – 2400 cm⁻¹ (4.17 – 4.44 μm) for CO₂. The largest value of the three integrated regions was divided by the number of spectral bins in each region. This number became the weighting factor for each region of the spectrum to be used in the fitting algorithm.

Before finding the plume temperature and chemical species concentration pathlengths for each pixel, the atmospheric concentrations of H₂O, CO₂ and CO were determined using a subset of pixels. Due to the short distance between the FIRST-MWE and turbine engine, as well as the physical layout of the test setup, excessive amounts of H₂O, CO₂, and CO were able to build along the path between the two during the experimental campaign. This fact was only realized after the campaign was concluded, and it became important to find accurate values for the elevated concentrations of these chemical species along the path to properly account for atmospheric absorption of the hot plume emissions. To find the atmospheric chemical species concentrations accurately,

but with minimal time, a computationally demanding recursive fit routine was implemented using representative pixels selected from across the FPA. Figure 33 shows an image of the selected representative pixels. The model fitting algorithm had two recursive loops, with three fitting routines, as illustrated with a flow chart in Figure 34.

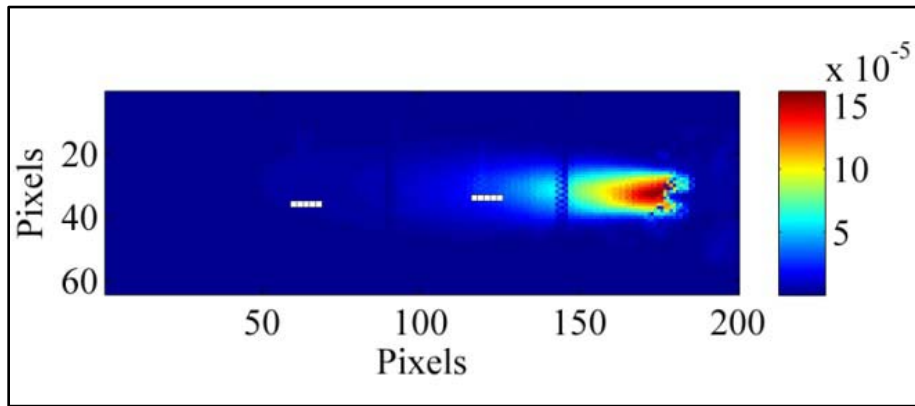


Figure 33. The seventeen pixels selected to represent the scene for determination of the atmospheric constituents. The color scale is in units of $W/cm^2 \cdot Sr \cdot cm^{-1}$.

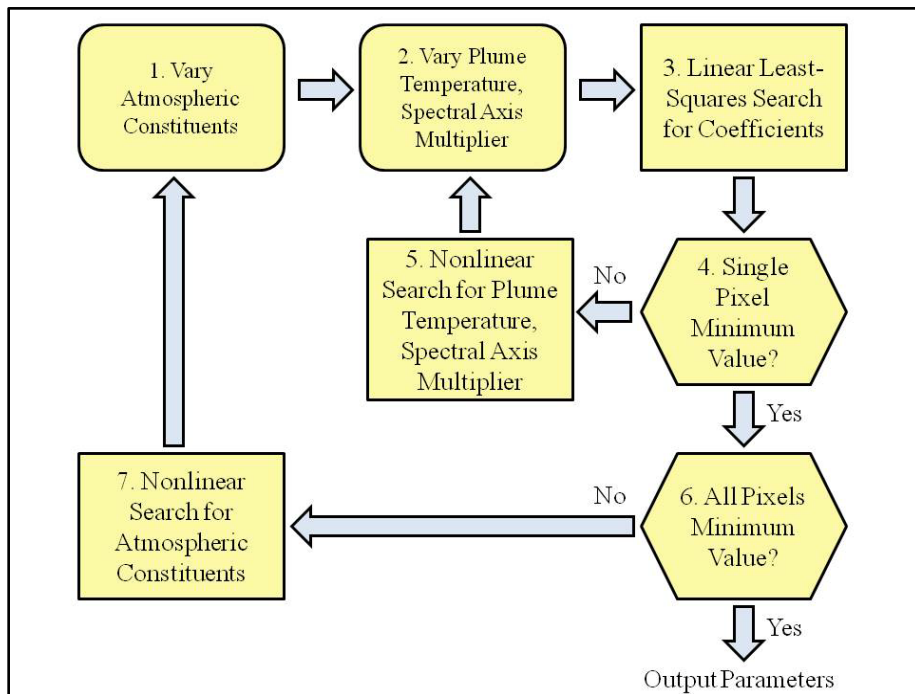


Figure 34. Flow chart illustrating the model fitting algorithm. Two loops, containing three least squares search routines, were used to determine the atmospheric constituents at representative pixels.

The outer loop contained a nonlinear least squares algorithm that varied parameters which had, approximately, no pixel-to-pixel variation. The parameters varied here were the atmospheric concentrations of CO₂, H₂O, and CO along the path between the FIRST-MWE and the scene. The model was input with initial estimates for these atmospheric concentrations to allow progression to the inner loop. These initial estimates were the approximate atmospheric levels, 388, 7425, and 177 parts per million by volume (ppmv) for CO₂, H₂O, and CO, respectively [12].

The inner loop contained the two other least squares fitting routines, which varied parameters that changed for each pixel. The parameters fit with a nonlinear least squares algorithm were plume temperature and spectral axis multiplier. Initial estimates of 310 K for the plume and unity for the multiplier were input in order to progress to the third fitting routine.

The last fitting algorithm dealt only with parameters which could be fit using a linear least squares approach. Chemical species concentration pathlengths were fit at this level. As mentioned previously, in order to save time and computing resources, the planckian blackbody function representing the background was approximated as a cubic polynomial in order to enable linear fitting in the lowest level as well. This reduced the computational complexity; otherwise the background had to be fit nonlinearly.

Once the initial estimates for the parameters in the first and second fitting routines were used to determine the linear coefficients, the plume temperature and spectral axis multiplier parameters were varied using a direct search algorithm in order to minimize the sum of squared error between the model and the calibrated data. Once the parameter values were found that minimized the sum of square errors in the inner loop for each

individual pixel, the outer loop parameters were varied and the whole process started over again. These loops were continued until values were found for all parameters which minimized the summed error of all representative pixels.

The atmospheric concentrations of CO₂, H₂O, and CO absorbing along the path between the turbine engine exhaust plume and sensor, as found by minimizing the sum of squared error, were 800 ppmv, 1624 ppmv, and 402 ppmv, respectively. With normal values in the range of 388 ppmv, 6300 ppmv, and 177 ppmv, respectively, the values found through fitting are elevated over normal atmospheric concentrations for CO₂ and CO, which was expected given the previously described experimental setup, which allowed a build-up of plume emissions along the path between the FIRST-MWE and turbine. The value is low for H₂O, which was difficult for the model to fit due to the small magnitude of the H₂O spectral features.

This recursive algorithm was implemented on a subset of pixels in order to make the problem of identifying atmospheric parameters tractable. Once these parameters were found, an iterative process was applied which utilized only the inner loop from the previous algorithm. The plume temperature, spectral axis multiplier, and chemical species concentrations were found for all pixels by fitting the model to the calibrated data with the least amount of squared error. This process was completed for each pixel, and required approximately 18 hours of computation time. The values for plume temperature and chemical species concentration pathlengths were used to build spatial distributions of plume temperature and chemical species concentration pathlength. Figures 35-37 show sample pixels of the model fit to the spectrum at different locations throughout the scene.

Due to the low resolution of the entire spectral range, Figures 35-37 show close-up views of the CO and CO₂ spectral emission regions for selected pixels.

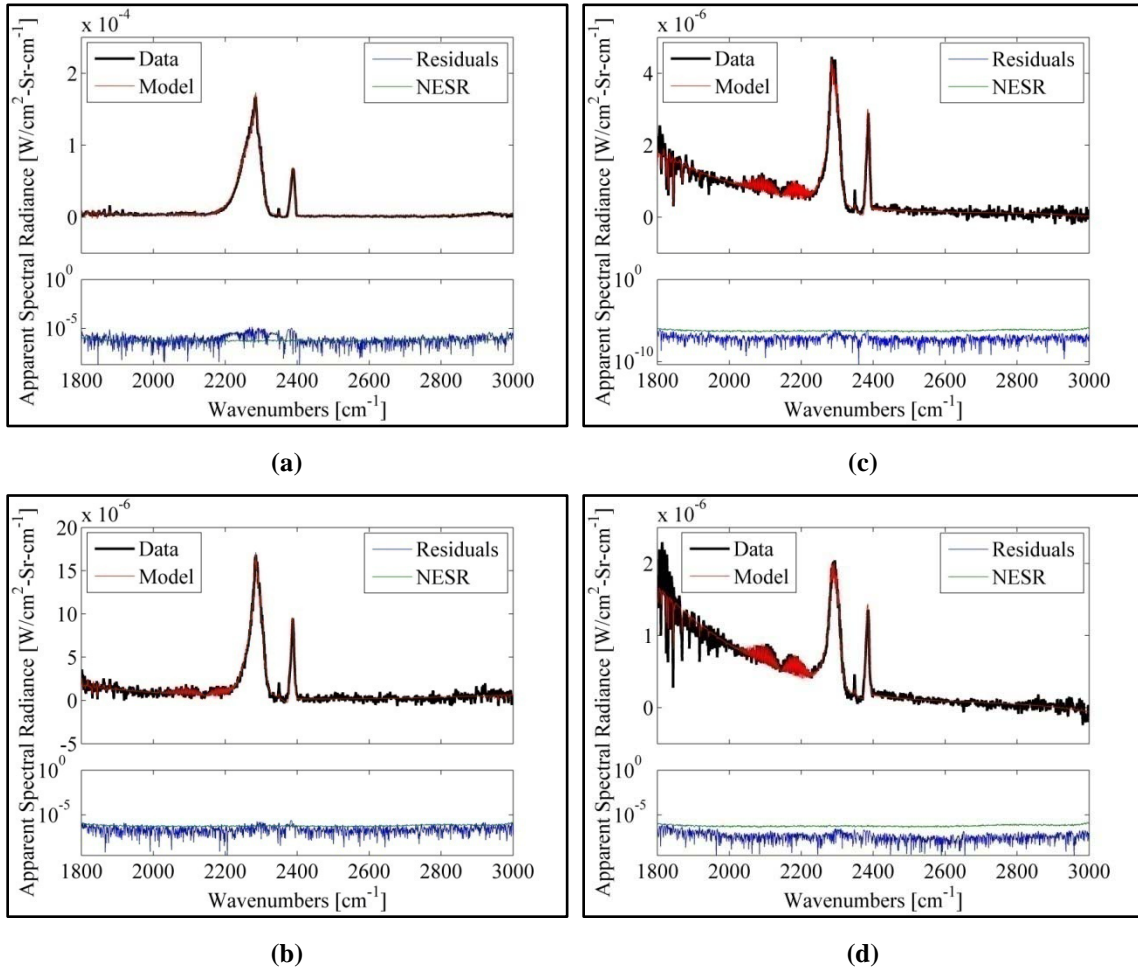


Figure 35. The model (red) fit to the spectrum (black) with residuals (blue) and NESR (green) at pixel (170, 31) (a), pixel (100, 31) (b), pixel (60, 31) (c), and pixel (24, 31) (d). All are with diesel fuel at a 225 cm³/min flow rate.

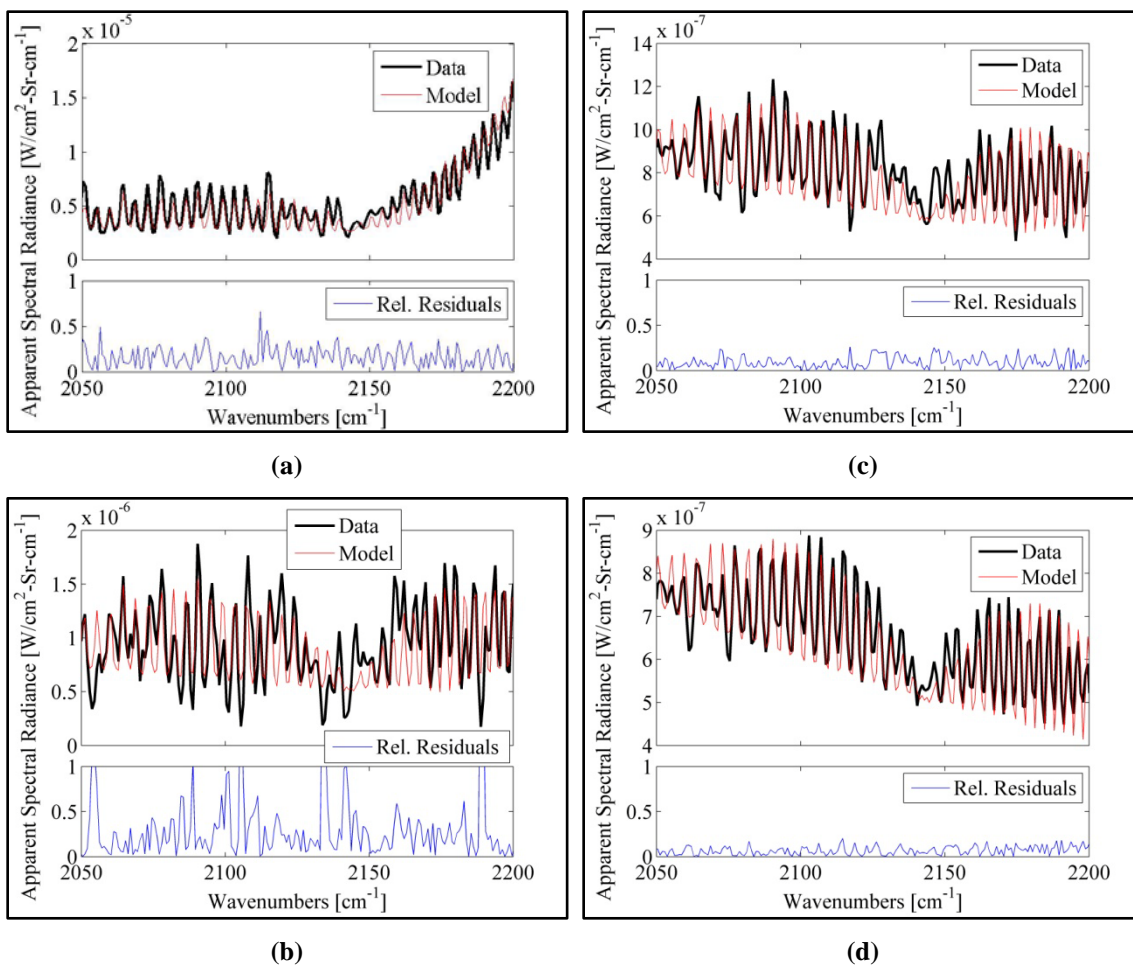


Figure 36. The model (red) fit to the CO emission spectrum (black) with relative residuals (blue) at pixel (170, 31) (a), pixel (100, 31) (b), pixel (60, 31) (c), and pixel (24, 31) (d). All are with diesel fuel at a $225 \text{ cm}^3/\text{min}$ flow rate.

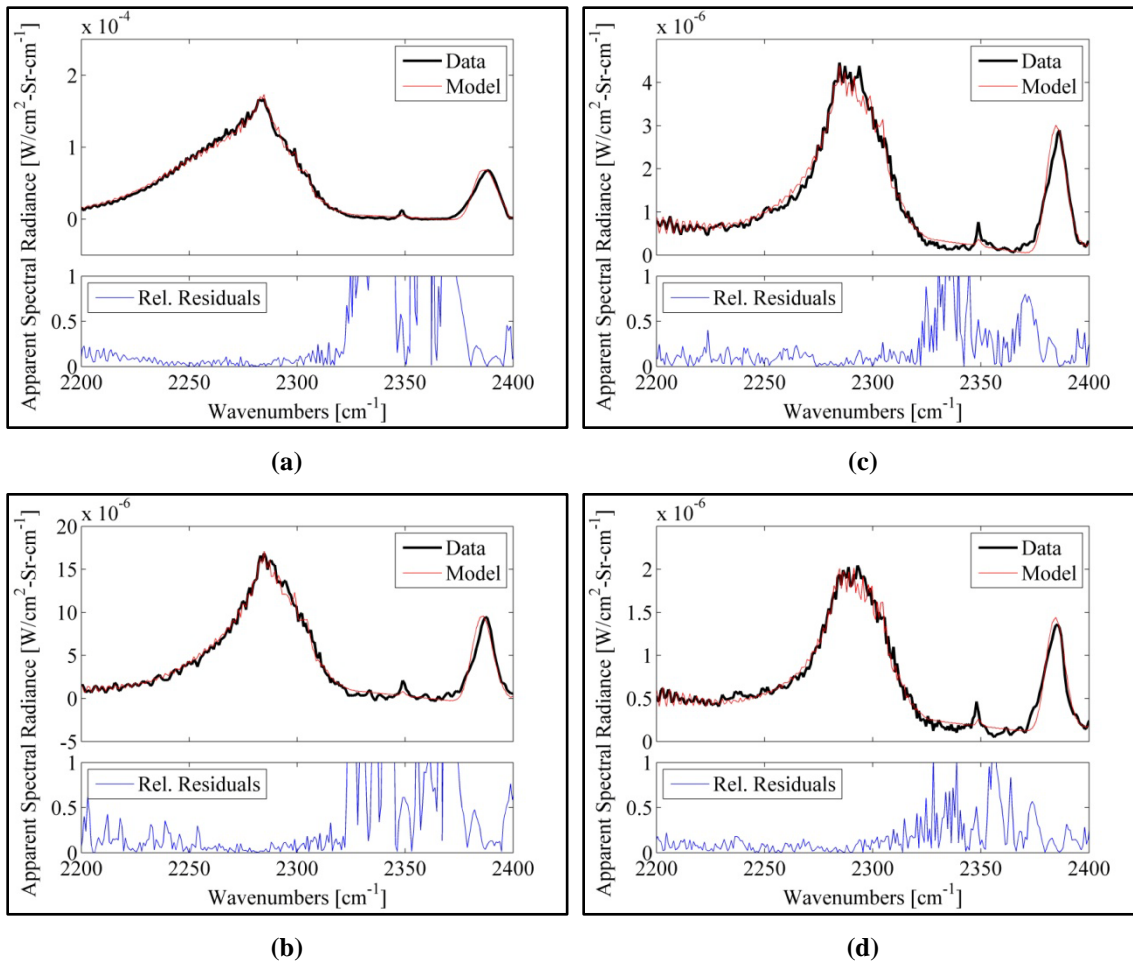


Figure 37. The model (red) fit to the CO₂ emission spectrum (black) with relative residuals (blue) at pixel (170, 31) (a), pixel (100, 31) (b), pixel (60, 31) (c), and pixel (24, 31) (d). All are with diesel fuel at a 225 cm³/min flow rate.

Summary

The error analysis equations necessary to produce uncertainty bounds on the calibrated spectrum, as well as the radiative transfer equations governing the model, were developed. Error analysis provides one way to judge the quality of the calibration process, indicating how much uncertainty is added to the spectra when calibration is performed. Additionally, the error analysis provides insight into the greatest causes of uncertainty. The radiative transfer equations used to build the model were developed as a

way to fully explain the parameters involved in the spectral fitting, and to motivate an explanation of the spectral fitting process.

The uncertainty bounds produced from the error analysis are presented with the calibrated apparent radiance results in the following chapter. The temperature and chemical species concentration spatial distributions extracted from the hyperspectral datacubes via the radiative transfer model are also presented. These results combine to showcase the ability of the FIRST-MWE to remotely collect high quality hyperspectral datacubes, and how even a simple model applied to the data can produce valuable information about a turbine engine exhaust plume.

VI. Results and Analysis

Spatial distributions of total apparent radiance, plume temperature, and plume chemical species concentration pathlengths, as well as apparent spectral radiance at select pixels, are presented for two fuel types and two engine settings. These results exhibit the capability of the FIRST-MWE to collect high quality hyperspectral datacubes, calibrate with small relative uncertainty, and fit a simple radiative transfer model in order to remotely collect information on a turbine engine exhaust plume.

The spatial distributions are oriented in the same manner as the image of the test setup, taken by the bore-sighted visible camera of the FIRST-MWE, as seen in Figure 38; the engine is on the right edge of the scene with the exhaust pointing to the left, through the thermocouple rake. The red outline gives the approximate field of view (FOV) of the MWIR detector on the FIRST-MWE.

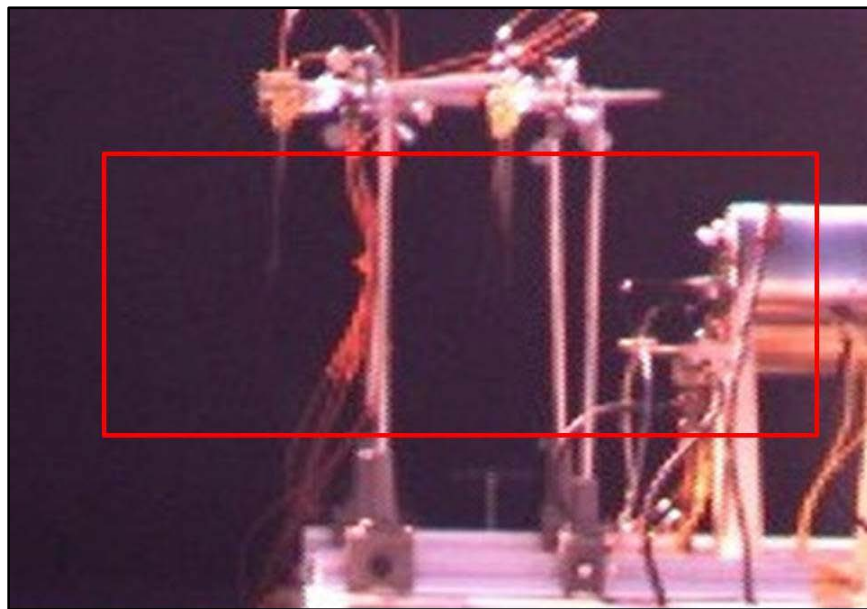


Figure 38. Visible image of the test setup as taken by the FIRST-MWE bore-sighted camera. The engine is on the right edge of the screen with the exhaust pointing to the left, through the thermocouple rake. The red outline gives the approximate FOV of the MWIR detector on the FIRST-MWE.

The spectral radiance of each pixel was obtained by performing the processes of hyperspectral datacube averaging, non-uniformity correction computation and application, and spectral gain and offset computation and application; all have been discussed previously. The plume temperature and chemical species concentration pathlength distributions were obtained by finding a single plume temperature and chemical species concentration pathlength for each of the three chemical species of interest which best fit the model to the spectral data.

The apparent spectral radiance plots show the uncertainty in the result, which is due to the SCAs in the turbine engine exhaust scene, as well as the variation in the blackbody files used for computing the NUC and spectral gain and offset.

Apparent Radiance

The apparent radiance distributions from the turbine engine exhaust plume are shown in two forms, the spatial distribution of total apparent radiance and the apparent spectral radiance at example pixels. Figure 39 shows a visible image from the bore-sighted camera on the FIRST-MWE, showing the approximate FOV of the FIRST-MWE. Figure 40 shows the spatial distribution of total apparent radiance across the FPA for the diesel and kerosene fuels, with fuel flow rates of 300 and 225 cm³/min.

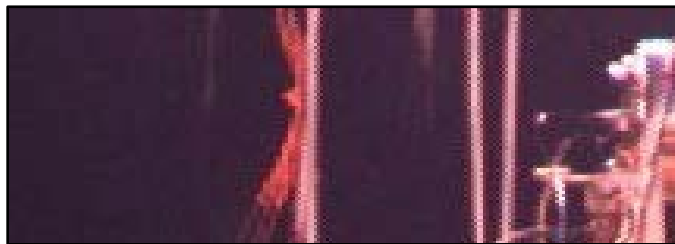
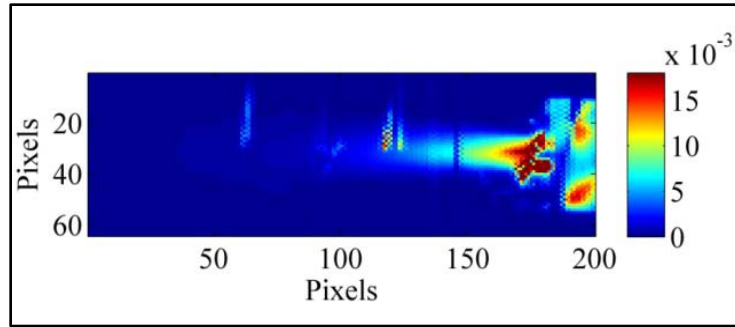
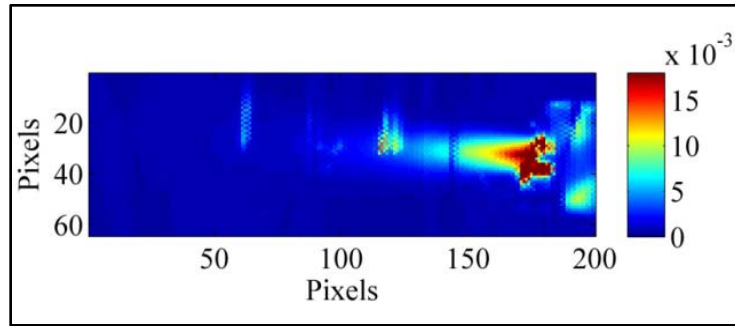


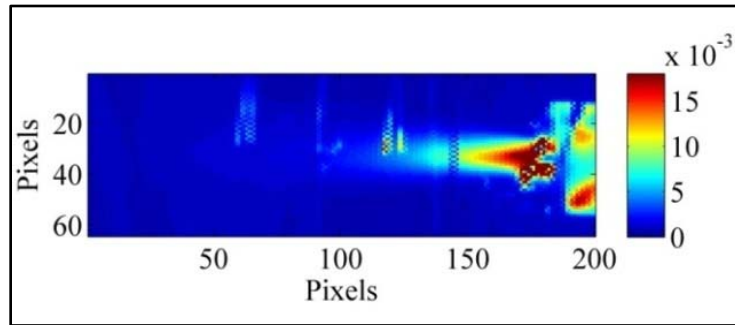
Figure 39. A visible image taken from the bore-sighted camera on the FIRST-MWE, showing the approximate FOV of the MWIR detector.



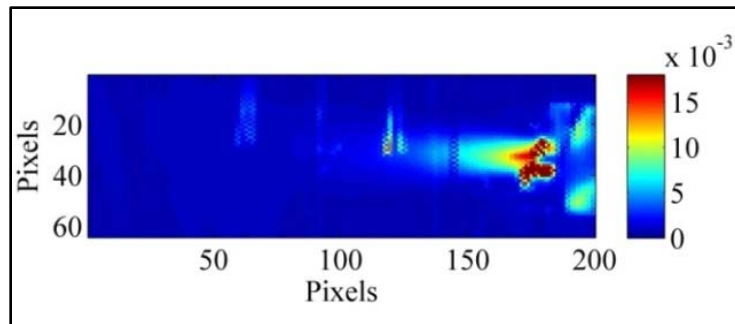
(a)



(b)



(c)



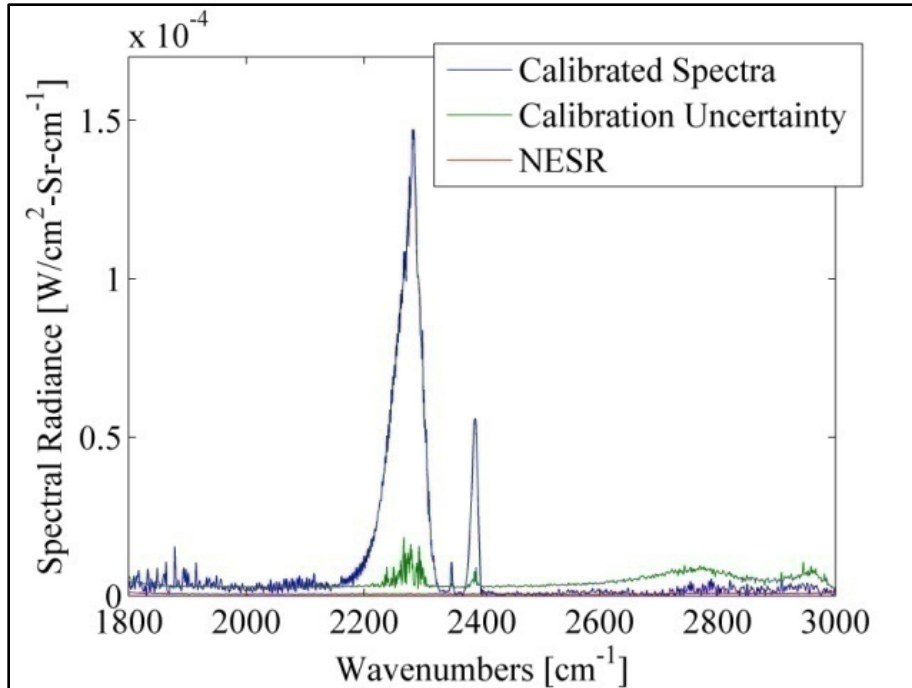
(d)

Figure 40. Total apparent radiance distribution, diesel Fuel at a 300 cm³/min flow rate (a) and 225 cm³/min flow rate (b), kerosene Fuel at a 300 cm³/min flow rate (c) and 225 cm³/min flow rate (d). The color scale is in units of W/cm²-Sr-cm⁻¹.

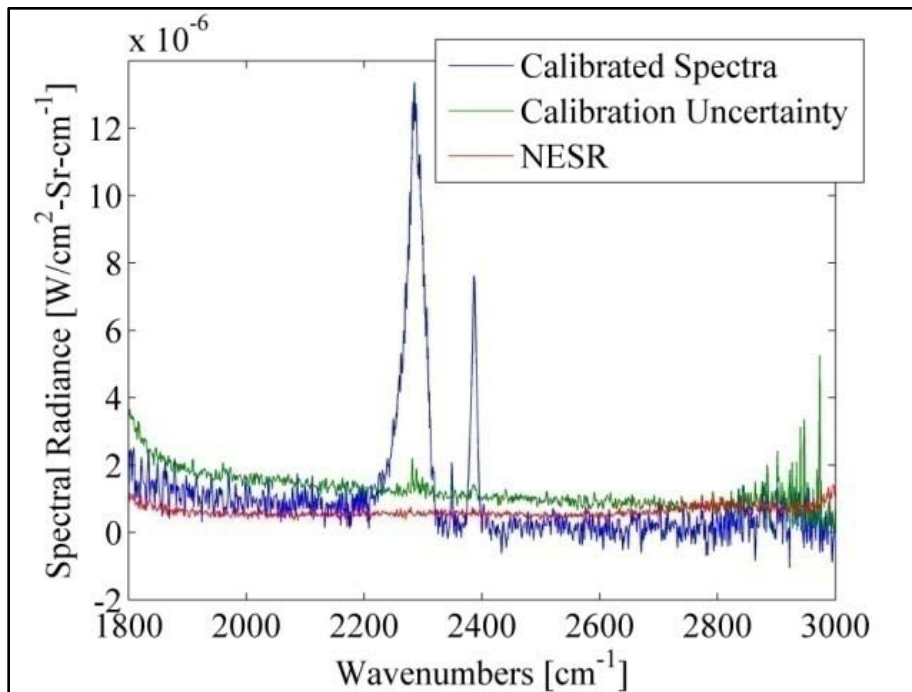
The total apparent radiance distribution provides a time-averaged view of the plume. Due to the hyperspectral datacube averaging performed, each spatial distribution represents the mean total apparent radiance over the entire set of datacube collections, between 15 and 17 minutes. Although each fuel type and flow rate produces different values on a per-pixel basis, the spatial extent and gradient of the plume is consistent. This speaks to the accuracy of the data processing methods.

The apparent spectral radiance of the averaged spectra of several pixels is shown in Figures 41 and 42 for the case of the kerosene fuel with $225 \text{ cm}^3/\text{min}$ fuel flow rate, along with the relative uncertainty in the measurement as computed in the error analysis section. The corresponding position of each pixel is shown in Figure 43.

The equations for uncertainty bounds developed in the previous chapter were applied in the computation of the uncertainties found in Figures 41 and 42. The uncertainty is due to the SCAs impacting the SNR of the scene, as well as the uncertainty associated with the blackbody files used for calibration. Using the error analysis equations of Chapter V, a 1% standard deviation in the raw average blackbody hyperspectral datacube results in a standard deviation of 4.4% in the calibrated average blackbody hyperspectral datacube. Thus, future employment of more stable wide-area blackbodies, control over environmental conditions, and other variation-reducing techniques, a minimization of the raw blackbody uncertainty can be produced, which will reduce the uncertainty in the calibrated hyperspectral datacubes of the turbine engine exhaust plume.

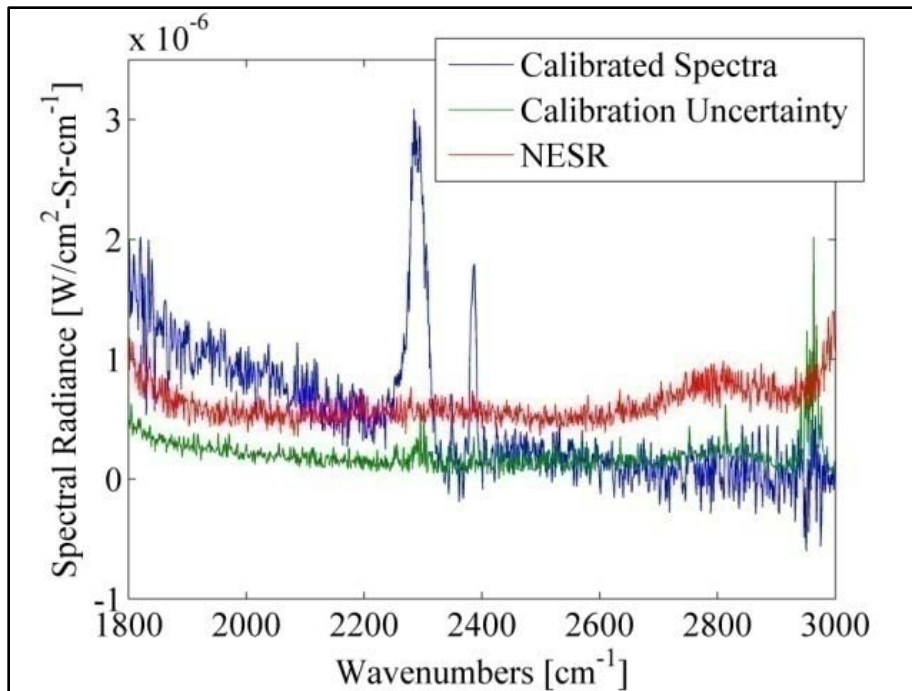


(a)

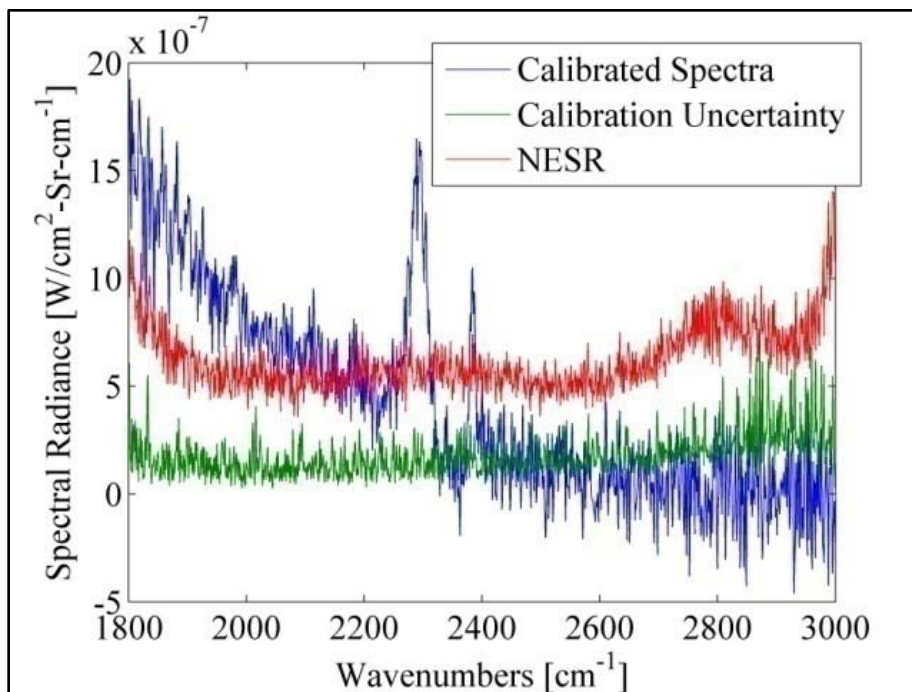


(b)

Figure 41. A calibrated spectrum (blue) with the calibration uncertainty (green) and the FIRST-MWE NESR (red) shown for pixel (170, 31) (a), and pixel (100, 31) (b), with kerosene fuel at a 225 cm³/min flow rate.



(a)



(b)

Figure 42. A calibrated spectrum (blue) with the calibration uncertainty (green) and the FIRST-MWE NESR (red) shown for pixel (60, 31) (a), and pixel (24, 31) (b), with kerosene fuel at a 225 cm³/min flow rate.

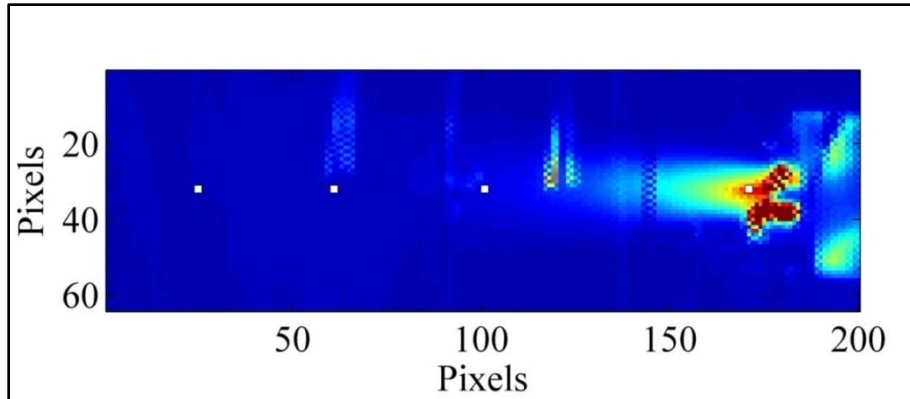
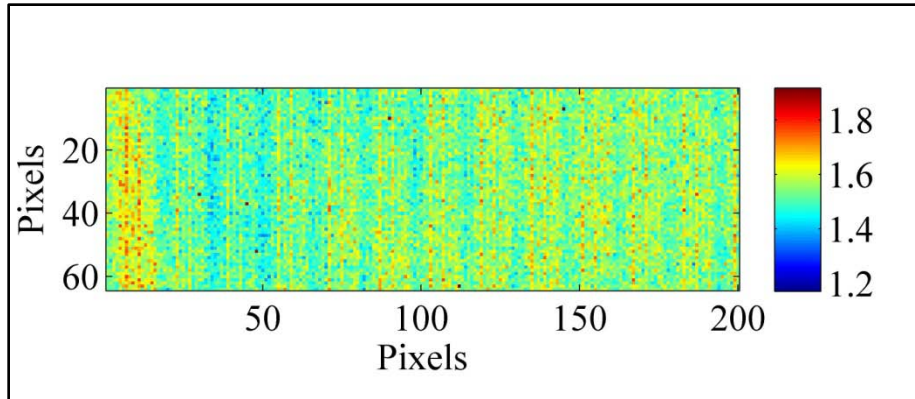


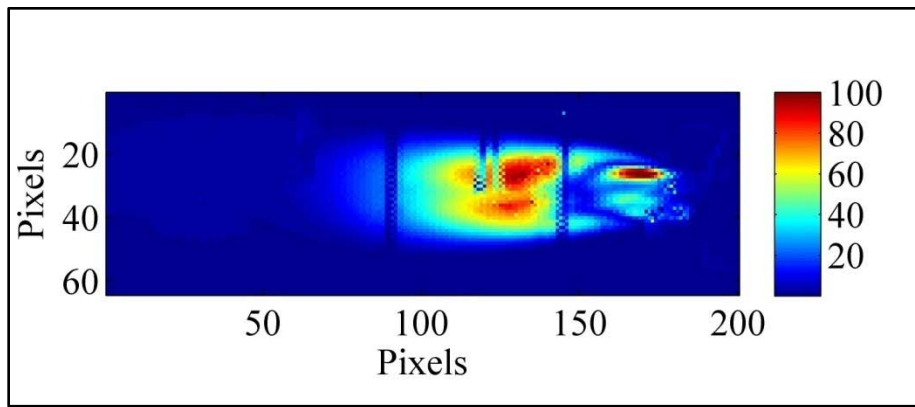
Figure 43. A total apparent radiance distribution showing the pixels selected for showcasing the uncertainty associated with the calibrated data. The white pixels in the image represent the spectra shown in Figures 41 and 42.

The main contributors to the uncertainty in the calibrated spectra were SCAs. Based on the error analysis equations, a 1% standard deviation in the raw average turbine engine exhaust hyperspectral datacube produced an average standard deviation of 1.9% in the calibrated average turbine engine exhaust hyperspectral datacube. Although this resulted in a smaller contribution to calibration uncertainty per raw hyperspectral datacube percent uncertainty than that of the blackbody data, due to SCAs, there is a much larger raw percent uncertainty associated with the turbine engine exhaust than the blackbodies. Figure 44 shows the average relative uncertainty of the blackbody scene and the turbine engine exhaust scene. It is apparent that the uncertainty due to SCAs was much greater than that due to the blackbodies.

Due to SCAs, the variations are not uniformly distributed across the turbine engine exhaust scene. Regions where the plume is varying dramatically from one interferogram point to the next will produce spectra with larger variations. Figure 44 (b) gives a visual representation of the distribution of the standard deviation in the spectra, averaged over the spectral domain.



(a)



(b)

Figure 44. Spatial distribution of the percent standard deviation in the spectra of each pixel, averaged over the spectral dimension for a blackbody (a) and for the turbine engine exhaust scene (b). As expected, the pixels within the plume exhibit more variation than those outside the plume, and much more than the blackbody. The color scales are in percent.

In general, there are two ways to reduce the impact of SCAs on the uncertainty, which is found in the collection of the turbine engine exhaust hyperspectral datacubes. If the time scale of the SCAs was close in magnitude to the required time to collect a hyperspectral datacube, it would be beneficial to explore methods of decreasing the amount of time required to collect the hyperspectral datacubes. In order to decrease the hyperspectral datacube collection time, it is necessary to decrease spectral resolution, spatial resolution or integration time. However, as described in Equation (3), reducing

the time required to collect the hyperspectral datacubes by decreasing the integration time increases the noise by a factor of $\tau_d^{1/2}$, which is counter to the objective. If the application allows for less resolution, it is possible to decrease spectral or spatial resolution without negatively impacting the SNR.

However, for the specific case in question here, the time scale of the turbine engine exhaust plume is too short to completely remove SCAs from the distribution via these methods. Another way to reduce the impact of SCAs, when the variation is approximately normally distributed, is to increase the integration time of each interferogram point collection to an amount long enough to capture the normal distribution within each. By increasing the integration time in this manner, the approximately average value at that interferogram position is obtained, and SCAs are reduced.

In light of the error propagation comparison performed above, reducing the standard deviation in the calibration files has a larger percent impact on the uncertainty in the calibration, however the variations cause by SCAs result in a much larger overall uncertainty in the calibrated spectrum. By maintaining better control of the calibration parameters, such as reducing the variation in blackbody temperature and using temperatures that tightly bound the scene temperature, it is possible to improve the uncertainty calculations. It is also beneficial that the calibration measurements can be performed in the laboratory as opposed to the field, ensuring ample time for multiple collections. The most beneficial method of reducing the uncertainty in the calibrated spectrum is to reduce the presence of SCAs via the methods described previously.

In addition to the uncertainty calculated in the error analysis section, another method of gauging the quality of a calibrated spectrum is the comparison of the signal level to the Noise Equivalent Spectral Radiance (NESR), as described in Equation (3) and presented in Chapter IV. Whether the calibrated spectrum is on the same order of magnitude as the NESR or ten orders of magnitude greater, this comparison gives insight into the quality of the data. Refer to Figure 16 to see the NESR of the FIRST-MWE.

The NESR of the FIRST-MWE was compared against the spatial distribution of total apparent radiance in order to provide insight into the regions where model fitting should provide accurate results. For spectra that are on the same order of magnitude as the NESR, the model will be fitting to noise. In these regions, the SNR is simply not high enough to produce reliable results, due to either low temperatures, small concentrations of emitting chemicals, or a combination of the two. Figure 45 shows the spatial distribution of the SNR of the total apparent radiance for the entire 200x64 pixel array collected in the experimental campaign.

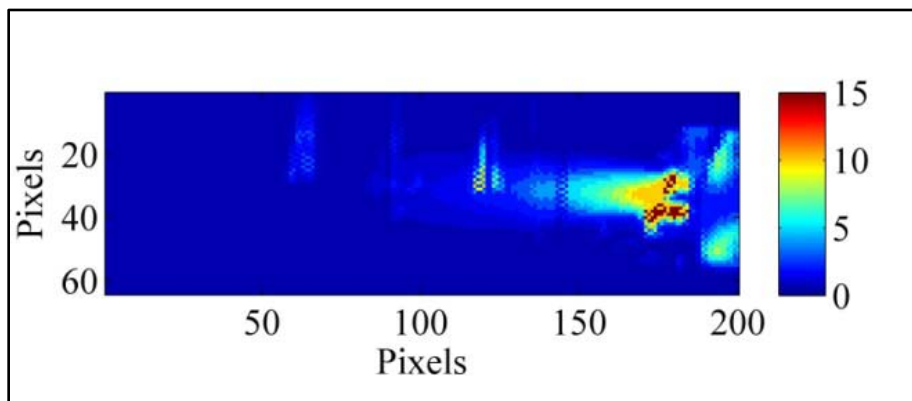


Figure 45. The spatial distribution of SNR. This was computed by taking the average NESR compared with the average signal at each pixel.

There are many pixels in the scene where the SNR is large, mainly concentrated in the regions immediately in the path of the turbine engine exhaust plume. For these pixels, it is reasonable to expect the model to determine sensible values for plume temperature and chemical species concentration pathlengths. Figure 46 gives an example of the calibrated spectrum compared to the NESR of FIRST-MWE.

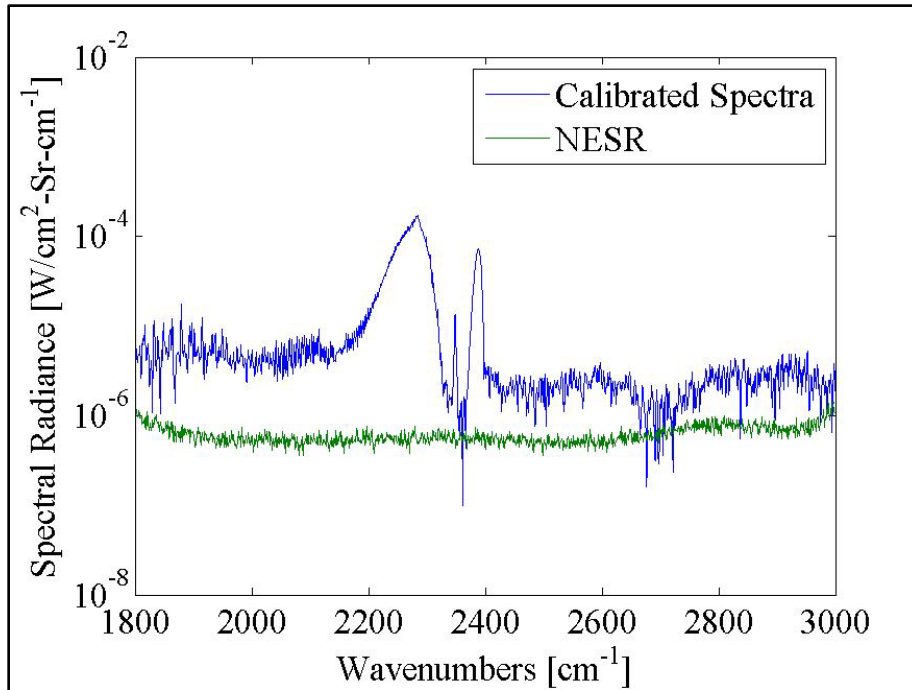


Figure 46. Calibrated spectrum of pixel (170, 32), from the kerosene fuel at a 225 cm³/min flow rate, and the NESR of the FIRST-MWE.

There are also many pixels in the scene where the SNR is very close to unity, if not less. Figure 47 gives an example of the calibrated spectrum of the same magnitude as the NESR of the FIRST-MWE. For the regions of the scene where the SNR is near or below unity, it is unreasonable to expect proper temperature and chemical species concentration pathlength results. For that reason, regions where the SNR is low have

been omitted from further analysis. The temperature and concentration pathlength distributions are presented in the subsequent sections.

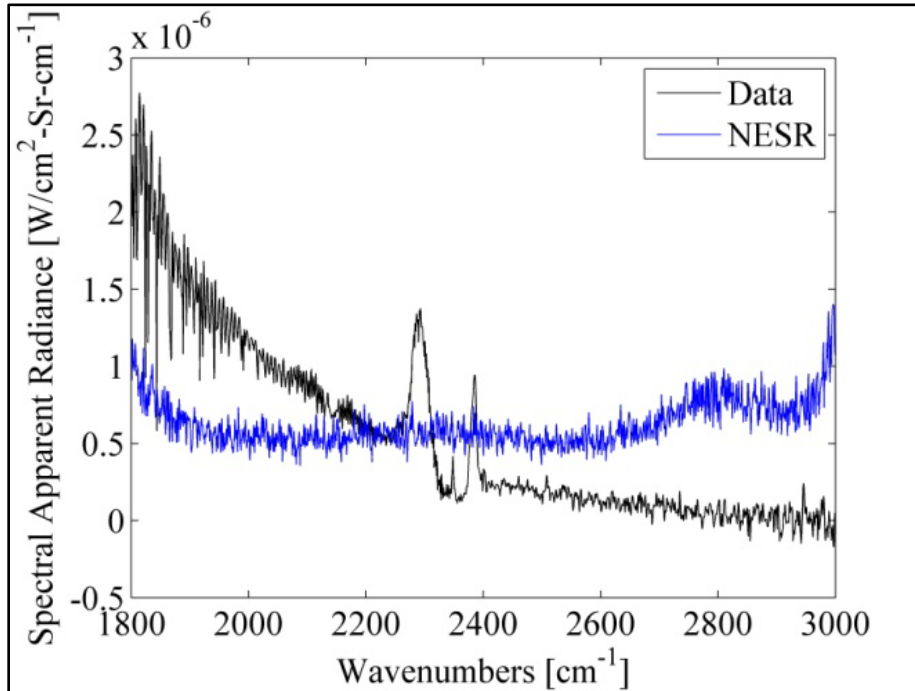


Figure 47. Calibrated spectrum of pixel (15, 30), from the kerosene fuel at a 225 cm³/min flow rate and the NESR of the FIRST-MWE.

Temperature Spatial Distributions

The temperature spatial distributions from the turbine engine exhaust plume are presented in Figure 48 for all four fuel type and flow rate combinations. The spatial distributions of temperature for the four fuel type and flow rate combinations are compared against one another to highlight the similarities and differences between the spatial distributions. The fuel flow rate has a large impact on the distribution of temperatures, while the fuel type does not. Additionally, the temperatures of specific pixels are compared against the *in situ* measurements taken by the thermocouples. These measurements were in agreement to within approximately 212 K, with much of the

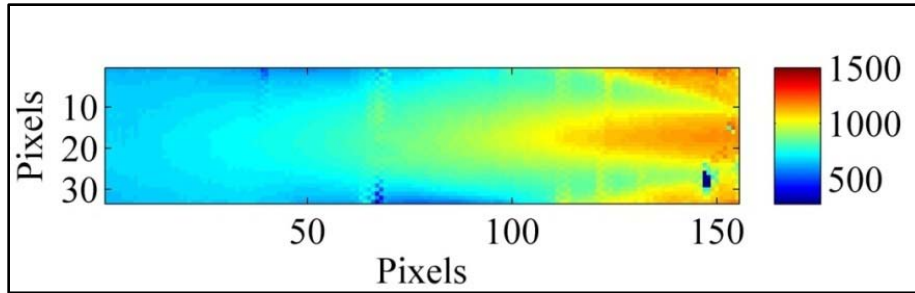
difference attributed to the approximations required to obtain a computationally efficient expression for the radiative transfer model.

Distribution Comparisons.

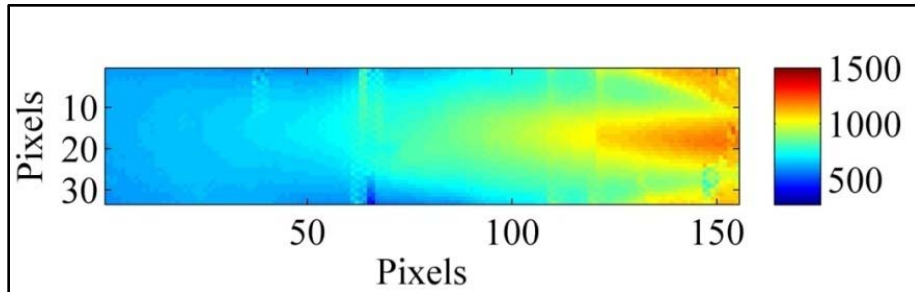
The temperature spatial distributions exhibit expected trends. For both fuel types, the temperature distribution produced by the model fitting the 300 cm³/min flow rate hyperspectral datacubes produced a greater spatial extent compared to the temperature distribution produced by the model fitting the 225 cm³/min flow rate hyperspectral datacubes. For pixels further from the turbine engine exhaust exit plane, it is possible to visually detect a negative temperature gradient of larger magnitude in the temperature distribution produced from the 225 cm³/min flow rate data compared with that produced with the 300 cm³/min flow rate data. The 225cm³/min flow rate appears to mix with the ambient atmosphere closer to the turbine engine exhaust exit plane.

By comparing temperature distributions through ratios, it is possible to highlight the similarities and differences found between the four fuel type and fuel flow rate combinations. Figure 49 enables visualization of the differences found between the two fuel flow rates used in the experiment. It is possible to discern that the higher fuel flow rate produced an increased temperature and greater spatial extent of the exhaust plume for both fuel types.

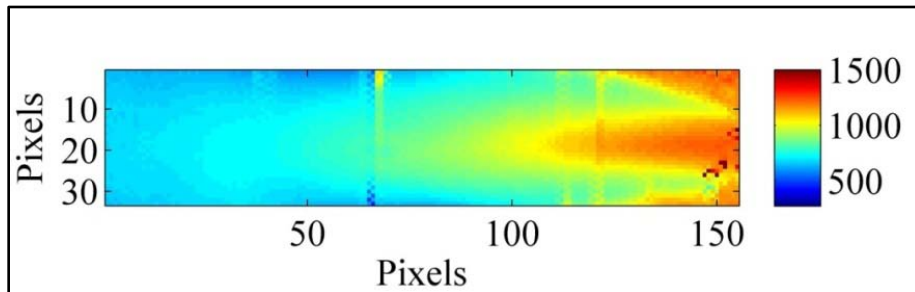
The ratio of temperature distributions of differing fuel type highlights the similarities between the diesel and kerosene fuels. Figure 50 shows the ratio of the temperature distribution of diesel fuel to kerosene fuel for fuel flow rate settings 300 cm³/min and 225 cm³/min. It is evident that the change in flow rate has a greater impact on the temperature than the fuel type.



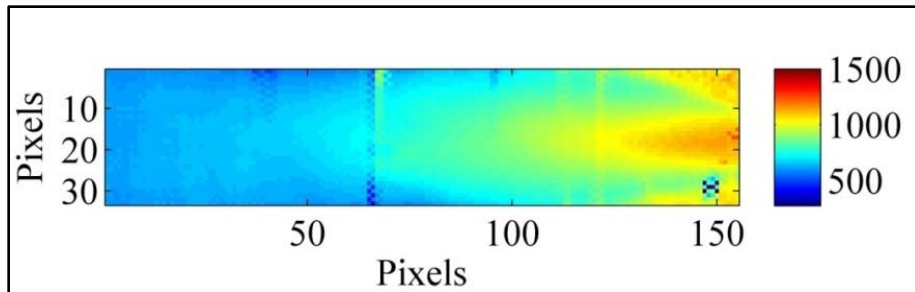
(a)



(b)

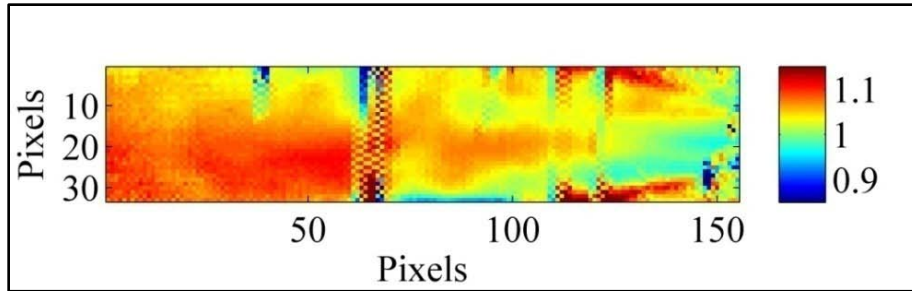


(c)

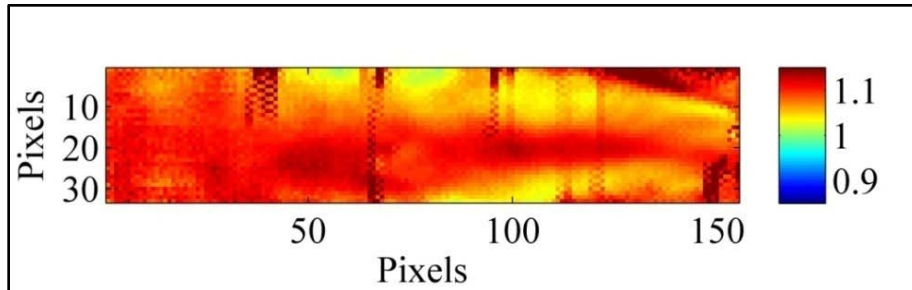


(d)

Figure 48. Spatial distribution of temperatures determined by the model for diesel fuel at a 300 cm^3/min flow rate (a), diesel fuel at a 225 cm^3/min flow rate (b), kerosene fuel at a 300 cm^3/min flow rate (c), and kerosene fuel at a 225 cm^3/min flow rate (d). The color scale is in Kelvin.

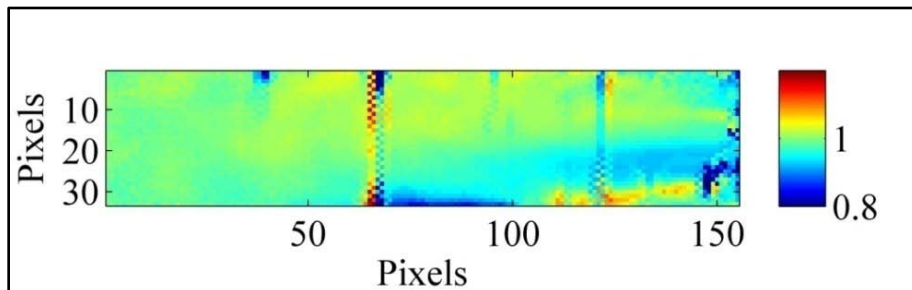


(a)

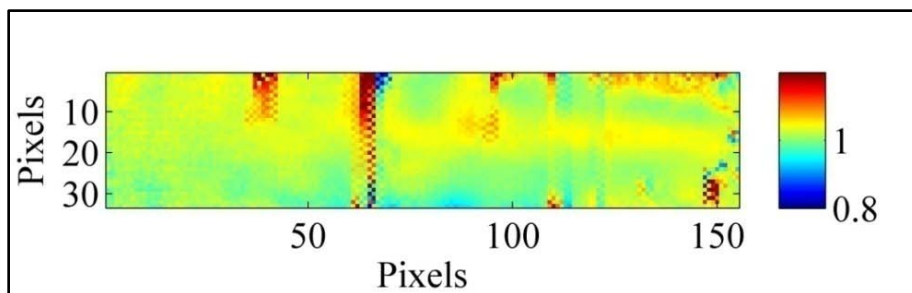


(b)

Figure 49. A distribution showing the ratio of the temperature distributions of the two fuel flow rates, $300 \text{ cm}^3/\text{min}$ to $225 \text{ cm}^3/\text{min}$, for diesel (a) and kerosene (b). The ratio highlights the fact that the $300 \text{ cm}^3/\text{min}$ flow rate produces higher temperatures for both fuel types.



(a)



(b)

Figure 50. A distribution showing the ratio of the temperature distributions of the two fuel types, diesel to kerosene, for $300 \text{ cm}^3/\text{min}$ (a), and $225 \text{ cm}^3/\text{min}$ (b). The ratio highlights the similarities between the temperature distributions produced by the two fuel types.

In Situ Comparisons.

In addition to comparisons between fuel types and flow rates, it is possible to use the temperatures of the *in situ* thermocouple to gauge the quality of the model fit to the data. In order to accomplish this comparison, two regions of pixels have been selected. Because a full path through the plume is not visible through the thermocouples, it is not possible to determine temperatures at the pixels occupied by the thermocouples. To achieve a temperature similar to that which would be at the thermocouple location, the temperatures of the pixels identified in Figure 51 have been averaged to determine the approximate temperature at the thermocouples. They are the same distance away from the exhaust exit plane, and only a few pixels below the thermocouple locations.

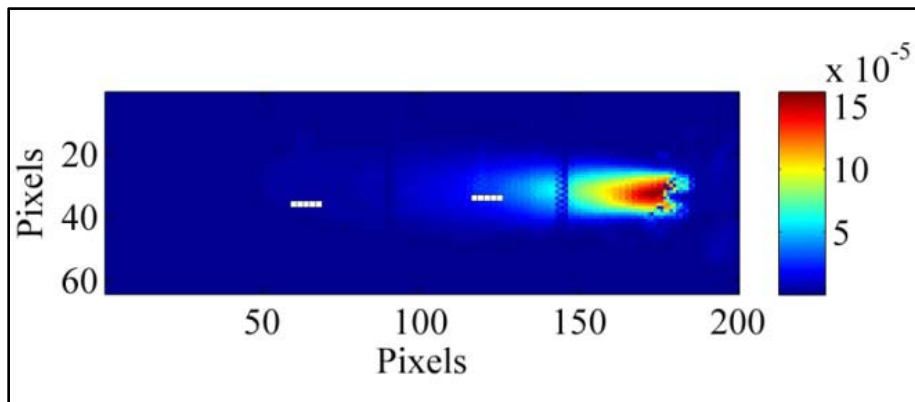


Figure 51. Pixels used to identify the model determined temperature equivalent to the temperatures measured by the thermocouples. The pixels in each region were averaged together to provide a single temperature for comparison.

The average temperature for both regions was computed for each fuel type and flow rate combination. Table 2 lists the average static temperatures associated with two regions of the scene corresponding to the two thermocouple locations, and the percentage difference between the two. Region one corresponds to the set of thermocouples approximately 21 cm from the exhaust plume exit plane, and region two corresponds to

the set of thermocouples approximately 42 cm from the exhaust plume exit plane. Eight pixels in region one and nine pixels in region two were averaged together to produce the approximate temperatures representative of the thermocouples, as determined by the model. The recovery temperatures captured by the thermocouples were converted to static temperatures, as discussed in Appendix A.

Table 2. Model determined average temperatures associated with two regions of the scene corresponding to the two thermocouple locations, thermocouple static temperatures for the axial position, and the difference between the two. Region one corresponds to the set of thermocouples approximately 21 cm from the exhaust plume exit plane, and region two corresponds to the set of thermocouples approximately 42 cm from the exhaust plume exit plane.

Fuel Type, Flow Rate	Thermocouple One, Average Static Temperature (K)	Region One, Average Temperature (K)	Difference (K)	Thermocouple Two, Average Static Temperature (K)	Region Two, Average Temperature (K)	Difference (K)
Diesel 300 cm ³ /min	719	968	249	522	734	212
Diesel 225 cm ³ /min	699	907	208	505	685	180
Kerosene 300 cm ³ /min	702	979	277	525	728	203
Kerosene 225 cm ³ /min	668	874	206	503	662	159

Due to the many approximations and assumptions necessary to produce a radiative transfer model capable of running in a reasonable amount of time, the model was biased to higher temperatures in the plume at each pixel, but remained within approximately 212 K, on average. Because it is assumed that the highest average exhaust plume temperatures will occur on the axis of the turbine engine, only the thermocouples on the axis of the turbine engine were used. These axial thermocouples at the 21 cm and 42 cm positions were the middle thermocouple and the right thermocouple, respectively.

Figure 52 shows the data collected from all three thermocouples at the 21 cm and 42 cm positions, which verifies the assumption that the highest temperatures were found to be on-axis.

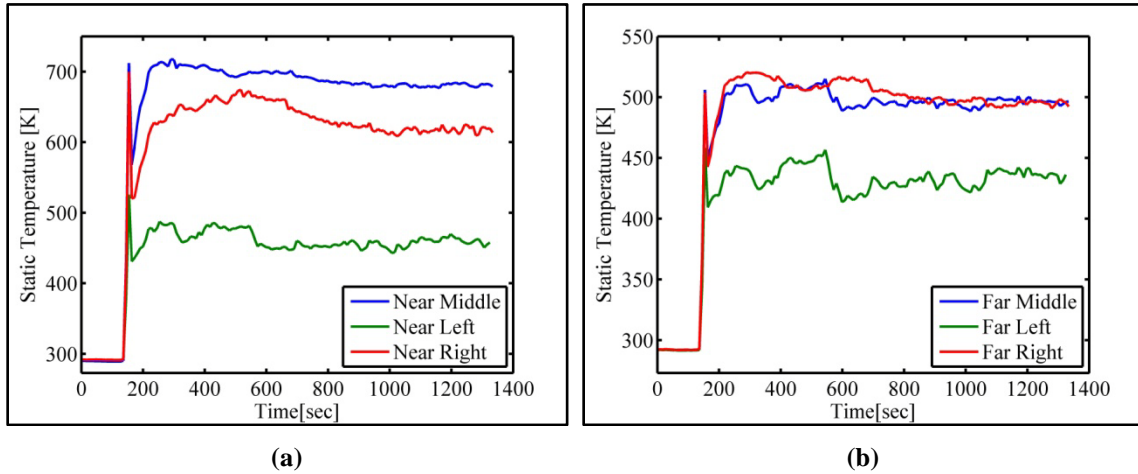


Figure 52. Thermocouple temperature measurements taken over the course of approximately 20 minutes of turbine engine run time at 21 cm (a) and 42 cm (b) from the exhaust plume exit plane, converted to static temperature in K. The on-axis thermocouples exhibited the highest temperatures, as expected. The sharp increase in temperature is due to the initial startup of the turbine engine.

In addition to the thermocouples, Turbine Technologies specifications for the SR-30 turbojet show an outlet exhaust temperature of 993 K [37]. The highest temperature observed at the location of exhaust exit plane as determined by the model, is 1251 K, a difference of 258 K, and the average temperature observed at the location of the exit plane as determined by the model is 1182 K, a difference of 189 K.

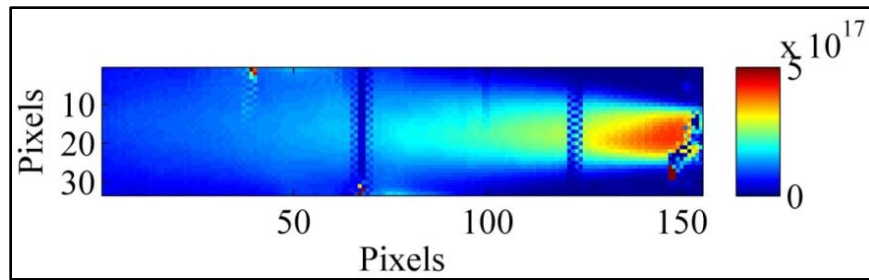
The temperatures measured by the thermocouples were consistently low compared with the temperatures calculated via modeling by approximately 212 K on average. These differences speak to the lack of fidelity in the model, and not on the capability of the FIRST-MWE to collect quality spectra; the spectra were there with decent SNR, as shown previously. The inability to determine accurate temperatures is

due to the many approximations necessary to make the model tractable for spectral fitting. In addition to the approximations and assumptions used in the radiative transfer model, a potential contributing factor to the difference exhibited is the approximation of values used in converting the recovery temperature to static temperature. Analysis of the sensitivity of these values has not been completed at this time.

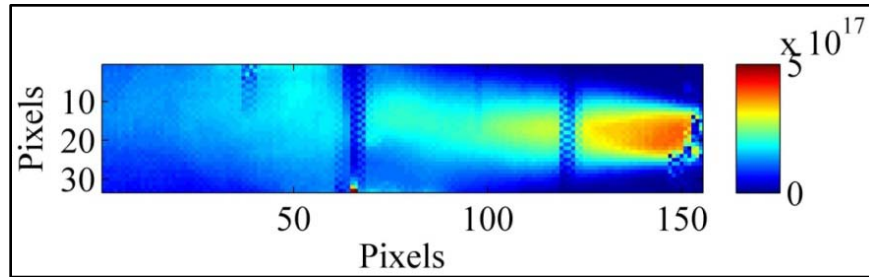
Concentration Spatial Distributions

The CO₂, H₂O, and CO concentration pathlength distributions, in molecules/cm², from the turbine engine exhaust plume are presented in Figures 53-55 for all fuel type and flow rate combinations. The spatial distributions of CO₂ concentration pathlength for the four fuel type and flow rate combinations are compared against one another to highlight the similarities and differences between the spatial distributions. The fuel type has a large impact on the distribution of concentration pathlength, while the fuel flow rate has less of an impact.

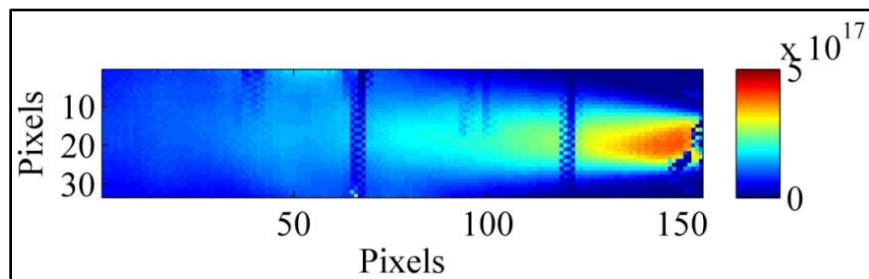
Additionally, theoretical lower and upper limits for the concentrations are calculated and compared with selected pixels for all three chemical species. The theoretical lower limits for CO₂, H₂O, and CO are the molecular concentrations in the ambient atmosphere for the test-day conditions. The theoretical upper limits for CO₂ and H₂O are the concentrations of molecules produced by the turbine engine assuming a perfectly efficient combustion process. The theoretical upper limit for CO is the concentration of molecules produced by the turbine engine assuming 50% combustion efficiency. The concentration pathlength distributions are found to be within the limits determined for CO₂ and CO.



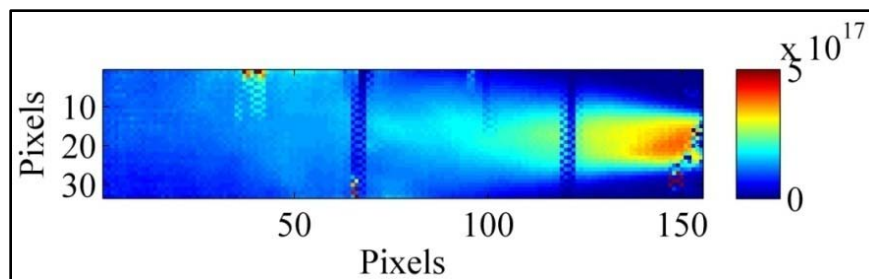
(a)



(b)

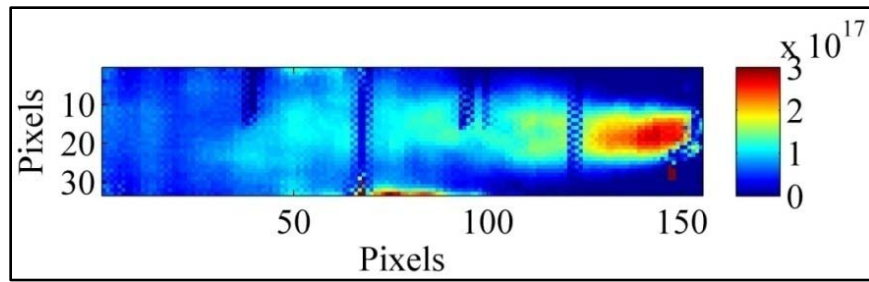


(c)

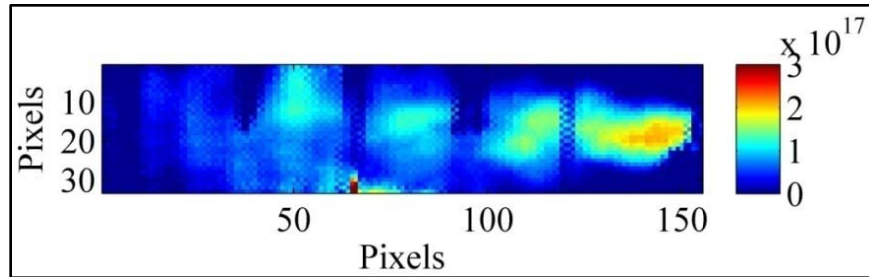


(d)

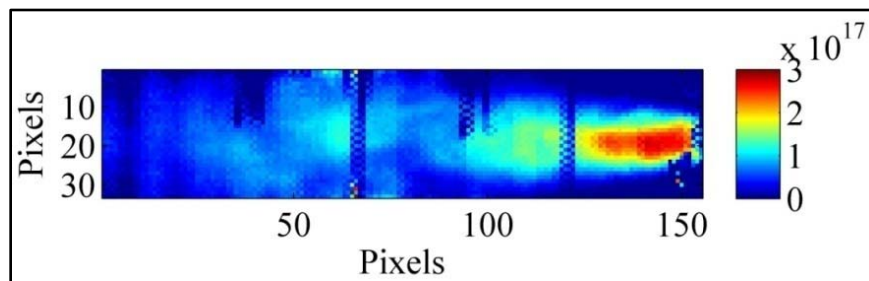
Figure 53. Spatial distribution of CO₂ concentration pathlength for diesel fuel at a 300 cm³/min flow rate (a), diesel fuel at a 225 cm³/min flow rate (b), kerosene fuel at a 300 cm³/min flow rate (c), and kerosene fuel at a 225 cm³/min flow rate (d). The color scale is in molecules/cm².



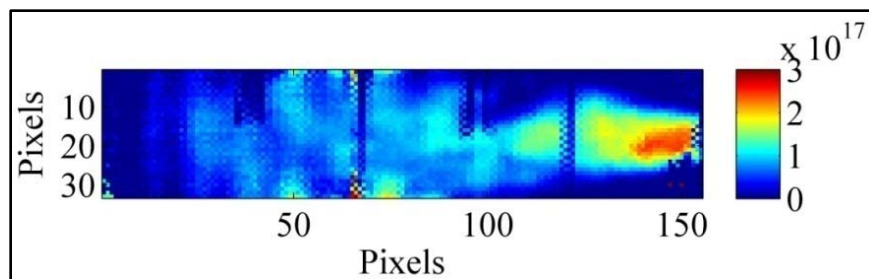
(a)



(b)

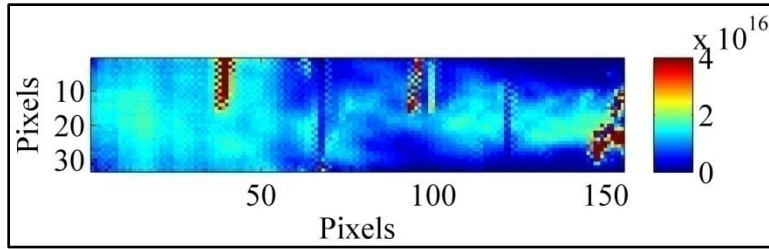


(c)

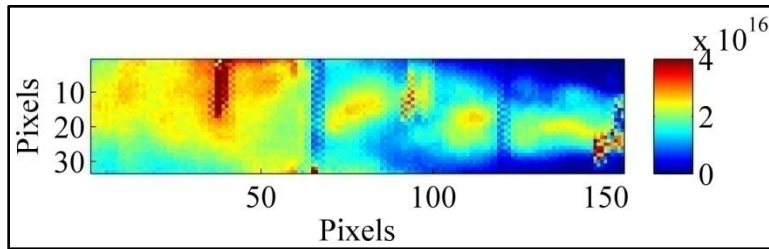


(d)

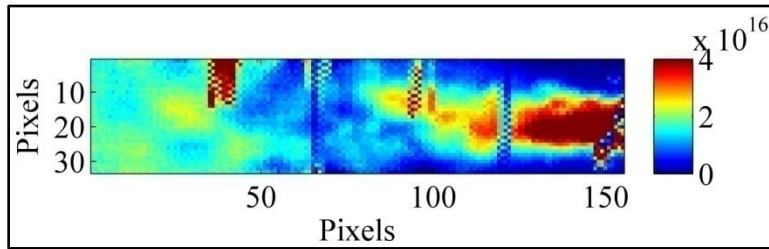
Figure 54. Spatial distribution of H₂O concentration pathlength for diesel fuel at a 300 cm³/min flow rate (a), diesel fuel at a 225 cm³/min flow rate (b), kerosene fuel at a 300 cm³/min flow rate (c), kerosene fuel at a 225 cm³/min flow rate (d). The color scale is in molecules/cm².



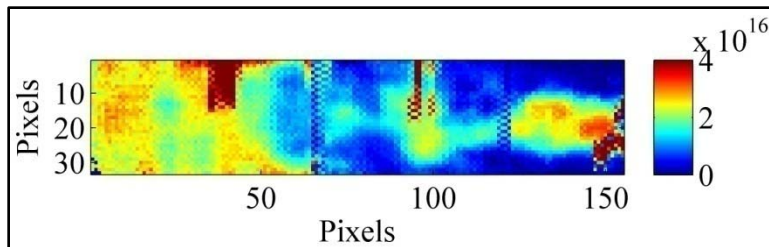
(a)



(b)



(c)



(d)

Figure 55. Spatial distribution of CO concentration pathlength for diesel fuel at a 300 cm³/min flow rate (a), diesel fuel at a 225 cm³/min flow rate (b), kerosene fuel at a 300 cm³/min flow rate (c), kerosene fuel at a 225 cm³/min flow rate (d). The color scale is in molecules/cm².

Distribution Comparisons.

The spatial distributions exhibit expected trends. For all chemical species and fuel types, with the exception of CO with diesel fuel, the concentration pathlength distribution produced by the model from the 300 cm³/min flow rate data produces higher

concentration pathlengths and a greater spatial extent compared to the concentration pathlength distribution produced from the 225 cm³/min flow rate data. The concentration pathlength distribution produced from the 225 cm³/min flow rate data has a lower concentration pathlength for all chemical species, and it exhibits more diffusion into the ambient atmosphere at a location closer to the turbine engine exhaust exit plane.

By comparing chemical species distributions through ratios, it is possible to highlight the similarities and differences found between the concentration pathlength distributions of the four fuel type and flow rate combinations. By displaying a distribution of the ratio of concentration pathlength distributions for the two fuel flow rates, Figure 56 enables visualization of the similarity in the CO₂ spatial distributions found between the two fuel flow rates used in the experiment.

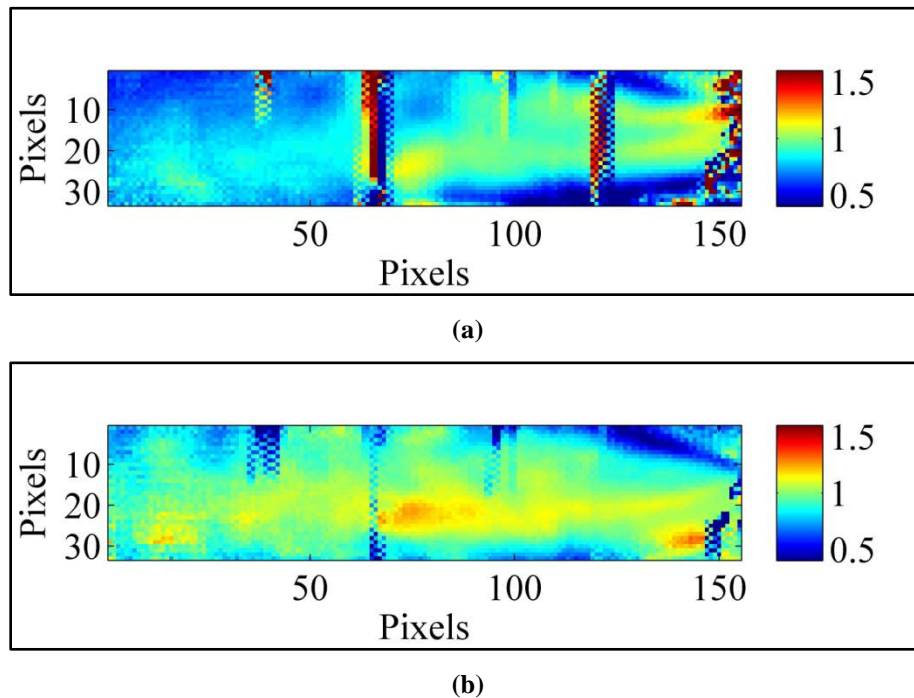


Figure 56. A distribution showing the ratio of the concentration pathlength distributions of the two fuel flow rates, 300 cm³/min to 225 cm³/min, for diesel (a) and kerosene (b). The ratio distribution highlights the fact that the flow rates produce similar concentration pathlength distributions for both fuel types.

The distribution showing the ratio of CO₂ concentration pathlength distributions of differing fuel type highlights the differences between the diesel and kerosene fuels.

Figure 57 shows a distribution of the ratio of the CO₂ concentration pathlength distribution of diesel fuel to kerosene fuel for both fuel flow rate settings, 300 cm³/min and 225 cm³/min.

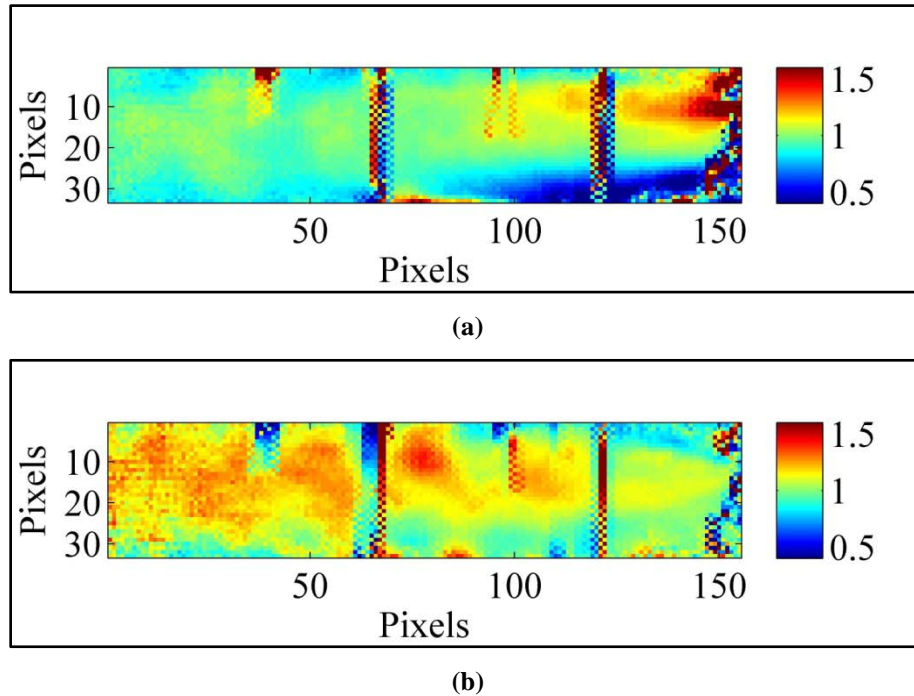
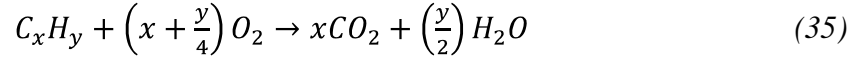


Figure 57. A distribution showing the ratio of the concentration pathlength distributions of the two fuel types, diesel to kerosene, for 300 cm³/min (a), and 225 cm³/min (b). The ratio distribution highlights the differences between the CO₂ concentration pathlength distributions produced by the two fuel types.

Based on a simple analysis of the fuel constituents, it is possible to show that the two fuels release similar amounts of CO₂, but that the diesel fuel releases more, indicating that a ratio slightly greater than unity is to be expected. The average diesel fuel formula is C₁₂H₂₃, and the average kerosene fuel formula is C₁₂H₂₆. Using these

formulas and assuming a balanced combustion and complete reaction, the equation governing the fuel chemistry is



where C_xH_y is the fuel formula, x is the number of carbon atoms and y the number of hydrogen atoms; O_2 is the oxygen diatomic. The amount of CO_2 released, Δ_{CO_2} , is obtained by

$$\Delta_{CO_2} = x \frac{MW_{CO_2}}{MW_{Fuel}} \quad (36)$$

where $MW_{CO_2} = 44.001$ g/mol is the molecular weight of CO_2 , and MW_{Fuel} is the molecular weight of the fuel. The CO_2 released for diesel and kerosene are 3.162 and 3.106 g CO_2 /g fuel, respectively. The similarity between these values indicates that differences between fuel types will be small, but assuming a similar combustion efficiency for the two fuel types, diesel fuel will have more CO_2 in the exhaust plume than kerosene.

Lower and Upper Limits on Concentrations.

In situ chemical species measurements were not performed, and thus it is not possible to determine the accuracy of the chemical species concentration pathlength spatial distributions. However, it is possible to compare the concentration pathlengths produced by the model to the limits which the chemical species concentrations should take on. By calculating the lower and upper bounds the chemical species concentrations must reside between, it is possible to evaluate, in an approximate way, the results produced by the model. By assuming an axial symmetry of the plume, approximate pathlengths are obtained from the scene in order to convert to concentration. The

concentrations determined by the model in the hot parts of the plume should not be less than normal atmospheric levels, and should not be more than the turbine engine releases.

The only chemical species in the atmosphere that was directly measured was H₂O. This equates to a 10200 ppmv concentration of H₂O in the ambient atmosphere. The atmospheric levels for CO₂ and CO must be taken from the average daily values of 388 ppmv and 177 ppmv, respectively. These concentrations equate to 2.5×10^{17} , 9.4×10^{15} , and 4.3×10^{15} molecules/cm³ for H₂O, CO₂, and CO, respectively. The upper limit is calculated from the total engine flow using the conservation of mass. For diesel fuel, these were determined to be 7.9×10^{17} , 8.3×10^{17} , and 4.2×10^{16} molecules/cm³ for H₂O, CO₂, and CO, respectively, and for kerosene fuel these were determined to be 8.8×10^{17} , 8.1×10^{17} , and 4.1×10^{16} for H₂O, CO₂, and CO, respectively. The calculations used to determine these limits are shown in Appendix C.

Figure 58 shows the model fit to the spectrum at pixel (165, 28), where the SNR was 9.3. The approximate pathlength through the plume was 2.4 cm, achieved by assuming an axial symmetry, and using the spatial information provided by the distributions. The model fit the spectrum well in the CO₂ and CO spectral regions, and determined concentrations of 9.1×10^{16} molecules/cm³ of H₂O, 1.4×10^{17} molecules/cm³ of CO₂, and 1.8×10^{16} molecules/cm³ of CO. The data was from the kerosene fuel, 225 cm³/min flow rate dataset.

Figure 59 shows the model fit to the spectrum at pixel (167, 35), where the SNR was 10.9, and the approximate pathlength through the plume was 2.4 cm. The model fit the spectrum well in the CO₂ and CO spectral regions, and determined concentrations of 8.8×10^{16} molecules/cm³ of H₂O, 1.3×10^{17} molecules/cm³ of CO₂, and 1.6×10^{16}

molecules/cm³ of CO. The data was from the kerosene fuel, 225 cm³/min flow rate dataset.

Figure 60 shows the model fit to the spectrum at pixel (170, 32), where the SNR was 17.3, and the approximate pathlength through the plume was 2.4 cm. The model fit the spectrum in the CO₂ and CO spectral regions, and determined concentrations of 1.1x10¹⁷ molecules/cm³ of H₂O, 1.6x10¹⁷ molecules/cm³ of CO₂, and 2.3x10¹⁶ molecules/cm³ of CO. The data was from the kerosene fuel, 225 cm³/min flow rate set.

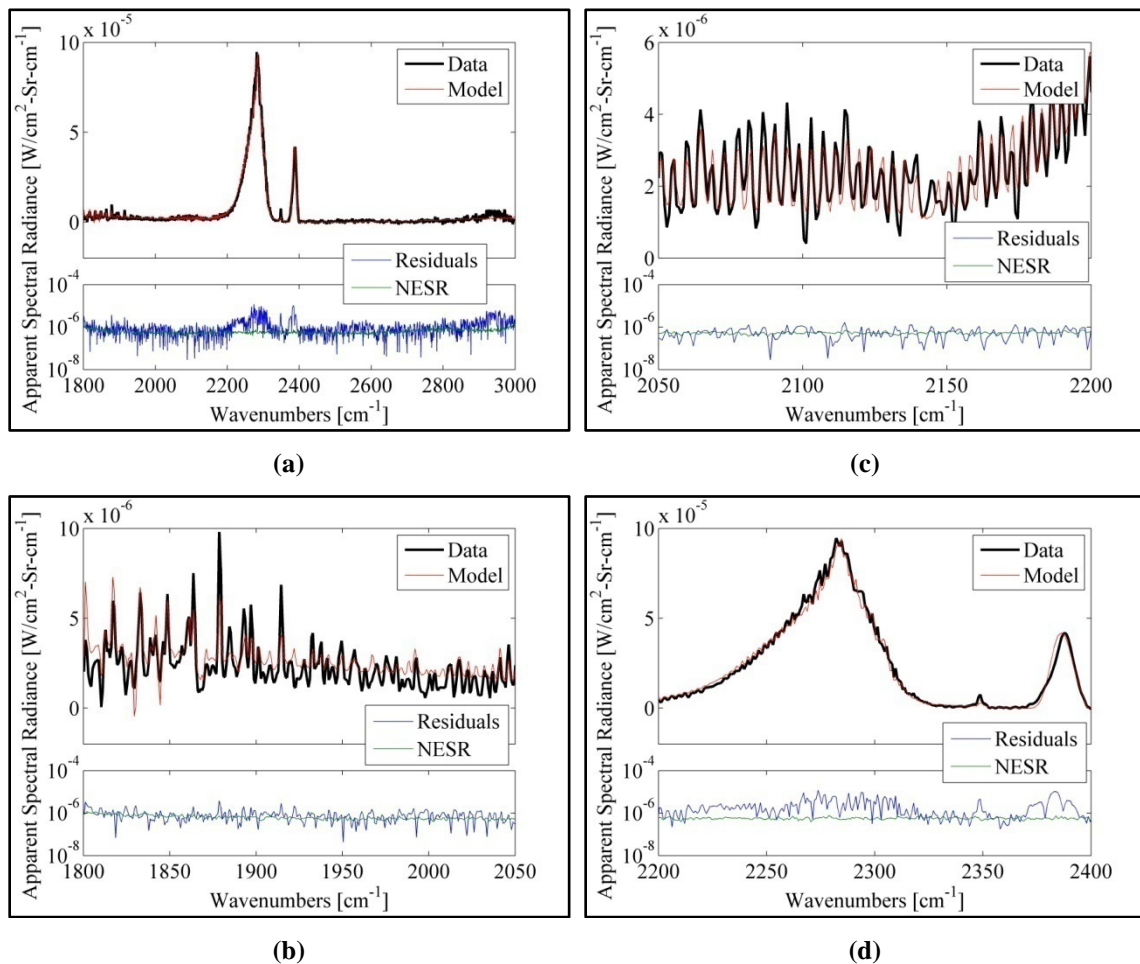


Figure 58. The model (red) fit to the spectrum (black) of pixel (165, 28), where the SNR was 9.3 and the pathlength approximately 2.4 cm. The residuals (blue) and NESR (green) are also shown. The full spectral region (a), as well as the regions of H₂O (b), CO (c), and CO₂ (d) are shown. The concentrations of CO₂, H₂O, and CO were determined by the model to be 1.4x10¹⁷, 9.1x10¹⁶, and 1.8x10¹⁶ molecules/cm³, respectively.

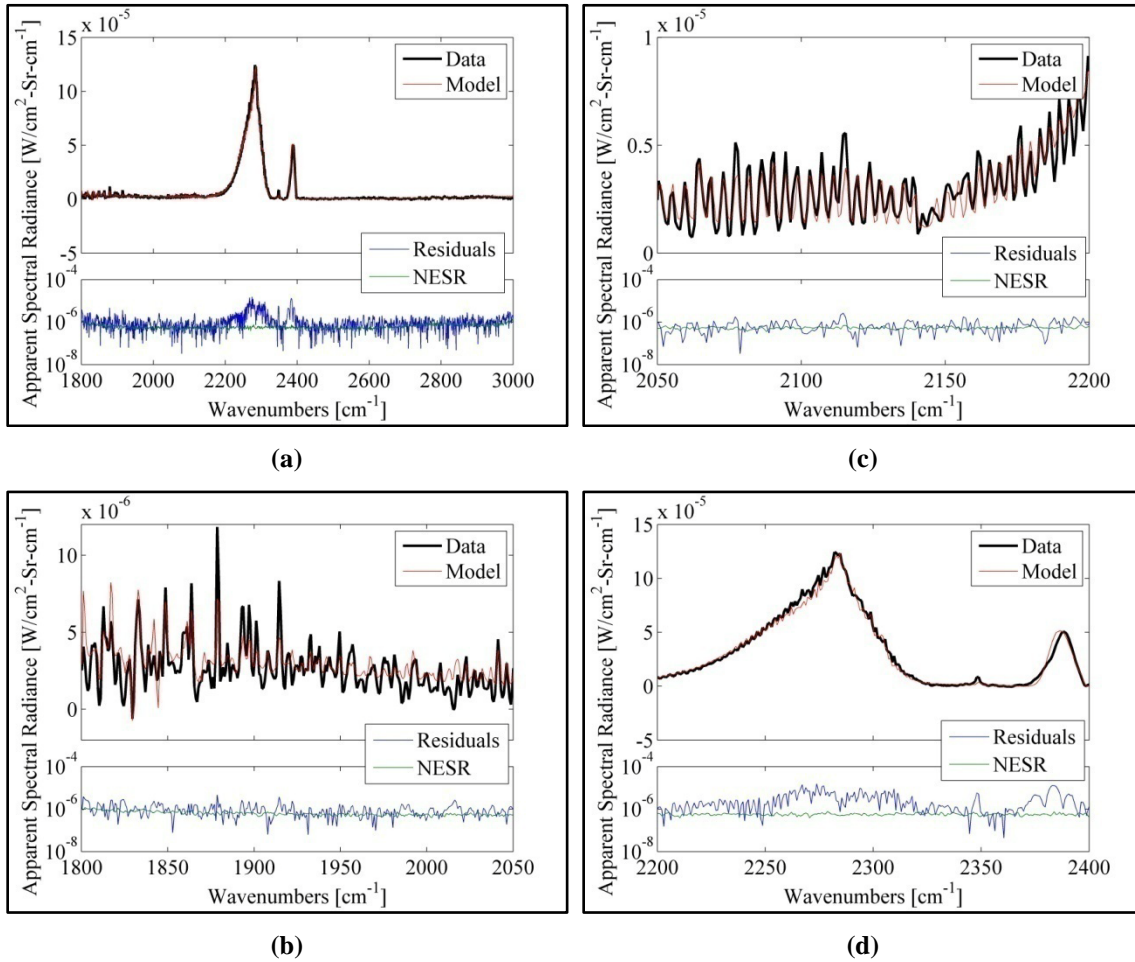


Figure 59. The model (red) fit to the spectrum (black) of pixel (167, 35), where the SNR was 10.9 and the pathlength approximately 2.4 cm. The residuals (blue) and NESR (green) are also shown. The full spectral region (a), as well as the regions of H₂O (b), CO (c), and CO₂ (d) are shown. The concentrations of CO₂, H₂O, and CO were determined by the model to be 1.3×10^{17} , 8.8×10^{16} , and 1.6×10^{16} molecules/cm³, respectively.

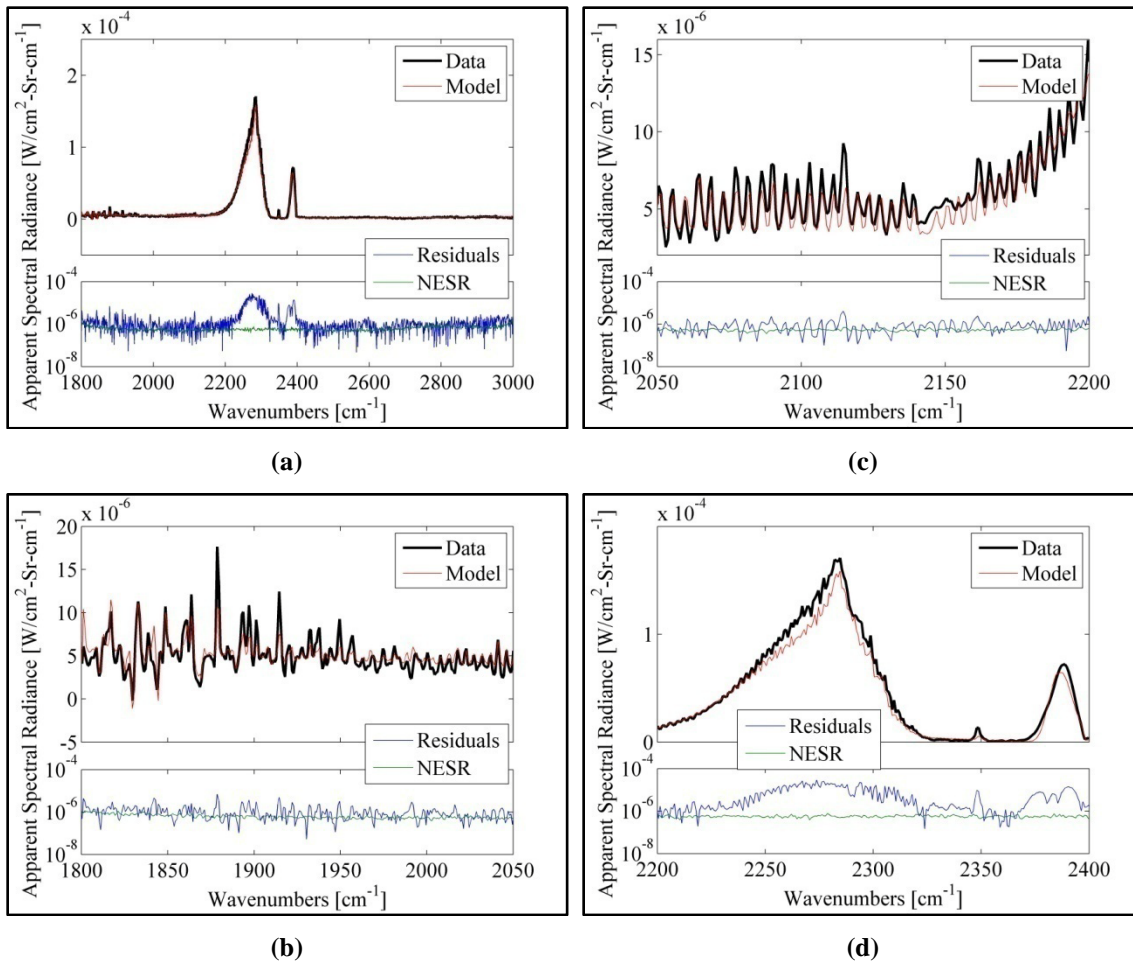


Figure 60. The model (red) fit to the spectrum (black) of pixel (170, 32), where the SNR was 17.3 and the pathlength approximately 2.4 cm. The residuals (blue) and NESR (green) are also shown. The full spectral region (a), as well as the regions of H₂O (b), CO (c), and CO₂ (d) are shown. The concentrations of CO₂, H₂O, and CO were determined by the model to be 1.6×10^{17} , 1.1×10^{17} , and 2.3×10^{16} molecules/cm³, respectively.

The examples in Figures 58 – 60 illustrate the ability of the model to determine concentrations of CO₂, H₂O, and CO that are generally within the bounds set by the atmospheric concentration levels at the lower limit, and concentrations output by the plume. The chemical species that did not always fall within the bounds was H₂O, which had the fewest spectral features with lowest SNR, making it doubly difficult for the

model to fit. It is not possible at this time to say more regarding the quality or accuracy of the concentration pathlength spatial distributions without further analysis.

Summary

Spatial distributions of apparent radiance, temperature, and concentration pathlengths of CO₂, H₂O and CO were presented, as well as apparent spectral radiance plots of selected pixels. The apparent spectral radiance plots included calibration uncertainty limits, which provided insight into the quality of the calibrated spectra. A spatial distribution of the average percent standard deviation was also presented, showing the main cause of calibration uncertainty is due to SCAs created by variations in the plume. A technique to decrease the calibration uncertainty was described, focusing on one way in which turbine engine exhaust plume spectra could be collected while minimizing SCAs.

The spatial distributions of temperature were presented with a brief comparison between the temperature distributions from the different fuel types and fuel flow rates used in the operation of the turbine engine. The temperature appears to vary greatly with fuel flow rate, and minimally with fuel type. A comparison with the *in situ* thermocouple measurements was conducted, with temperatures differing by more than 200 K. This difference is attributed to the low fidelity of the model, and not the capability of the FIRST-MWE to collect high quality calibrated spectra.

Concentration pathlength distributions were presented for CO₂, H₂O, and CO. The CO₂ distributions were compared with each other, showing the variation in fuel type had a greater impact on the distribution than the variation in flow rate. This variation was

developed by looking at the CO₂ release rates for diesel and kerosene, which verified the finding that diesel fuel should release slightly more CO₂ than kerosene fuel, assuming the turbine engine is operating at similar combustion efficiencies. Lower and upper bounds on the concentration of CO₂, H₂O, and CO were presented along with the results of selected pixels. By approximating the pathlength within the plume, using an axial symmetry approximation, the concentrations of CO₂, H₂O and CO were determined. It was found that CO₂ and CO fell within the concentration bounds, while H₂O was found to have a concentration too low. Due to the model's ability to extract concentrations of CO₂ and CO that were within bounds, this discrepancy is attributed to the small number and SNR of the spectral emission features of H₂O.

VII. Conclusions

A review of current efforts in the field of hyperspectral sensing of turbine engines was presented, as well as the characterization of the processes necessary to produce calibrated data using the Telops FIRST-MWE. These background topics were located in Chapter II. A description of the experimental setup was provided in Chapter III. Characterization of the FIRST-MWE, to include characteristics of the focal plane array (FPA) and scene change artifacts (SCAs) were presented in Chapter IV. Focal plane array characterization included a determination of the non-uniformity correction (NUC) and spectral gain and offset for the FIRST-MWE. The error analysis and radiative transfer equations necessary to produce calibrated spectral distributions, temperature and concentration distributions, and calibration uncertainties were presented in Chapter V. In Chapter VI, a discussion of results and analysis was completed for spectral radiance, temperature, and concentration pathlength spatial distributions.

The goal of this effort was to demonstrate the capability of IFTS technology to obtain high quality hyperspectral datacubes remotely collected against the exhaust plume of a turbine engine. This was accomplished by demonstrating the production of spatially and spectrally resolved hyperspectral datacubes of radiometrically calibrated apparent spectral radiance, presenting the uncertainty in the spectral radiance measurement, and developing processes that extract spatial distributions of relative temperature and chemical species concentration from the hyperspectral datacube using the Telops FIRST-MWE.

The impact of SCAs was explored in detail, with the result that temporal averaging of hyperspectral datacubes reduced the impact of SCAs while increasing SNR, without the need for data filtering. By averaging enough hyperspectral datacubes, the impact of SCAs can be minimized and a recognizable spectrum appears with information about the relative concentrations and approximate temperatures throughout the scene.

This result was the first work accomplished towards determining the validity of applying IFTS technology to highly turbulent turbine engine exhaust plumes. Additionally, this result, which demonstrated the utility of IFTS technology in applications involving highly turbulent turbine engine exhaust plumes, enabled further research into the extraction of temperature and chemical species concentration pathlength distributions.

Due to the large variation in the spectra introduced by SCAs, the calibrated spectra were found to have 35% uncertainty in the $1800 - 2500 \text{ cm}^{-1}$ ($4 - 5.5 \text{ }\mu\text{m}$) region for pixels with signal-to-noise ratio (SNR) greater than 1.5. These calibrated hyperspectral datacubes of turbine engine exhaust plumes represent the first achieved to date. They enable future comparison with computational fluid dynamics models produced by engine manufacturers, and the potential for computation of emission indices without need for costly and time consuming *in situ* measurements.

In situ temperature measurements were compared with results extracted from the spectra, with agreement within 212 K, and concentration pathlengths for CO_2 and CO were found to be within expected limits. Discrepancies between *in situ* temperature measurements and temperatures extracted from the spectra were attributed to the many approximations and assumptions made in order to produce a computationally efficient,

tractable model. Disagreement between the calculated lower limit of H₂O concentrations and the concentrations extracted from the spectra were attributed to the weak and infrequent H₂O spectral emissions. These results represent the first documented extraction of turbine engine exhaust plume temperature and chemical species concentration spatial distributions from an IFTS collected hyperspectral datacube. Additionally, the milestones achieved by these initial results lay out a path toward better accuracy in the production of temperature and concentration pathlength distributions.

Through the methods demonstrated here, it has been shown that IFTS technology is able to collect hyperspectral datacubes of high quality despite the presence of SCAs in the data. The datacubes were calibrated with low uncertainty, and spatial distributions of spectral radiance were produced. Through further analysis, temperature and chemical species concentration pathlength distributions were obtained. This work demonstrates a novel capability, and with additional effort, will produce even more remarkable results. Some areas where the presented work would most greatly benefit from additional attention are highlighted in the following section.

Future Work

With further analysis, it is possible to achieve more accurate results in the temperature and chemical species concentration pathlength distributions. To that end, three areas of additional research are proposed: experimental work to characterize the equipment, modeling work to refine the fitting techniques, and theoretical work to more fully comprehend the impact of assumptions.

The recommended experimental work involves performing *in situ* measurements of the chemical species concentrations, taking *in situ* measurements of the total and static pressures in order to accurately convert thermocouple recovery temperature to static temperature, and accurately measuring the characteristics of the turbine engine under study while collecting hyperspectral datacubes.

In order to accurately measure the characteristics of the turbine engine under study, it is highly recommended that installation of additional or improved instrumentation to capture accurate values for the engine fuel flow rate, thrust, and exhaust gas temperature is accomplished. It is critical for any future experimental campaign to fully document the performance parameters of the engine under study during remote hyperspectral data collection, to enable repeatability and further analysis.

The recommended theoretical work includes studying the impact of the assumption that average plume temperatures and chemical species concentration pathlengths are able to represent temporally averaged spectra of a changing temperature and chemical species concentration pathlengths. An additional point of research is studying the expected differences between the fuel types and flow rates, based on a more comprehensive understanding of fluid dynamics and chemical kinetics.

The recommended modeling work focuses efforts on the underlying causes of the differences in temperatures between the spectrally extracted temperatures and the thermocouples. A potential path of research explores the impact a temperature and chemical species concentration gradient within the plume, as well as the impact instantaneous magnitude fluctuations, has on the spectrum.

Exploration of the temperature gradient has been accomplished to a minimal degree. A radiometric model accounting for two separate, radially distributed temperature regions within the plume was developed. This model was only applicable for pixels on the center line of the plume because it was not able to account for differing path lengths, a critical factor when using multiple temperatures. The model was unfeasible to implement due to the computational intensity, requiring thousands of hours of computation time for a single distribution.

Another path of exploration involves the assumption of axial symmetry in the turbine engine exhaust plume. Using the two-dimensional spatial distribution of spectral radiance, it is possible to perform an inverse Abel transform of the data to retrieve the radial distribution of spectral radiance. Work citing the usage of Abel transforms has been included [38, 39], and scripts have been written in MATLAB for this application, which can be found in Appendix D.

The Abel transform method requires the assumption of axial symmetry. Work has been accomplished to characterize the temperature variation in the exhaust output of the Turbine Technologies SR-30 turbojet, which has shown a non-uniform, non-symmetric variation in temperature [40]. In order to acquire suitable data for an Abel transform, data collection against a turbine engine manufactured for commercial use would be necessary, due to the axial symmetry and relatively uniform flow commercial turbines are designed to exhibit. Using this methodology against a commercial aircraft turbine engine would also demonstrate the applicability to the user community.

One additional area of future work is an acoustic vibration survivability study. This study would determine the safe operating distance the Telops FIRST-MWE must

maintain when collecting against commercial aircraft turbine engines in order to remain operationally sound. The commercial aircraft turbine engines emit strong acoustic vibrations, which impact the operation of an IFTS due to the requirement to know the mirror position very precisely. Characterizing this susceptibility would aid in determining the operational usefulness of the Telops FIRST-MWE and the methodologies developed here.

Final Remarks

This document demonstrated the capability IFTS technology to produce spatially and spectrally resolved hyperspectral datacubes of calibrated apparent spectral radiance collected against the exhaust plume of a turbine engine, despite the turbulent exhaust flow of the turbine engine exhaust plume. That information was used in the initial steps of building the capability to extract temperature and chemical species concentration pathlength distributions, which produced the first results developed by this method. Although the spatial distributions require additional work, this first step has shown the value in this research area, and has highlighted paths to even better results.

Appendix A. Recovery and Static Temperature

The thermocouples reported recovery temperature measurements instead of static temperature measurements. Static temperature is what was extracted from the exhaust plume spectra, so a conversion was necessary. The recovery temperature is related to static temperature by

$$T_s = \frac{T_r}{1+r M^2 \frac{\gamma-1}{2}} \quad (37)$$

where T_s is the static temperature, T_r is the recovery temperature measured by the thermocouples, r is the boundary layer recovery number, M is the Mach number, and $\gamma = c_p/c_v$ is the specific heat ratio. The boundary layer recovery number, Mach number, and specific heat ratio are approximated using the recovery temperature measurements and the atmospheric pressure. This gives approximate values of $r = 0.88$, $M = 0.7$, and $\gamma = 1.36$, for the thermocouples located 21 cm from the exhaust plume exit plane, and $r = 0.88$, $M = 0.7$, and $\gamma = 1.38$ for the thermocouples located 42 cm from the exit plane [41]. These values were used in the reporting of temperatures in Table 2.

Appendix B. Data Averaging Methods

As discussed in Chapter IV, it is necessary to average or find the median of the data over all datacubes in order to reduce the affect of SCAs on SNR. This process of data averaging, although straightforward, presented some unexpected results attributable to the phase correction method implemented while performing the discrete Fourier transform. Two theoretically equivalent methods of data averaging were explored. The results were the same, but not without first uncovering an unresolved issue with the phase correction. The first method averaged hyperspectral datacubes in the spectral domain, the second in the spatial domain.

Although it requires significantly more processing time, averaging hyperspectral datacubes in the spectral domain, after the Fourier transform, has advantages over averaging in the spatial domain before the Fourier transform. The size of the data is reduced to only the frequency band of interest, producing an order of magnitude reduction in the size of the hyperspectral datacube. The error analysis is simpler as well, removing the need to propagate error through the Fourier transform.

To average the hyperspectral datacubes in the spectral domain, the raw data at each pixel was Fourier transformed with a Hamming apodization function and a Mertz phase correction over the spectral range $1600 - 3000 \text{ cm}^{-1}$ ($3.33 - 6.25 \text{ }\mu\text{m}$). The Hamming apodization function removes spectral noise at the cost of resolution, and the Mertz phase correction accounts for any unevenness in the interferograms due to mirror sampling, which would otherwise cause energy to remain in the imaginary component.

To average the raw hyperspectral datacubes in the interferogram domain, all hyperspectral datacubes were averaged together, forward sweep direction separate from

the reverse mirror sweep direction, producing a mean and standard deviation for each pixel's interferogram for the two directions. The two average interferograms were then Fourier transformed using a Hamming apodization function and Mertz phase correction, and averaged together in the spectral domain.

An issue arose when comparing the average spectra using the two methods.

Figure 61 shows the two uncalibrated spectra, averaged in the spectral domain and the spatial domain, respectively. In Figure 61 (b), the spectral region of interested, 2500 – 5000 cm^{-1} (2 – 4 μm) has been focused on in order to emphasis the issue at hand. The spectral features of H_2O and CO_2 , observed at 1800 – 2000 cm^{-1} (5 – 5.5 μm) and 2250 – 2400 cm^{-1} (4.2 – 4.4 μm), respectively, are due to atmospheric absorbance along the path inside the instrument, between the front optic and the detector.

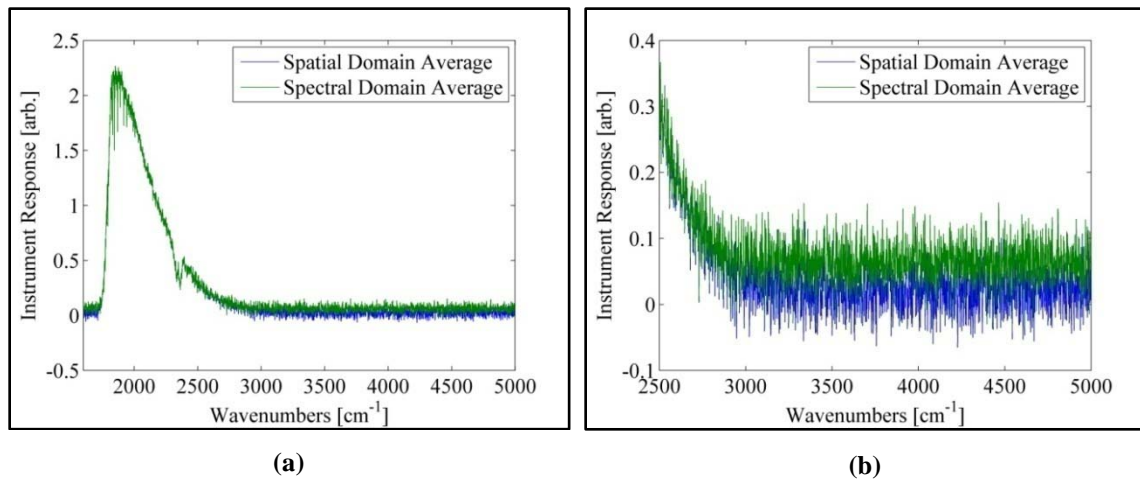


Figure 61. A spatial domain average (blue) and a spectral domain average (green) of twenty hyperspectral datacubes observing a blackbody at 80 °C, over the spectral range 1800 – 5000 cm^{-1} (2 – 5.56 μm) (a), and 2500 – 5000 cm^{-1} (2 – 4 μm) (b). The spatial average performed only a single Mertz phase correction, while the spectral average performed twenty. The non-zero energy in the spectrum of the spectral domain average at wavenumbers greater than 3000 cm^{-1} (3.33 μm) is unphysical.

As can be seen in Figure 61, the spatial domain averaged spectra approaches zero signal at higher wavenumbers, and the spectral domain averaged spectra does not. Both the spectral response and the radiance from the 80 °C blackbody under observation approach zero in this region, which means that energy has been added during the spectral domain average process, which is unphysical.

It was postulated that the increased signal in the wavenumber region above 3000 cm^{-1} ($3.33 \mu\text{m}$) was due in some way to the Mertz phase correction; either the theory or the implementation of theory was to blame. To test this, the interferogram at each pixel from each hyperspectral datacube in the set was Fourier transformed with a Hamming apodization function, but without a Mertz phase correction. The complex spectra were averaged in the spectral domain, and the Mertz phase correction was implemented to produce the averaged hyperspectral datacube. Figure 62 shows this reduced the signal seen in the high wavenumber region of the spectra.

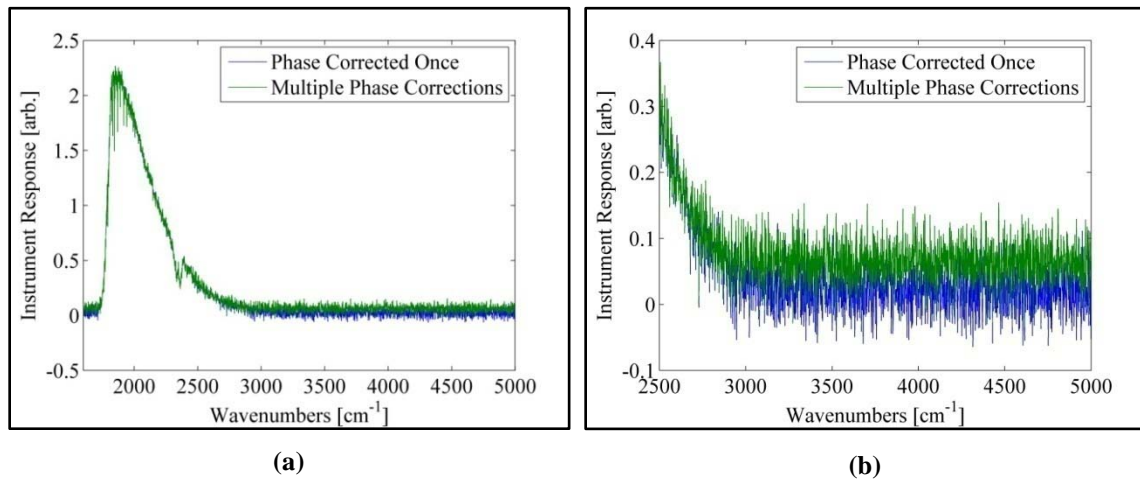


Figure 62. A spectral domain average with only one phase correction (blue) and a spectral domain average with multiple phase corrections (green), observing a blackbody at 80 °C, over the spectral range 1800 – 5000 cm^{-1} (2 – 5.56 μm) (a), and 2500 – 5000 cm^{-1} (2 – 4 μm) (b). The singly phase corrected spectrum approaches zero signal at high wavenumbers, and the multiply phase corrected spectrum does not.

Although the root cause has not been identified, it has been determined that with the current implementation, multiple applications of Mertz phase correction impacts the resultant spectrum when dealing with discrete data. With the new method of correcting phase, there is essentially no difference between the spectra produced via averaging in the spectral domain versus averaging in the spatial domain.

Appendix C. Atmospheric Constituent Concentrations

The lower and upper limits of the chemical species concentrations were determined using information pulled from a number of sources. The lower bound for the chemical species concentrations in the hot part of the plume was the atmospheric concentration. At this theoretical limit, the plume is emitting no CO₂, H₂O, or CO. The emission features are due solely to atmospheric chemical species heated by the hot gas of the turbine.

Measurements of atmospheric H₂O were collected by the AFWA, reported in Table 1 as Dew Point. Conversion from Dew Point to the concentration of H₂O in ppmv and molecules/cm³ is performed by first computing the vapor pressure of H₂O, e_{H_2O} , using the Goff-Gratch equation;

$$\begin{aligned} \log_{10}(e_{H_2O}) = & -7.90298 \left(\frac{T_s}{T} - 1 \right) + 5.02809 \log_{10} \left(\frac{T_s}{T} \right) \\ & -1.3816 * 10^{-7} \left(10^{11.344(1 - T_s/T)} - 1 \right) \\ & +8.1328 * 10^{-3} \left(10^{-3.49149(T_s/T - 1)} - 1 \right) + \log_{10}(101324.6) \end{aligned} \quad (38)$$

where $T_s = 373 \text{ K}$ is the steam point, and T is the ambient temperature. Once the vapor pressure of H₂O is determined, it is used to compute the ambient humidity ratio, w_{amb} ;

$$w_{amb} = \frac{(MW_{H_2O}/MW_{Air})e_{H_2O}}{P_{amb} - e_{H_2O}} \quad (39)$$

where P_{amb} is the ambient pressure as reported in Table 1, and taken as an average value of 98.9 kPa. The humidity ratio is used to determine the ppmv [42];

$$\chi_{H_2O} = \frac{w_{amb}/MW_{H_2O}}{w_{amb}/MW_{H_2O} + 1/MW_{Air}} \quad (40)$$

where χ_{H_2O} is the concentration of H₂O in ppmv.

No measurements were taken to determine the CO₂ and CO concentrations during the experimental campaign of 5 November, so the standard outdoor atmospheric concentrations of CO₂ and CO are used. They are 388 ppmv and 177 ppmv for CO₂ and CO, respectively [12, 43].

The chemical species concentrations, now in ppmv, must be converted to molecules/cm³ for comparison with the model output. Conversion from ppmv to molecules/cm³ requires the Ideal Gas Law,

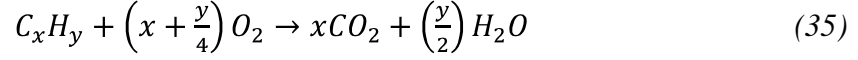
$$\frac{n_x}{V} = \frac{\chi_x P_{amb}}{k_B T_{amb}} \quad (41)$$

where $\frac{n_x}{V}$ is the number density of chemical species x in molecules/cm³, χ_x is the atmospheric concentration of chemical species x in ppmv, $k_B = 1.38 \times 10^{-23} \text{ J K}^{-1}$ is Boltzmann's constant, and T_{amb} is the ambient temperature.

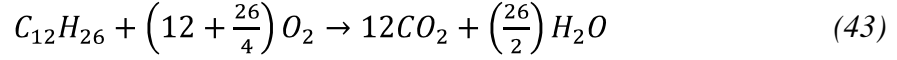
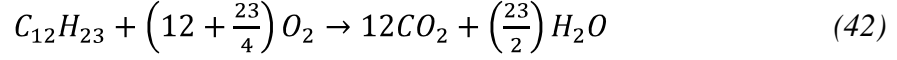
The upper limit of the chemical species concentrations is based on the chemical species production of the SR-30 turbojet. A number of steps are necessary to produce the factor by which the ambient concentrations will scale to represent the upper limit of concentrations within the plume.

It is necessary to assume a combustion efficiency of 100% for the determination of CO₂ and H₂O concentrations, and a combustion efficiency of 90% for the determination of CO concentrations. In this manner, realistic maximum values are achieved for each chemical species.

Assuming 100% combustion efficiency, and a balanced combustion reaction equation, the fuel chemistry will follow Equation (35), repeated here for convenience;



Assuming a diesel fuel formula of $C_{12}H_{23}$ and a kerosene fuel formula of $C_{12}H_{26}$, the reaction equations look like



for diesel and kerosene, respectively. From the reaction equations, the CO_2 and H_2O release rates are determined for both fuel types,

$$\Delta_{CO_2} = x \frac{MW_{CO_2}}{MW_{Fuel}} \quad (44)$$

$$\Delta_{H_2O} = \frac{y}{2} \frac{MW_{H_2O}}{MW_{Fuel}} \quad (45)$$

where $x = 12$ for both fuel types; $y = 23$ for diesel and $y = 26$ for kerosene;

$MW_{diesel} = 167$ g/mol for diesel and $MW_{kerosene} = 170$ g/mol. The release rates for CO_2 and H_2O are $\Delta_{CO_2} = 3.162$ g CO_2 /g diesel and $\Delta_{H_2O} = 1.240$ g H_2O /g diesel, respectively, for diesel and $\Delta_{CO_2} = 3.106$ g CO_2 /g kerosene and $\Delta_{H_2O} = 1.376$ g H_2O /g kerosene, respectively, for kerosene.

Assuming the engine is a control volume, the conservation of mass holds and the total flow in will equal the total flow out. By calculating the air flow in, the H_2O flow in, the fuel flow in, the H_2O flow out, the CO_2 flow out, and the air flow out, it is possible to determine the turbine engine exhaust plume humidity ratio, w_{plm,H_2O} , and the turbine engine exhaust plume CO_2 ratio, w_{plm,CO_2} ;

$$R_{Fuel,in} + R_{Air,in} + R_{H_2O,in} = P_{CO_2,out} + P_{H_2O,out} + P_{Air,out} \quad (46)$$

$$w_{plm,H_2O} = \frac{P_{H_2O,out}}{P_{Air,out}} \quad (47)$$

$$w_{plm,CO_2} = \frac{P_{CO_2,out}}{P_{Air,out}} \quad (48)$$

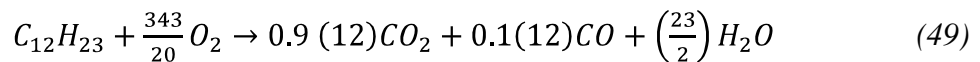
where $R_{Fuel,in}$, $R_{Air,in}$, and $R_{H_2O,in}$ are the fuel, air, and H₂O reactants, respectively, and $P_{CO_2,out}$, $P_{H_2O,out}$, and $P_{Air,out}$ are the CO₂, H₂O, and air products, respectively.

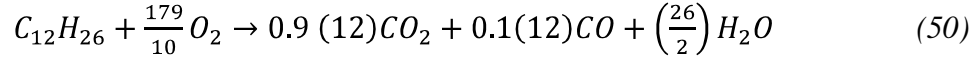
The three in-flows are the same for both fuel types. The fuel flow into the control volume is easily obtained by assuming a specific gravity of diesel and kerosene to both be approximately equal to 0.82. 300 cm³/min equates to approximately 4 g/s, and 225 cm³/min equates to approximately 3 g/s. However, there is no difference in the resulting limits due to varying fuel flow rates, so only the 300 cm³/min fuel flow rate is utilized here. The air flow into the control volume is based on an air-to-fuel-ratio of 62:1 for the SR-30 turbojet [44]. The air in-flow is simply 62 times the fuel in-flow. The H₂O in-flow is the air in-flow multiplied by the previously calculated ambient humidity ratio, w_{amb} .

The three out-flows are specific to the fuel type because they are dependent upon the release rates. The CO₂ and H₂O out-flows are the fuel in-flow rate multiplied by the CO₂ and H₂O release rates, respectively. The air out-flow is determined through knowledge of all the other mass flow rates, using the conservation of mass.

The last step is to convert the turbine engine exhaust plume humidity ratio and CO₂ ratio to ppmv or molecules/cm³ using Equations (40) and (41). The

In order to determine the upper bound on the CO concentrations, the same process is applied; however the combustion reaction equation is modified to account for only 90% efficiency. For diesel and kerosene, the equations become, respectively,





The release rates are calculated in the same way, with $\Delta_{CO} = 0.1006$ g CO/g diesel for diesel and $\Delta_{CO} = 0.0988$ g CO/g kerosene for kerosene. The balance of masses is slightly different;

$$R_{Fuel,in} + R_{Air,in} + R_{H_2O,in} = P_{CO_2,out} + P_{H_2O,out} + P_{CO,out} + P_{Air,out} \quad (51)$$

$$w_{plm,CO} = \frac{P_{CO,out}}{P_{Air,out}} \quad (52)$$

where $P_{CO,out}$ is the CO product out-flow and $w_{plm,CO}$ is the turbine engine exhaust plume CO ratio, in g CO/g Air. The CO product can be converted to ppmv or molecules/cm³ using Equations (40) and (41).

Appendix D. MATLAB Scripts

The following sets of MATLAB scripts were written in order to determine temperature and chemical species concentration pathlength distributions. The first set contains the scripts used to produce the results presented in Chapter VI. These scripts are based on a single plume temperature and single concentration pathlength per chemical species, and as such were the most computationally efficient and practical.

The second set of scripts was used to produce a two-temperature model, which was only good for pixels on the axis of the turbine engine because it was not designed to account for changing pathlengths through the plume. This model requires several minutes to run per pixel, and is therefore an unrealistic solution to the temperature gradient problem.

The third set of scripts is incomplete; they were intended to enable an inverse Abel transform to be completed spectrally. The Abel transform, based on a Fourier and inverse Hankel transform, was never implemented on data.

Model Fitting Scripts

The following MATLAB scripts were written to perform model fitting. These scripts contain the three least squares fitting algorithms, fitting the previously described model to the spectral data. The first algorithm, named *CO₂ Path Recursive Loop Weights*, performs the nonlinear fitting of the atmospheric concentrations of CO₂, H₂O, and CO using the bounded direct search function *fminsearchbnd* and calls the second algorithm. The second algorithm, titled *CO₂ Fit Loop Weights*, performs the nonlinear fitting of the plume temperature and spectral axis multiplier using the bounded direct

search function *fminsearchbnd*, and calls the third algorithm. The third algorithm, titled *Fit Basis Functions Weights v2*, performs linear fitting of the chemical species concentration pathlengths and the baseline polynomial coefficients using the weighted least squares function *lsconv*.

CO₂ Path Recursive Loop Weights.

```

%% Header
clear all
close all
clc
global MATLAB_DIRECTORY;
MATLAB_DIRECTORY = '/home/afiten3/gap09m/sbowen/MatlabScripts/';
addpath(genpath(MATLAB_DIRECTORY));

Filepath = ['/home/scratch2/sbowen/20081105/'...
            '20081105-EngineTestKeroseneFuel/offset_corrected/'];
Datapath = [Filepath 'Figures'];
cd(Filepath);

prefix = 'LowRPM';

%% Optimize CO2 and Background Temp
func = @(param) CO2_fit_loop_Weights...
        (prefix,Filepath,param(1),param(2),param(3));
[x fval exitflag output] = fminsearchbnd...
        (func,[505 1507 3989],[380 177 0],[800 40000 4000]);

save([prefix '_Optimize_CO2_H2O_CO_Weights_TC'],'x')

```

CO₂ Fit Loop Weights.

```

function sseT = CO2_fit_loop_Weights(prefix,Filepath,co2,h2o,co)

global MATLAB_DIRECTORY;
MATLAB_DIRECTORY = '/home/afiten3/gap09m/sbowen/MatlabScripts/';
addpath(genpath(MATLAB_DIRECTORY));

cd(Filepath);

load([prefix, '_Datacube_Mean_Spectra_Cal']);
load('sig_1680');
%% Setup Atmospheres:
wavenumbers = sig;
pathlength = 11.2E-3; % 11.2 m
N = 18956; % number of IFG points
T_atm = 292.61; % atm temperature in Kelvin from FIRST-MWE

```

```

atmos = gen_std_atmos('co2',co2,'h2o',h2o,'co',co,...
    'pathlength',pathlength,'nu_min',min(wavenumbers),'nu_max',...
    max(wavenumbers),'N',N,'temperature',T_atm);
atmos.ILS.function = 'hamming';

[nu,transmittance] = compute_transmittance(atmos,wavenumbers);

%% Model Fit

Temp = zeros(xSize,ySize);

iXX = [124:-1:117 67:-1:59];
iYY = [33 35];
for iX = 1:length(iXX)
    if iX < 9, iY = 1; else iY = 2; end

    nu_min = 1800; nu_max = 3000;
    ix = sig>nu_min&sig<nu_max;
    nu = sig(ix);
    L_obs = squeeze(real(EngineRPM_cal(iXX(iX),iYY(iY),ix))));
    transmittance_nu = transmittance(ix);
    f = @(iT) sum( (fit_basis_fcns_weights_noplot_v2...
        (nu,L_obs,transmittance_nu,iT(1),iT(2)) - real(L_obs)).^2 );
    Tmp = fminsearchbnd(f,[478 1.0000],[275 0.9995],[1500 1.0005]);
    Temp(iXX(iX),iYY(iY)) = Tmp(1);
    sse_tmp = f(Tmp);
    if iX == 1
        sseT = sse_tmp;
    else
        sseT = sseT +sse_tmp;
    end
    [mdl conc] = fit_basis_fcns_weights_noplot_v2...
        (nu,L_obs,transmittance_nu,Temp(iXX(iX),iYY(iY)),Tmp(2));
    disp(sprintf('%d error, column %03d of %03d, row %03d of %03d',...
        sse_tmp,iXX(iX),iYY(iY)));
end

disp(sprintf('%d total error.',sseT));

```

Fit Basis Functions Weights v2.

```

function [mdl,conc] = fit_basis_fcns_weights_v2(nu,L_obs,trans,p1,p4)

% Load molecular cross sections - normalize for numerical stability
nu = nu*p4;
B1 = planckian(nu,p1);
h2o = abs_xs( 1,p1,nu)'.*B1;    m_h2o = max(h2o);    h2o = h2o/m_h2o;
co2 = abs_xs( 2,p1,nu)'.*B1;    m_co2 = max(co2);    co2 = co2/m_co2;
co = abs_xs( 5,p1,nu)'.*B1;    m_co = max(co);    co = co/m_co;

% Stuff for baseline correction
offset = ones(size(nu(:)));
slope = nu(:)/max(nu);

```

```

quad = slope.^2;
cubic = slope.^3;

% Build A matrix for linear fit
A = [h2o' co2' co' offset slope quad cubic];
A = vtimes(A,trans(:));
A = [A offset slope quad cubic];

% Add weights
h2o_reg = 1:263;
co_reg = 264:490;
co2_reg = 491:723;
else_reg = 724:1440;

L_int_h2o = abs(trapz(L_obs(h2o_reg)));
L_int_co = abs(trapz(L_obs(co_reg)));
L_int_co2 = abs(trapz(L_obs(co2_reg)));
L_int_else = abs(trapz(L_obs(else_reg)));

L_int_h2o_N = L_int_h2o/length(h2o_reg);
L_int_co_N = L_int_co/length(co_reg);
L_int_co2_N = L_int_co2/length(co2_reg);
L_int_else_N = L_int_else/length(else_reg);

div = max([L_int_h2o_N L_int_co_N L_int_co2_N]);

W_h2o = (div*length(h2o_reg))/L_int_h2o;
W_co = (div*length(co_reg))/L_int_co;
W_co2 = (div*length(co2_reg))/L_int_co2;
W_else = (L_int_else_N*length(else_reg))/L_int_else;

Weights = [ones(length(h2o_reg),1).*...
           W_h2o; ones(length(co_reg),1).*...
           W_co; ones(length(co2_reg),1).*...
           W_co2; ones(length(else_reg),1).*W_else];

% Do the linear fit
[x,x_err] = lsconv(A,real(L_obs)',Weights);
for ii = 1:3
    if x(ii) < 0, x(ii) = 0; end
end
mdl = A*x;
conc = x./[m_h2o; m_co2; m_co; 1; 1; 1; 1; 1; 1; 1; 1];
baseline1 = x(4).*A(:,4)' + x(5).*A(:,5)' +...
           x(6).*A(:,6)' + x(7).*A(:,7)';
baseline2 = x(8).*A(:,8)' + x(9).*A(:,9)' +...
           x(10).*A(:,10)' + x(11).*A(:,11)';

ax(1) = subplot(6,1,1:3);
plot(nu,real(L_obs),'k','LineWidth',1);hold all;
plot(nu,mdl,'r','LineWidth',1);hold off;
legend('Data','Model')
title(['Temp: ' num2str(round(p1)) ' K, Err: ' ...

```



```

    num2str(sum( (mdl-real(L_obs)')).^2), '%0.2E' ] );
prettyPlot; set(gca, 'XTickLabel', []);

ax(2) = subplot(6,1,4);
plot(nu,abs(real(L_obs)-mdl')/max(abs(real(L_obs)-mdl')), 'b');
legend(['Residuals: ' ...
    num2str(round(10^8*max(abs(real(L_obs)-mdl')))/10^8)]);
prettyPlot; set(gca, 'XTickLabel', []);

ax(3) = subplot(6,1,5);
plot(nu,(x(1).*A(:,1)')/max(x(1).*A(:,1)')); hold all;
plot(nu,(x(2).*A(:,2)')/max(x(2).*A(:,2)'));
plot(nu,(x(3).*A(:,3)')/max(x(3).*A(:,3)')); hold off;
legend(['H_2O: ' num2str(round(10^8*max(x(1).*A(:,1)')))/10^8)], ...
    ['CO_2: ' num2str(round(10^7*max(x(2).*A(:,2)')))/10^7)], ...
    ['CO: ' num2str(round(10^8*max(x(3).*A(:,3)')))/10^8)]);
set(gca, 'XTickLabel', []); prettyPlot;

ax(4) = subplot(6,1,6);
plot(nu,baseline1/max(abs(baseline1)));hold all;
plot(nu,baseline2/max(abs(baseline2)));hold off;
legend(['Baseline 1: ' ...
    num2str(round(10^7*max(abs(baseline1)))/10^7)], ...
    ['Baseline 2: ' num2str(round(10^7*max(abs(baseline2)))/10^7)]);
xlabel('Wavenumbers [cm^{-1}]');prettyPlot;
linkaxes(ax, 'x');
drawnow;
end

```

Two-Temperature Model Scripts

Much like the single-temperature scripts above, these scripts were written to perform model fitting. The scripts contain three least squares fitting algorithms, fitting the model described in Equation (28) to the spectral data for two plume temperature regions. The first algorithm, named *CO₂ Path Recursive Loop 2 Zones*, performs the nonlinear fitting of the atmospheric concentrations of CO₂, H₂O, and CO using the bounded direct search function *fminsearchbnd* and calls the second algorithm. The second algorithm, titled *CO₂ Fit Loop 2 Zones*, performs the nonlinear fitting of chemical species concentration pathlengths in two plume regions, two plume temperatures, a background temperature, and the spectral axis multiplier using the bounded direct search function *fminsearchbnd*, and calls the third algorithm. The third algorithm, titled *Fit*

Basis Functions 2 Zones, forms the model from the parameters given by the second algorithm.

CO₂ Path Recursive Loop 2 Zones.

```

%% Header
clear all
close all
clc
global MATLAB_DIRECTORY;
MATLAB_DIRECTORY = '/home/afiten3/gap09m/sbowen/MatlabScripts/';
addpath(genpath(MATLAB_DIRECTORY));

Filepath = ['/home/scratch2/sbowen/20081105/'...
            '20081105-EngineTestKeroseneFuel/offset_corrected/'];
Datapath = [Filepath 'Figures'];
cd(Filepath);

prefix = 'LowRPM';

%% Optimize CO2 and Background Temp
func = @(param) CO2_fit_loop_2zones...
        (prefix,Filepath,param(1),param(2),param(3),param(4));
[x fval exitflag output] = fminsearchbnd...
        (func,[505 1507 3989 312],[380 177 0 260],[800 40000 4000 800]);

save([prefix '_Optimize_2Zones_CO2_H2O_CO_TB'],'x')

```

CO₂ Fit Loop 2 Zones.

```

function sseT = CO2_fit_loop_2zones(prefix,Filepath,co2,h2o,co,iTB)

global MATLAB_DIRECTORY;
MATLAB_DIRECTORY = '/home/afiten3/gap09m/sbowen/MatlabScripts/';
addpath(genpath(MATLAB_DIRECTORY));

cd(Filepath);

load([prefix, '_Datacube_Mean_Spectra_Cal']);
load('sig_1680');
%% Setup Atmospheres:
wavenumbers = sig;
pathlength = 11.2E-3; % 11.2 m
N = 18956; % number of IFG points
T_atm = 292.61; % atm temperature in Kelvin from Telops FIRST-MWE

atmos = gen_std_atmos('co2',co2,'h2o',h2o,'co',co,...
                    'pathlength',pathlength,'nu_min',min(wavenumbers),...
                    'nu_max',max(wavenumbers),'N',N,'temperature',T_atm);
atmos.ILS.function = 'hamming';

```

```

[nu,transmittance] = compute_transmittance(atmos,wavenumbers);

%% Model Fit

Temp = zeros(xSize,ySize);
iXX = [170 100 1];
iYY = [9 32 56];

for iX = 1:length(iXX)
for iY = 1:length(iYY)
    nu_min = 1800; nu_max = 3000;
    ix = sig>nu_min&sig<nu_max;
    nu = sig(ix);
    L_obs = squeeze(real(EngineRPM_cal(iXX(iX),iYY(iY),ix)))');
    transmittance_nu = transmittance(ix);
    f = @(iT) sum( (fit_basis_fcns_2zones_noplot...
        (nu,L_obs,transmittance_nu,iT(1),iT(2),iT(3),iT(4),...
        iT(5),iT(6),iT(7),iT(8),iT(10),iT(11)) -...
        real(L_obs)).^2 );
    f([1E17 1E17 1E17 1E17 1E16 1E16 1000 1000 300 290 1.0000])
    [Tmp fval exitflag output] = fminsearchbnd(f,...
        [1E17 1E17 1E17 1E17 1E16 1E16 1000 500 300 290 1.0000],...
        [1E10 1E10 1E10 1E10 1E10 1E10 275 275 260 260 0.9995],...
        [1E19 1E19 1E19 1E19 1E19 1E19 1500 1500 360 360 1.0005]);
    if exitflag == 0
        [Tmp fval exitflag output] = fminsearchbnd(f,...
            Tmp,...
            [1E10 1E10 1E10 1E10 1E10 1E10 275 275 260 260 0.9995],...
            [1E19 1E19 1E19 1E19 1E19 1E19 1500 1500 360 360 1.0005]);
    end
    if exitflag == 0
        [Tmp fval exitflag output] = fminsearchbnd(f,...
            Tmp,...
            [1E10 1E10 1E10 1E10 1E10 1E10 275 275 260 260 0.9995],...
            [1E19 1E19 1E19 1E19 1E19 1E19 1500 1500 360 360 1.0005]);
    end
    if exitflag == 0
        [Tmp fval exitflag output] = fminsearchbnd(f,...
            Tmp,...
            [1E10 1E10 1E10 1E10 1E10 1E10 275 275 260 260 0.9995],...
            [1E19 1E19 1E19 1E19 1E19 1E19 1500 1500 360 360 1.0005]);
    end
    sse_tmp = f(Tmp);
    if iX == 1
        sseT = sse_tmp;
    else
        sseT = sseT +sse_tmp;
    end
    disp(sprintf('%d error, pixel %03d, %03d',...
        sse_tmp,iXX(iX),iYY(iY)));
end
end

```

```
disp(sprintf('%d total error.',sseT));
```

Fit Basis Functions 2 Zones.

```
function [mdl,conc] = fit_basis_fcns_2zones(nu,L_obs,trans,...
    q1_1,q1_2,q2_1,q2_2,q3_1,q3_2,p1,p2,p3,p4)
% q1 is H2O concentration
% q2 is CO2 concentration
% q3 is CO concentration
% p1 is plume zone 1 (hot) temp
% p2 is plume zone 2 temp
% p3 is background temp
% p4 is HeNe wavelength modifier

% Load molecular cross sections - normalize for numerical stability
nu = nu*p4;
B1 = planckian(nu,p1);
B2 = planckian(nu,p2);
B3 = planckian(nu,p3);

h2o_1 = q1_1*(abs_xs( 1,p1,nu)');
h2o_2 = q1_2*(abs_xs( 1,p2,nu)');
co2_1 = q2_1*(abs_xs( 2,p1,nu)');
co2_2 = q2_2*(abs_xs( 2,p2,nu)');
co_1 = q3_1*(abs_xs( 5,p1,nu)');
co_2 = q3_2*(abs_xs( 5,p2,nu)');
back = B3;

ep1 = (h2o_1 + co2_1 + co_1);
ep2 = (h2o_2 + co2_2 + co_2);
tp1 = (1 - ep1);
tp2 = (1 - ep2);

mdl = (back.*tp1.*(tp2.^2) +...
    ep2.*B2.*tp1.*tp2 +...
    ep1.*B1.*tp2 + ep2.*B2).*trans;

conc = [q1_1 q1_2 q2_1 q2_2 q3_1 q3_2];
plot(nu,mdl,'g','LineWidth',2);hold on;
plot(nu,real(L_obs),'b');hold off;
legend('Model','Data');
title( ['Temp: ' num2str(round(p1)) ' K, Err: '...
    num2str(sum( (mdl-real(L_obs)).^2),'%0.2E')] );
prettyPlot;
drawnow;
```

Abel Transform Script

The MATLAB script, *Inverse Abel* was intended to enable an inverse Abel transform to be completed spectrally. The inverse Abel transform script, based on a

built-in Fourier transform function, *fft*, and an inverse Hankel transform function, *Inverse_Hankel*, which itself was based on the function *Hankel_transform*, written by Guizar-Sicairos *et al* [45], was able to transform a theoretical top hat function, but was never implemented with real data.

Hankel Transform.

```

%% This routine implements Hankel transforms of integer order based
%% on a Fourier-Bessel series expansion. The algorithm is based on a
%% recently published research work (please cite if used):

%% M. Guizar-Sicairos and J. C. Gutierrez-Vega, Computation of
%% quasi-discrete Hankel transforms of integer order for propagating
%% optical wave fields, J. Opt. Soc. Am. A 21, 53-58 (2004).

%% The numerical method features great accuracy and is energy
%% preserving by construction, it is especially suitable for iterative
%% transformation processes. Its implementation, requires the
%% computation of zeros of the m-th order Bessel function of the first
%% kind where m is the transformation order.

%% An array of the first 3001 Bessel functions of order from zero to
%% four can be found in the "c.mat" array. If a greater transformation
%% order is required the zeros may be found numerically.

%% With the c.mat array, as included, Hankel transforms of order 0-4
%% may be computed, with up to 3000 sampling points. A trasformation,
%% and inverse transformation example is given below.

%% This routine was tested under Matlab 6.5 R13

%%%%%%%%%%%%%%%%%%%%%%%%%%%%%%%%%%%%%%%%%%%%%%%%%%%%%%%%%%%%%%%%%%%%%%%%
%% Input parameters  %%
%%%%%%%%%%%%%%%%%%%%%%%%%%%%%%%%%%%%%%%%%%%%%%%%%%%%%%%%%%%%%%%%%%%%%%%%

R = 4;           % Maximum sampled radius (time or space,
                % how many points are used in transform)
N = 250;        % Number of sampling points (accuracy of result)
ord = 0;        % Transformation order

%%%%%%%%%%%%%%%%%%%%%%%%%%%%%%%%%%%%%%%%%%%%%%%%%%%%%%%%%%%%%%%%%%%%%%%%
%% Matrix and vectors computing  %%
%%%%%%%%%%%%%%%%%%%%%%%%%%%%%%%%%%%%%%%%%%%%%%%%%%%%%%%%%%%%%%%%%%%%%%%%
%% This operations may only be performed once for iterative algorithms

load('I:\My Documents\Thesis\Hankel\c.mat');
c = c(ord+1,1:N+1);

```

```

V = c(N+1)/(2*pi*R);    % Maximum frequency
r = c(1:N)'*R/c(N+1);  % Radius vector
v = c(1:N)'/(2*pi*R);  % Frequency vector

[Jn,Jm] = meshgrid(c(1:N),c(1:N));
C = (2/c(N+1))*besselj(ord,Jn.*Jm/c(N+1))./...
    (abs(besselj(ord+1,Jn)).*abs(besselj(ord+1,Jm)));
% C is the transformation matrix

m1 = (abs(besselj(ord+1,c(1:N)))/R)';
% m1 prepares input vector for transformation
m2 = m1*R/V;
% m2 prepares output vector for display
clear Jn
clear Jm

%%%%%%%%%%%%%%%%%%%%%%%%%%%%%%%%%%%%%%%%%%%%%%%%%%%%%%%%%%%%%%%%%%%%%%%%
%% Transformation example %%
%%%%%%%%%%%%%%%%%%%%%%%%%%%%%%%%%%%%%%%%%%%%%%%%%%%%%%%%%%%%%%%%%%%%%%%%
%% The n-th order Hankel transform of a generalized top-hat function
%% is obtained and compared with the analytic solution, please change
%% transformation order from 0 to 4 to see additional results.

f = (r.^ord).*(r<=1);    % Generalized top-hat function (input)
F = f./m1;               % Prepare vector for transformation
F2 = C*F;                % Obtain the Hankel transform
Fretrieved = C*F2;       % Inverse hankel transform

fretrieved = Fretrieved.*m1; % Prepare vector for display
f2 = F2.*m2;             % Prepare vector for display

%%%%%%%%%%%%%%%%%%%%%%%%%%%%%%%%%%%%%%%%%%%%%%%%%%%%%%%%%%%%%%%%%%%%%%%%
%% Display results %%
%%%%%%%%%%%%%%%%%%%%%%%%%%%%%%%%%%%%%%%%%%%%%%%%%%%%%%%%%%%%%%%%%%%%%%%%

figure,
subplot(2,1,1), plot(r,f), hold on,...
    plot(r,fretrieved,':r'), hold off, xlim([0 4]),
xlabel('r'),
title(sprintf('%d,%d,%d',R,N,ord));
legend('Input function','Retrieved function with IHT'),
v2 = linspace(1e-10,5,300);
fanalytic = besselj(ord+1,2*pi*v2)./v2;
subplot(2,1,2), plot(v,f2,':r'), hold on,...
    plot(v2,fanalytic), hold off, xlim([0 5]),
legend('Transformation results','Analytic Solution'),
xlabel('v')

% All codes were written by Manuel Guizar Sicairos.

```

Inverse Hankel.

```
function [C r v m1 m2] = Inverse_Hankel(R,N,ord)
```

```

%
% [C r v m1 m2] = Inverse_Hankel(R,N,ord), where
%
%   R is the maximum sampled radius (time)
%   N is the number of sampling points
%   ord is the transformation order
%
%   C is the transformation matrix
%   r is the radius vector
%   v is the frequency vector
%   m1 prepares the input vector for transformation
%   m2 prepares the output vector for display

load('I:\My Documents\Thesis\Hankel\c.mat');
c = c(ord+1,1:N+1);

V = c(N+1)/(2*pi*R);    % Maximum frequency
r = c(1:N)'*R/c(N+1);  % Radius vector
v = c(1:N)'/(2*pi*R);  % Frequency vector

m1 = (abs(besselj(ord+1,c(1:N)))/R)';
% m1 prepares input vector for transformation
m2 = m1*R/V;
% m2 prepares output vector for display

[Jn,Jm] = meshgrid(c(1:N),c(1:N));

% C is the transformation Matrix
C = (2/c(N+1))*besselj(ord,Jn.*Jm/c(N+1))./...
    (abs(besselj(ord+1,Jn)).*abs(besselj(ord+1,Jm)));

end

```

Inverse Abel.

```

function [rf r] = Inverse_Abel(f)
% f is a 1 X ?? vector of an integrated pixel column from an
% axially symmetric distribution
% rf is the new radial function
% r is the radius vector
addpath('I:\My Documents\Thesis\Hankel');    % Path to the c.mat file.
R = length(func);
N = length(func);
ord = 0;

[C r v m1 m2] = Inverse_Hankel(R,N,ord);

f1 = fft(f);
rf = (C*(f1'./m2)).*m1;
end

```

Bibliography

1. Sarture, C. M., Chrien, T. G., Green, R. O., Eastwood, M. L., Raney, J. J., & Hernandez, M. A. (1995). Airborne Visible/Infrared imaging spectrometer (AVIRIS): Sensor improvements for 1994 and 1995. *Its Summaries of the Fifth Annual JPL Airborne Earth Science Workshop. Volume 1: AVIRIS Workshop p 145-148 (SEE N95-33730 12-42), 1 145-148.*
2. Wolfe, W. L. (1997). *Introduction to imaging spectrometers* (First ed.). Bellingham, WA: SPIE - The International Society for Optical Engineering.
3. Sagnac, E. Bouty, "The Luminiferous Ether Demonstrated by the Effect of the Relative Motion of the Ether in an Interferometer in Uniform Rotation"(in French), *Comptes Rendus (Paris) 157 (1913), p.708-710*
4. Michelson, A., & Morley, E. (1887). On the relative motion of the earth and the luminiferous ether. *The American Journal of Science, 134(203), 333-345.*
5. Eismann, M. (2008). Hyperspectral remote sensing course notes chapter 5. Unpublished manuscript.
6. Schäfer, K. *et al.* (2004). Remote passive detection of aircraft exhausts at airports. *Proceedings of SPIE, the International Society for Optical Engineering, 5270(1) 189-198.*
7. Brustet, J. M. *et al.* (1981). Infrared imagery applied to a large buoyant plume. *Journal of Applied Meteorology (1962), 20(5), 571-580.*
8. Wartewig, S. (2003). Fourier transform technique. *IR and raman spectroscopy* (pp. 40). Weinheim, Germany: Wiley-VCH.
9. Naylor, D. A. *et al.* (2006). Performance evaluation of the Herschel/SPIRE imaging Fourier transform spectrometer. *Proceedings of SPIE - the International Society for Optical Engineering, Space Telescopes and Instrumentation I: Optical, Infrared, and Millimeter, 6265 II, 626530.*
10. Eismann, M. (2008). Hyperspectral remote sensing course notes chapter 8. Unpublished manuscript.
11. Carter, M. R., Bennett, C. L., Fields, D. J., & Hernandez, J. (1993). Gaseous effluent monitoring and identification using an imaging Fourier transform spectrometer. Paper presented at the *International Symposium on Substance Identification Technologies*, Innsbruck (Austria). Retrieved from Energy Citations Database database.
12. Wallace, J., & Hobbs, P. (2006). *Atmospheric science* (2nd ed.). New York: Academic Press.

13. Schäfer, K., Heland, J., Lister, D. H. *et al.* Nonintrusive optical measurements of aircraft engine exhaust emissions and comparison with standard intrusive techniques. *Applied Optics*, 39(3), 441.
14. Schurmann, G. *et al.* (2005). Detection of emission indices of aircraft exhaust compounds by open-path optical methods at airports. *Proceedings of SPIE, the International Society for Optical Engineering*, 5979(1) 59791B; 59791B-5971-9; 59791B-9.
15. Heland, J. (1995). Remote sensing and gas analysis of aircraft exhausts using FTIR-emission-spectroscopy. *Air Pollution and Visibility Measurements; Proceedings of the Conference, Munich, Germany; UNITED STATES*, 62.
16. Agboola, F. A., Bridges, J., & Saiyed, N. (2004). *Measurements of infrared and acoustic source distributions in jet plumes*. United States: NASA Glenn Research Center.
17. Rusch, P., Harig, R., Matz, G. *et al.* SIGIS HR: A system for measurement of aircraft exhaust gas under normal operating conditions of an airport. *Proceedings of the SPIE - the International Society for Optical Engineering*, 5979(1), 597922.
18. Flores-Jardines, E. *et al.* (2005). Investigation of temperature and gas concentration distributions in hot exhausts (airplanes and burners) by scanning imaging FTIR spectrometry. *Proceedings of SPIE, the International Society for Optical Engineering*, 5979, 59791-59791.
19. Latta, T. E. AIRVAL: DOD program to evaluate air-to-air missile effectiveness (infrared signatures of high performance jet aircraft and evaluation of air to air missile effectiveness). *Corporate Author: Sandia National Labs., Albuquerque, NM*
20. Wolfhard, H. G., & Zakanycz, S. (1981). *Handbook of aircraft signatures. part I*. No. IDA-P-1569). Alexandria, VA: Institute for Defense Analyses Science and Technology Division.
21. Wolfhard, H. G. (1982). *Handbook of aircraft signatures. part II. backgrounds*. No. IDA-P-1587, IDA/HQ-81-23522). Alexandria, VA: Institute for Defense Analyses Science and Technology Division.
22. Wolfhard, H. G. (1983). *Handbook of aircraft signatures. part III. tactical aircraft*. No. IDA-P-1700-PT-3, IDA/HQ-82-25109). Alexandria, VA: Institute for Defense Analyses Science and Technology Division.
23. Sandford, B. P., Schummers, J. H., Rex, J. D., Shumsky, J., & Selby, J. (1976). *Aircraft signatures in the infrared 1.2 to 5.5 micron region. volume III. aircraft measurements of C9A, C141A, F111E, C135A, T38A and F102A*. No. AFGL-TR-0133-Vol-3). Hanscom AFB, MA: Air Force Geophysics Lab.

24. Giss, W. A. (1970). Measurement of an infrared signature of an A-7 aircraft with an infrared suppression system installed. The Eighth Symposium on Infrared Countermeasures, 13--20.
25. Wyatt, P. J., PLASS, G. N., & Stull, V. R. (1964). The infrared transmittance of water vapor (infrared transmittance of water vapor calculated over wide range of path lengths, pressures and temperatures). *Applied Optics*, 3, 229.
26. Selby, J., & McClatchey, R. M. (1972). *Atmospheric transmittance from 0.25 to 28.5/micrometers computer code LOWTRAN 2*. No. AFCRL-ERP-427). Hanscom Field, MA: Air Force Cambridge Research Labs.
27. Bradley, K., & Bowen, S. *Imaging fourier transform spectrometry of jet engine exhaust with the telops FIRST-MWE*. Unpublished manuscript.
28. Parker, C. M. (2006). *Material safety data sheet: SSA no. 2 low sulfur diesel 500 ppm sulfur max* No. 0114SPE012). Enon, OH: Speedway/Superamerica LLC.
29. Parker, C. M. (2006). *Material safety data sheet: SSA K-1 kerosene* No. 0113SPE012). Enon, OH: Speedway/Superamerica LLC.
30. United States. National Oceanic and Atmospheric Administration. (1976). *U.S. standard atmosphere: 1976*. No. NOAA-S/T 76-1562). Washington: Dept. of Commerce, National Oceanic and Atmospheric Administration.
31. Hawks, M. (2005). *Passive ranging using atmospheric oxygen absorption spectra*. Unpublished PhD, Air Force Institute of Technology, Wright-Patterson AFB, OH.
32. Farley, V., Vallieres, A. A., & Chamberland, M. M. *Hyperspectral sensor noise equivalent spectral radiance model validation with field measurements*. Unpublished manuscript.
33. Saleh, B. E. A., & Teich, M. C. (2007). *Fundamentals of photonics* (2nd Edition ed.) Wiley-Interscience.
34. Dereniak, E. L., & Boreman, G. D. (1996). *Infrared detectors and systems* (1st ed.). New York: Wiley-Interscience.
35. Legault, J. (2006). *Imaging fourier transform InfraRed spectrometer (IFTIRS). volume 1 technical proposal*. No. TEL-IFTIRS-00001). Fort Wayne, IN: Telops USA, Inc.
36. Bernath, P. F. (2005). *Spectra of atoms and molecules* (2nd ed.). Oxford, UK: Oxford University Press.
37. Turbine Technologies, LLC. (2005). *MiniLab gas turbine power system*. Chetek, WI: Turbine Technologies, LLC.

38. Smith, L. M., Keefer, D. R., & Sudharsanan, S. I. (1988). Abel inversion using transform techniques. *Journal of Quantitative Spectroscopy and Radiative Transfer*, 39(5), 367-373. Retrieved from <http://search.ebscohost.com/login.aspx?direct=true&db=inh&AN=3192517&site=ehost-live>
39. Vicharelli, P. A., & Lapatovich, W. P. (1987). Iterative method for computing the inverse abel transform. *Applied Physics Letters*, 50(10), 557-559. Retrieved from <http://search.ebscohost.com/login.aspx?direct=true&db=inh&AN=2896513&site=ehost-live>
40. Witkowski, T., White, S., Duenas, C. O., Strykowski, P., & Simon, T. (2003). Characterizing the performance of the SR-30 turbojet engine. Paper presented at the *ASEE Annual Conference Proceedings*, Nashville, TN, United States. 7743--7763.
41. Wilson, D. G., & Korakianitis, T. (1998). *The design of high-efficiency turbomachinery and gas turbines* (2nd ed.) Prentice Hall.
42. Wollenweber, G. C. (2009). In Bowen S. J. (Ed.), *Ambient and plume concentrations for turbojets*. Cincinnati, OH: General Electric.
43. National Oceanic and Atmospheric Administration. (2009). *Earth system research laboratory*. Retrieved 02/20, 2009, from <http://www.esrl.noaa.gov/gmd/ccgg/trends/>
44. Pourmovahed, A., Jeruzal, C. M., & Brinker, K. D. (2003). Development of a jet engine experiment for the energy systems laboratory. Paper presented at the *Proceedings of the ASME Advanced Energy Systems Division - 2003*, Washington, DC., United States. 229--247.
45. Guizar-Sicairos, M. (2004). Computation of quasi-discrete hankel transforms of integer order for propagating optical wave fields. *Journal of the Optical Society of America.A, Optics, Image Science, and Vision*, 21(1), 53-58.

REPORT DOCUMENTATION PAGE

Form Approved
OMB No. 074-0188

The public reporting burden for this collection of information is estimated to average 1 hour per response, including the time for reviewing instructions, searching existing data sources, gathering and maintaining the data needed, and completing and reviewing the collection of information. Send comments regarding this burden estimate or any other aspect of the collection of information, including suggestions for reducing this burden to Department of Defense, Washington Headquarters Services, Directorate for Information Operations and Reports (0704-0188), 1215 Jefferson Davis Highway, Suite 1204, Arlington, VA 22202-4302. Respondents should be aware that notwithstanding any other provision of law, no person shall be subject to a penalty for failing to comply with a collection of information if it does not display a currently valid OMB control number.

PLEASE DO NOT RETURN YOUR FORM TO THE ABOVE ADDRESS.

1. REPORT DATE (DD-MM-YYYY) 26-03-2009		2. REPORT TYPE Master's Thesis		3. DATES COVERED (From - To) September 2008 - March 2009		
4. TITLE AND SUBTITLE Hyperspectral imaging of a turbine engine exhaust plume to determine radiance, temperature, and concentration spatial distributions				5a. CONTRACT NUMBER Proposal ID 2007-162, JON# 09-317		
				5b. GRANT NUMBER		
				5c. PROGRAM ELEMENT NUMBER		
6. AUTHOR(S) Bowen, Spencer J., Captain, USAF				5d. PROJECT NUMBER		
				5e. TASK NUMBER		
				5f. WORK UNIT NUMBER		
7. PERFORMING ORGANIZATION NAMES(S) AND ADDRESS(S) Air Force Institute of Technology Graduate School of Engineering and Management (AFIT/EN) 2950 Hobson Way WPAFB OH 45433-7765				8. PERFORMING ORGANIZATION REPORT NUMBER AFIT/GAP/ENP/09-M02		
9. SPONSORING/MONITORING AGENCY NAME(S) AND ADDRESS(ES) AFRL/RYS Attn: Mr. Jeffrey W. Burks 2591 K St., Bldg 254 WPAFB OH 45433-7301 DSN: 785-9205				10. SPONSOR/MONITOR'S ACRONYM(S) AFRL/RYS		
				11. SPONSOR/MONITOR'S REPORT NUMBER(S)		
12. DISTRIBUTION/AVAILABILITY STATEMENT APPROVED FOR PUBLIC RELEASE; DISTRIBUTION UNLIMITED						
13. SUPPLEMENTARY NOTES						
14. ABSTRACT The usefulness of imaging Fourier transform spectroscopy (IFTS) when looking at a rapidly varying turbine engine exhaust scene was explored by characterizing the scene change artifacts (SCAs) present in the plume and the effect they have on the calibrated spectra using the Telops, Inc.-manufactured Field-portable Imaging Radiometric Spectrometer Technology, Midwave Extended (FIRST-MWE). It was determined that IFTS technology can be applied to the problem of a rapidly varying turbine engine exhaust plume due to the zero mean, stochastic nature of the SCAs, through the use of temporal averaging. The FIRST-MWE produced radiometrically calibrated hyperspectral datacubes, with calibration uncertainty of 35% in the 1800 - 2500 cm ⁻¹ (4 - 5.5 μm) spectral region for pixels with signal-to-noise ratio (SNR) greater than 1.5; the large uncertainty was due to the presence of SCAs. Spatial distributions of temperature and chemical species concentration pathlengths for CO ₂ , CO, and H ₂ O were extracted from the radiometrically calibrated hyperspectral datacubes using a simple radiative transfer model for diesel and kerosene fuels, each with fuel flow rates of 300 cm ³ /min and 225 cm ³ /min. The temperatures were found to be, on average, within 212 K of <i>in situ</i> measurements, the difference attributed to the simplicity of the model. Although no <i>in situ</i> concentration measurements were made, the concentrations of CO ₂ and CO were found to be within expected limits set by the ambient atmospheric parameters and the calculated products of the turbine engine, on the order of 10 ¹⁵ and 10 ¹⁷ molecules/cm ³ , respectively.						
15. SUBJECT TERMS Hyperspectral imaging; imaging Fourier transform spectroscopy; turbine engine exhaust plumes; scene change artifacts; temperature distributions; concentration pathlength distributions						
16. SECURITY CLASSIFICATION OF:			17. LIMITATION OF ABSTRACT	18. NUMBER OF PAGES	19a. NAME OF RESPONSIBLE PERSON	
REPORT	ABSTRACT	c. THIS PAGE	UU	154	Michael A Marciniak, PhD, AFIT/ENP	
U	U	U			19b. TELEPHONE NUMBER (Include area code) 937-255-3636 x 4529, michael.marciniak@afit.edu	